Study on shoreline position and intertidal foreshore slope detection using remote sensing imagery

著者（英）	KUMAR DIPANKAR
year	2019
その他のタイトル	リモートセンシングデータからの汀線位置と前浜勾配の検出に関する研究
学位授与大学	筑波大学 (University of Tsukuba)
学位授与年度	2018
報告番号	12102甲第9025号
URL	http://doi.org/10.15068/00156316

Study on shoreline position and intertidal foreshore slope detection using remote sensing imagery

March 2019

DIPANKAR KUMAR

Study on shoreline position and intertidal foreshore slope detection using remote sensing imagery

Graduate School of Systems and Information Engineering

University of Tsukuba

March 2019

DIPANKAR KUMAR

ACKLNOWLEDGEMENTS

It is beyond doubt that it would not have been possible to write this doctoral thesis without the support, advice, and encouragement from the supervisor, teachers, lab mates, friends, and support from my parents and siblings. Accordingly, I would like to use this opportunity to express my gratitude to a number of people, both academically and personally, who over the years have contributed in a various way to completion of this work.

At first, I would like to express my heartiest gratitude to my academic supervisor, Professor Dr. Satoshi TAKEWAKA, for his supervision, dedicated advice, motivation and guidance from the very early stage of the doctoral research as well as giving me excellent opportunity for doctoral study in the Department of Engineering Mechanics and Energy of the University of Tsukuba, Japan. I will put all from him in my mind, and it will help me a lot for the whole of my life. Indeed, I have no word to appreciate for his all efforts, because his efforts for me are priceless.

I would also like to give heartiest acknowledgments to the member of my dissertation committee, Professor Dr. Harumichi KYOTOH, Professor Dr. Yuko HATANO, Associate Professor Dr. Naoki SHIRAKAWA, and Associate Professor Dr. Tadashi EBIHARA, for their valuable assistance and suggestions that they have given during the refereeing phase of this dissertation.

I am very much grateful to Professor Dr. Gour Chandra Paul as a supervisor during my master’s study in the Department of Mathematics at University Rajshahi, Bangladesh. I would like to express special gratitude to Professor Dr. Ashabul Hoque for his encouragements. Without his encouragements and guidance, I would not have been possible to realize a doctoral degree in Coastal Engineering. I am also very much grateful to my teacher Professor Dr. Md. Abdus Sattar, for his motivation and inspiration during the early

stage of the Ph.D. study. Without his unexplainable effort, I could not be able to start my Ph.D. study here in Japan.

Special and sincere thanks to my present and former colleagues of Hydraulic and Hydrodynamic laboratory for their kindness and assistance in my Japan life. I am grateful for the help and friendship behavior from my Japanese and other countries colleagues and friends.

I am very much thankful to the Government of Japan, for providing me the Monbukagakusho scholarship through the Ministry of Education, Culture, Sports, Science, and Technology (MEXT) that made my study possible in the Department of Engineering Mechanics and Energy of the University of Tsukuba. I am also thankful to the Government of Bangladesh, for providing me the higher study leave through the Ministry of Education and the authority of Bangabandhu Sheikh Mujibur Rahman Science and Technology University (BSMRSTU). These both opportunities helped to make my dreams come true.

Finally, my infinite gratitude goes to my parents for their unconditional love along with their continuous support, encouragement, and patience throughout my life. This doctoral thesis is dedicated to the memory of my father who passed away on 22nd April 2015.

ABSTRACT

Four land-based X-band radars were installed along the 16 km long straight micro-tidal sandy Kashima Coast, Japan to monitor the shoreline variations within the intertidal zone. The radars monitor the shoreline positions continuously in time but do not cover the whole spatial domain of the coast. On the other hand, Synthetic Aperture Radar (SAR) covers the whole spatial domain, but data is available only a few times in a year. For full spatial coverage of the coast, the SAR satellite observation shoreline positions are introduced, where the radar's data are not available.

The studies of shoreline are vital to the early stages of the decision-making process for planned coastal developments to mitigate the potential loss of buildings, infrastructure, and beaches. These studies have also a considerable importance due to its significance in coastal management and climate change vulnerability analysis. Indeed, automatic and accurate detection of shoreline position and intertidal foreshore slope are challenging and significantly important in coastal management for coastal protection. Based on these significances, the primary target is to employ the modified Temporal Waterline Method (mTWM) on a radar captured time averaged images captured throughout the course of two-week tidal cycle variation over an area spanning 5.6 km within the coast to detect shoreline positions and intertidal foreshore slopes during 2005 – 2008. The utilized method is based on the correlation map between the pixel intensity variation of the time-averaged X-band radar images, and the binary representation tide signal at each water levels, which are used to determine the shoreline positions at the land-water interface and intertidal foreshore slopes. In order to ensure the binary signal represented each of the water levels in the intertidal shore profile, determining the water level direction-wise bottom elevation is considered as the modification. Random gaps were detected in the captured images owing to the unclear or over saturation of waterline signal. In order to assess the feasibility of the method, the detected shoreline positions and intertidal foreshore slopes are compared with previously collected survey data at Hasaki Oceanographical Research Station (HORS). A horizontal shift is observed in the detected shoreline positions compared to the survey data; however, the intertidal foreshore slopes estimation is reasonably well. This horizontal shift can be attributed to wave breaking and high wave conditions. Wave set-up and run-up are the effects of wave breaking and high wave conditions, respectively. The correction of wave set-up and run-up is considered to allow the upward shift of water level position, as well as shoreline position shifted to landward direction. It was found that the shoreline positions extracted from radar images with corrected wave run-up reasonably agree with the survey data. The mean absolute bias (MAB) between survey data and the shoreline positions detected using mTWM with corrected wave run-up is approximately 5.9 m, which is less than the theoretical spatial resolution of the radar measurements. Time-averaged radar images were selected for shoreline detections to discuss shoreline variations at the sandy coast, Kashima, Japan during various periods, and to demonstrate the practicability of the utilized method. Therefore, the temporal and spatial variations of a shoreline can be automatically and continuously monitored over the long term to help the authorities to understand coastal changes, facilitating coastal protection and sustainable development in coastal zones.

In order to determine the wave run-up corrected shoreline positions, the mTWM with wave run-up correction is applied further to remains other radars captured time-averaged images between 2009 and 2012. As a result, the shoreline positions were obtained successfully. As earlier mentioned, the radars do not cover the whole spatial extent. Therefore, to overcome the difficulties of land-based X-band radars and SAR satellite observations, a data fusion method is proposed that integrates the radars and SAR satellite observation shoreline positions by using Data INterpolating Empirical Orthogonal Functions (DINEOF) method. The validity of the proposed method results is checked by aerial laser survey data and found reasonable agreement. The MAB between aerial lased survey data and the data fusion extracted shoreline positions is approximately 11.7 m, which is very close to the theoretical spatial resolution of Radar and SAR satellite observation measurements (10 m). The obtained outcome that allows the data fusion shoreline dataset establishes a technique namely the DINEOF can generally be a comprehensive strategy for estimating gap values in spatiotemporal datasets.

Keywords: *Kashima Coast, X-band radar; Synthetic Aperture Radar; Modified Temporal Waterline Method; Tidal variation; Shoreline position; Intertidal foreshore slope; Wave run-up correction; Data fusion;*

TABLE OF CONTENTS

LIST OF FIGURES

LIST OF TABLES

LIST OF ABBREVIATIONS

DCT	Discrete Cosine Transform
DEM	Digital Elevation Models
DINEOF	Data INterpolating Empirical Orthogonal Functions
ETM+	Enhanced Thematic Mapper Plus
JAXA	Japan Aerospace Exploration Agency
FS	Foreshore Slope
HORS	Hasaki Oceanographical Research Station
LiDAR	Light Detection and Ranging
mTWM	modified Temporal Waterline Method
Max.	Maximum
Min.	Minimum
MWL	Mean Water Level
MAB	Mean Absolute Bias
NOWPHAS	Nationwide Ocean Wave Information Network for Ports and Harbors
PLS	Penalized Least Squares regression
SAR	Synthetic Aperture Radars
Std.	Standard Deviation
SP	Shoreline Position
TM	Thematic Mapper
TWM	Temporal Waterline Method

CHAPTER ONE : INTRODUCTION

1.1 Background

Coastal engineering is a rapidly growing branch of civil engineering. It is responsible for the study of the processes of shore protection, coastal zone development, waves, currents and longshore sediment transport, the morphological and environmental impact of the coastal, harbor and offshore structures, and prevention or mitigation of coastal disasters. The objective of coastal engineering involves management and monitoring of shoreline erosion and accumulation, improvement of navigation channels and harbors, utilization of infrastructures, understanding seismically triggered wave (tsunamis), and management of pollution in nearby marine environments.

Over the last few decades, remote sensing data such as aerial photographs, Light Detection and Ranging (LiDAR) surveys, video camera analysis, optical satellite imagery, and land-based X-band radars have become more popular among the coastal scientists, engineers, and planners. Depending on the specific platform, these data are used as an important tool for monitoring the intertidal morphology, shoreline mapping, coastal erosion and accretion, land subsidence and rip current measurements. These kinds of monitoring tools are also essential for understanding the morphological behavior of the nearshore environment and coastal environmental protection.

The shoreline is an indicator of coastal erosion and accretion. It is defined as the borderline that separates coastal land and water (Pajak and Leatherman, 2002). It can be changed due to erosion and accretion, and as the nearby land use patterns change, erosion or accretion takes place resulting in changes of the shoreline. There is more than 347,984 km of shoreline in the world. Over 60 percent of the world’s population is geographically located within 100 km of the coastal areas (Vitousek et al., 1997). It’s shape and position changes dynamically with time and influenced by alongshore sediment transport, wind-generated waves, and tides. Since shoreline has a dynamic feature, its detection and monitoring are a challenging and complicated task. In this regard, coastal scientists and engineers are continuously looking for better tools to determine the accurate position of shorelines and analyze the variations in shoreline position from the above mentioned remotely sensed imagery. There have been several ways (viz. manual, semi-automatic and automatic) to detect shoreline positions from remotely sensed data. However, the manual and semi-automatic shoreline digitization method is a very tedious, time-consuming, and labor-intensive operation than the automatic digitization method. In this regard, numerous automated detection approaches have been established and employed to perceive expected objects from different types of remotely sensed data. Thus, in the present study, we sought to apply an automatic method to accurately detect the shoreline positions and intertidal foreshore slopes using X-band radar images. Finally, a data fusion method is introduced for integrating X-band radars and SAR satellite observation shoreline position data.

1.2 Review of literature

Remote sensing is the acquisition of essential information that helps in monitoring various applications such as coastal process, image fusion, change detection and land cover classification. It is a key technique that obtain information related to the earth’s resources and environment such as hydrology, ecology, meteorology, oceanography, glaciology, and geology. It’s also allows for observation and measurement of coastline or shoreline without direct contact. These data can be used to evaluate the coastal processes like littoral drift, erosion/accretion and shoreline changes and to study water geomorphology landforms, sediment concentration, water quality etc. In past, several studied (Crowell et al., 1991; Camfield and Morang, 1996; Kraus and Rosati,1997; Takewaka, 2005; Hanslow, 2007; Ryu et al., 2008; Chen and Chang, 2009; Chang et al., 2015; Gabriela Garcia-Rubio et al., 2015; Bell et al., 2016; Bird et al., 2017) have been conducted on shoreline position detection and investigate their variability from several data sources such as: aerial photographs, beach profile surveys, Light Detection and Ranging (LiDAR) surveys, video camera analysis, satellite imagery, and X-band radar images.

Aerial images typically have broad spatial coverage; however, their temporal coverage is limited by acquisition time. Light Detection and Ranging (LiDAR) systems can cover large areas over short time periods and provide both accurate and more effective high-resolution Digital Elevation Models (DEM). However, the data source is usually limited due to the high processing cost.

Video imaging systems are becoming more popular for continuously monitoring the coastal morphological behaviors worldwide. It can also be employed to track the sea surface features with high temporal resolution, as usual contributing several images per second, in addition, to trace stretches of intertidal sandy beaches at some sites around the world. Thus, several video monitoring techniques (Aarninkhof et al., 2003, 2005; Holman et al., 1993; Holland and Holman, 1997; Plant and Holman, 1997; Uunk et al., 2010; De Santiago et al., 2013; Sobral et al., 2013; Valentini et al., 2017) have been used for understanding the long-term behavior of the shoreline positions and nearshore beach processes.

Video cameras can generate color images, which allow the identification of wave breaking, suspension of foams, and sediment concentrations etc., and to seek out their temporal and spatial variations. It is often mounted on towers standing along the shoreline to provide slanted views, and the rectified montages of video images from different cameras allow to measure wave and current fields, sediment transport and morphological characteristics (Austin and Masselink, 2006). However, the application of video monitoring is limited to daylight hours and fair-weather conditions. The invention of thermal infrared cameras allows using the data collected by video monitoring both during the day and at night to procure intertidal DEM (Gaudin et al., 2009). In addition, thermal infrared cameras operate in low light conditions to observe hydrodynamics in the nearshore zone. Such monitoring systems operate well in low visibility, have excellent temporal and spatial coverage, and can provide a data quality identical to that produced by a camera at slightly lower resolution. But it is remarkably higher range regardless of light conditions (Dankert and Horstmann, 2007).

X-band radar is an integral part of nearshore the remote sensing infrastructure system, which can be used to overcome some of the limitations of video imaging (Holman and Haller, 2013). They have been employed to trace the significant movement of wave crests over areas spanning several kilometers to detect coastal features. The most attractive feature of X-band radar systems applications is their ability to continuously and remotely collect data that allow the proper understanding of the nearshore coastal processes along the coastal areas under different weather conditions. Since last two decades, land-based remote sensing monitoring system like as X-band radar has been gradually popular in coastal studies, because it can provide real-time and uninterrupted observation, even in bad weather conditions (Bell, 1999; Takewaka, 2005; Galal and Takewaka, 2008, An and Takewaka, 2016, Bell et al., 2016; Bird et al., 2017).

Bell (1999) succeeded in determining near-shore bathymetry after analyzing X-band radar images. He applied a linear depth inversion technique, considering peak period from Fast Fourier Transforms (FFT), and wave celerity from cross correlations between sequences of images. Elsayed and Takewaka (2008) identified seasonal variations of longshore shoreline positions and longshore migrations with an X-band radar at Kashima Coast, Ibaraki, Japan. They compared seasonal variations of longshore position with estimated longshore wave energy fluxes and observed longshore movements of shoreline mega-cusps within the intertidal range by inspecting sequences of time-averaged radar images. They also estimated the longshore migration speeds of mega cusps and compared them with the measured longshore current speeds and components of wave energy. They found that the maximum migration speed occurred between an incident wave angle of 40^o and 45^o for the northern migrations. Recently, An and Takewaka (2016) identified the spatiotemporal variations of the shoreline positions around the three artificial Headlands (HLs) by Empirical Orthogonal Function (EOF) analysis and to explain them with respect to incident waves and surf zone extensions. They conclude that the surf zone extensions being a major factor in the distribution of shoreline variability within the Kasima Coast, Japan. Among of the above cited references, authors (Takewaka, 2005; Elsayed and Takewaka, 2008; An and Takewaka, 2016) were extracted the shoreline positions manually with the help of tidal records and the instantaneous waterlines from time averaged X-band radar images.

Recently, many intensive attempts have been conducted on the detection of waterline positions using the waterline method from various remote sensing data. The waterline position is one type of shoreline indicator, which is used to describe the instantaneous position of land and water interface for every measurement. Due to rhythmic rise and down of the tide level, the waterline position shifted horizontally from its mean water level (MWL) position to landwards or seawards direction. Generally, shoreline position is defined at the MWL. After induced tide correction, the waterline position is known as shoreline position.

In the past, several potential scholars (Koopmans and Wang., 1994; Mason et al., 1995; Heygster et al., 2010; Ryu et al., 2002; Zhao et al., 2008; Xu et al., 2016; Takewaka,

2005) have applied the waterline approach to data collected by Synthetic Aperture Radars (SAR) images, satellite images, and X-band radar images.

For instance, Koopmans and Wang (1994) applied the waterline approach to SAR data, identified the waterlines of the intertidal areas of Wadden Sea, and used a tidal model to assign those contours to water elevations. Mason et al. (1995) adopted the same approach using SAR images of the extensive intertidal areas of Morecambe Bay in the United Kingdom (UK). Heygster et al. (2010) also used SAR images and applied the waterline approach to generate the tidal flats topography along the German coast of the Wadden Sea between 1996 and 1999. Ryu et al. (2002) extracted the waterline of a tidal flat in Gomso Bay, Korea from Landsat Thematic Mapper (TM) data, whereas Zhao et al. (2008) applied an identical approach to multi-temporal satellite images of the Yangtze Delta, China. Recently, Xu et al. (2016) have conducted a study to estimate the temporal and seasonal topographic changes associated with two major tidal flats in Gomso and Hampyeong Bay in the southern part of the West Sea of South Korea based on the waterline approach using 18 scenes of Landsat TM and Enhanced Thematic Mapper Plus (ETM+) data considering the corresponding tidal gauge observation data, covering the period of 2003 – 2004.

Takewaka (2005) have employed X-band marine radar to detect the shoreline positions and intertidal foreshore slopes by imaging the waterlines in the spatial domain and describing beach contour lines using time-averaged images and tidal records. The findings revealed acceptable agreement with the survey data, concluding that the radar estimation can be considered as a mighty tool to track the morphology of sandy coasts. Furthermore, the shoreline positions and intertidal foreshore slopes were manually digitized using the tidal records and waterlines extracted from time-averaged X-band radar images.

The waterline extraction approach, which is based on visual interpretation, is considered as an effective, and straightforward procedure that can be extensively applied to remote sensing data. This method relies on the human eye capability to precisely detect the boundaries between coastal land and water from aerial photographs, SAR images, optical satellite images, and X-band radar images. However, the manual digitization method involves very tedious, time-consuming, and labor-intensive practices to measure the boundaries between coastal land and water. Hence, developing an automated process to measure the shoreline positions was urgently needed. In this regard, numerous automatic digitization approaches (Dellepiane et al., 2004; Bell et al., 2016; Fuse and Ohkura, 2018; Liu and Jezek, 2004; Paravolidakis et al., 2018; Pardo-Pascual et al., 2012; Vandebroek et al., 2017) have been developed and implemented to detect expected objects from different types of remotely sensed data. In the present study, we focus on an automatic digitization approach to detect shoreline positions and intertidal foreshore slopes from time-averaged X-band radar images.

Based on the demand, Bell et al. (2016) developed the Temporal Waterline Method (TWM) as a robust method to automatically detect intertidal shore profiles using the pixel intensity variation in time-averaged X-band radar images and the binary signal of tidal records. For validation, Bell et al. (2016) adopted the method to develop a morphological map of the target intertidal shore profile using X-band dataset received from Hilbre Island at the mouth of Dee Estuary, UK. The resulting gathered elevation maps were presented the intertidal region with a radial range of 4 km of that area. The accuracy of the extracted results obtained by the TWM was verified in comparison to airborne LIDAR data surveyed throughout the same area and during the radar survey period. The vertical elevation bias between the compared results was approximately ±0.5 m, indicating that a relatively stable macrotidal environment was utilized as the test case. Furthermore, Bird et al., 2017 employed the TWM to monitor the inter- and intra-annual intertidal morphological changes and described the seasonal variations in the morphology of Hilbre Island at the mouth of Dee Estuary, UK. The heterogeneous macrotidal study area examined by Bird et al. (2017) for sandy, sandbank, intertidal sand flats, and saltmarsh beaches, along with several rocky outcroppings.

1.3 Motivation and significance of the study

The studies of shoreline are vital to the early stages of the decision-making process for planned coastal developments to mitigate the potential loss of buildings, infrastructure, and beaches. These studies have also a great importance due to its significance in resource extraction, coastal management and climate change vulnerability analysis. Indeed, accurate intertidal shore profile detection plays an effective role in coastal management for coastal protection. Manual digitization method can accurately detect the intertidal shore profile as well as shoreline positions and intertidal foreshore slopes from X-band radar images; however, it is a most labor-intensive and time-consuming operation. These obstacles have effectively prevented by introducing an automated method. Therefore, an automatic method namely modified Temporal Waterline Method (mTWM) is introduced and applied to accurately detect the intertidal shore profile as well as detect the shoreline positions and intertidal foreshore slopes using X-band radar images to a sandy, highly varied, and micro-tidal beach site at Kashima Coast, Japan. However, the radars do not cover the whole spatial domain of this coast. For whole spatial coverage, SAR observation is introduced.

The most significance of this study is to digitize the shoreline positions and intertidal foreshore slopes from radar images accurately and automatically in quick time, which may drastically minimize the digitization time and updating the database in shorter time. By introducing data fusion technique between radars and SAR observation shoreline positions, the spatial coverage is enhanced, which remove the limitations of both observations.

1.4 Objectives of the study

This study is to focus on the application of mTWM to a highly movable micro-tidal sandy beach exposed to energetic waves of the south Pacafic Ocean with a comparison of the shoreline position and intertidal foreshore slope results with survey results along the pier in the four years from 2005 – 2008. Precisely, the study is to validate the accuracy of the mTWM extracted shoreline positions and intertidal foreshore slopes compared to survey data. In accordance with the above discussion, the objectives of the study involve the following:

- to implement an automated mTWM to detect the time series shoreline positions and intertidal foreshore slopes extracted from time stack X-band radar images considering the tidal variation in the above mentioned entirely sandy and micro-tidal study site,
- to validate the derived temporal updates of shoreline positions and intertidal foreshore slopes at the research pier in comparison to the previously collected beach profile survey data,
- to compare the temporal updates of the extracted shoreline positions with corrected wave set-up and run-up at the research pier with beach profile survey data, and
- to propose a data fusion technique that integrates land-based X-band radars and SAR satellite observation shoreline positions, which are integrated by using the Data INterpolating Empirical Orthogonal Functions (DINEOF) method. The validity of the proposed method results is checked by aerial laser survey data.

1.5 Thesis outline

The rest of the thesis is organized as follows. Chapter two describes the study area environments and available data description.

Chapter three describes the automatic application to detect the shoreline positions and intertidal foreshore slopes from X-band radar images and its validation with previously collected beach profile survey data.

Chapter four introduces a data fusion technique that integrates the X-band radars and Synthetic Aperture Radar (SAR) observation shoreline positions. The estimated fused data is validated with aerial laser survey data.

Finally, the conclusions, limitations, and recommendations for further study are presented in chapter five.

CHAPTER TWO : STUDY AREA AND DATA DESCRIPTION

This chapter describes the study area environment and the different data sets that are used in this research. The complete documentation of X-band radars and SAR satellite observation data and its processing are provided in this chapter. The previously collected field survey beach profile and aerial laser survey data also illustrated here. Besides above-mentioned data, the waves and tide data are also described in this chapter.

2.1 Study area

Kashima coast, which is located in the Ibaraki Prefecture of Japan facing the South Pacific Ocean, is almost straight with a sandy beach that spread over an area spanning approximately 16 km. It is bounded on the south end by Choshi Fishery Port and the north end by Kashima Port. The study area is marked with the yellow rectangle box shown in **Figure 2.1**. The 400 m long field observation research pier which perpendicular to the shore is located in the center of Hasaki Oceanographical Research Station (HORS) with the research building located on the backshore approximately 110 m backward from the mean shoreline position. The horizontal axis indicates the longshore extent and vertical axis corresponds the cross-shore extent along the pier is defined relative to the HORS reference point and a positive seaward direction is used (see **Figure 2.1**). The beach experiences high waves during the winter season and is relatively calm during summer. The median sediment diameter of 0.18 mm that occasionally increases to 1.00 mm around troughs after severe storms (Katoh and Yanaghima, 1995). Based on the previous study (Kuriyama, 2002; Kuriyama et al., 2008) at the single bar Hasaki coast, the mean beach slope was 1/50, ranging from -60 to 200 m seaward, and 1/200 in the deeper area.

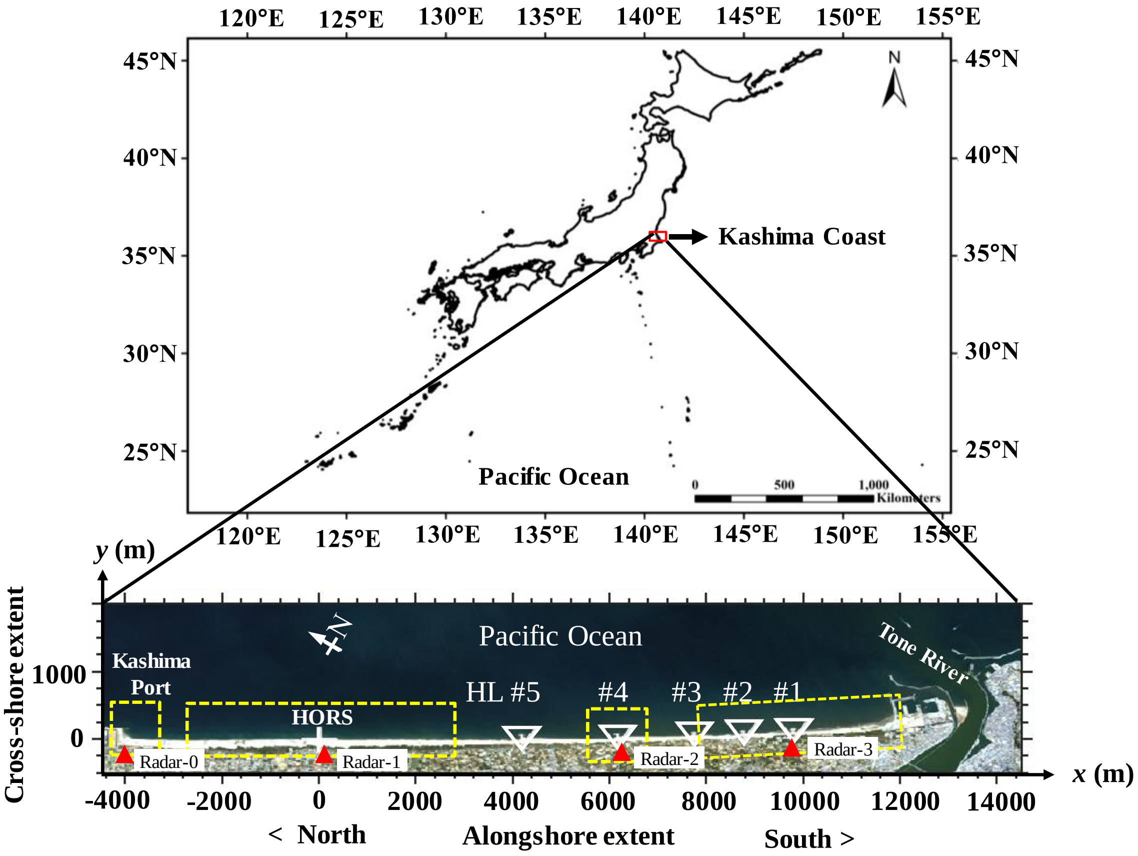

Figure 2.1. Location map of study area: Kashima Coast, Japan. The red triangle indicates the radar location. The origin of the coordinate system is located at the base of HORS. Yellow rectangular box indicates the area covered by radar observation and white triangles indicate the positions of artificial headlands.

2.2 Radar observations

2.2.1 X-band radar system and radar echo images

Four conventional X-band marine radars were installed along the coast to monitor the morphological variations within the intertidal zone and the wave motions (Takewaka, 2005; Hasan and Takewaka, 2007). As seen in **Figure 2.1**, one radar was installed at the research pier of HORS of the Port and Airport Research Institute (PARI) of Japan. Two radars were installed at the southern portion of the beach protected by the HLs. Another one was installed at the northern end near Kashima Port. Each radar can trace the distributions of waterline in the intertidal zone and wave motions within the effective spatial coverage range.

Figure 2.2 show the HORS and the radar antenna on the roof of the research building. The radar antenna is mounted on the roof of the research building 17 m above the mean sea level. The 2.8 m long antenna rotates with a period of approximately 2.6 seconds, and radar backscatter from the sea surface, so-called sea clutter, are captured with a specially designed A/D-board with a sampling rate of 20 MHz installed on Windows PC. The backscatter echo signals are converted to gray images. The data collection process of X-band radar data is described in **Figure 2.3**. The sampled echo signals from the sea surface are converted to a rectangular image of 1,024 pixels in the horizontal (longshore extent) and 512 pixels in the vertical (cross-shore extent), as shown in **Figure 2.4**, which shows examples of radar echo images. Panel (a) of **Figure 2.4** is sea state during calm wave condition, (b) is during high wave condition. The slanted white lines extending in the long-shore direction are oblique wave crests and vertical strip in the middle of the figure is research pier. The radar is located at the midpoint of the bottom edge of the echo image indicated by a black dot. In echo images, several features, such as wave crests, wave ray, and waterline positions can be identified. However, it is unable to trace the wave crests with lower wave heights which can be observed in **Figure 2.4**(a). The details of the radar system were described by Takewaka (2005).

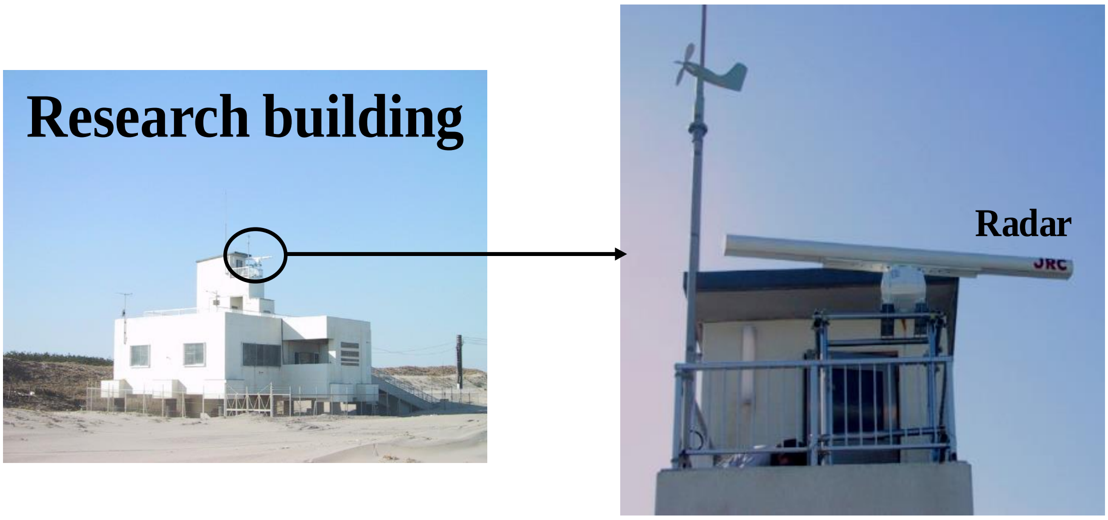

Figure 2.2. Camera view of Hasaki Oceanographical Research Station (left photo) and radar antenna (length 2.8 m) on the roof of the research building (right photo).

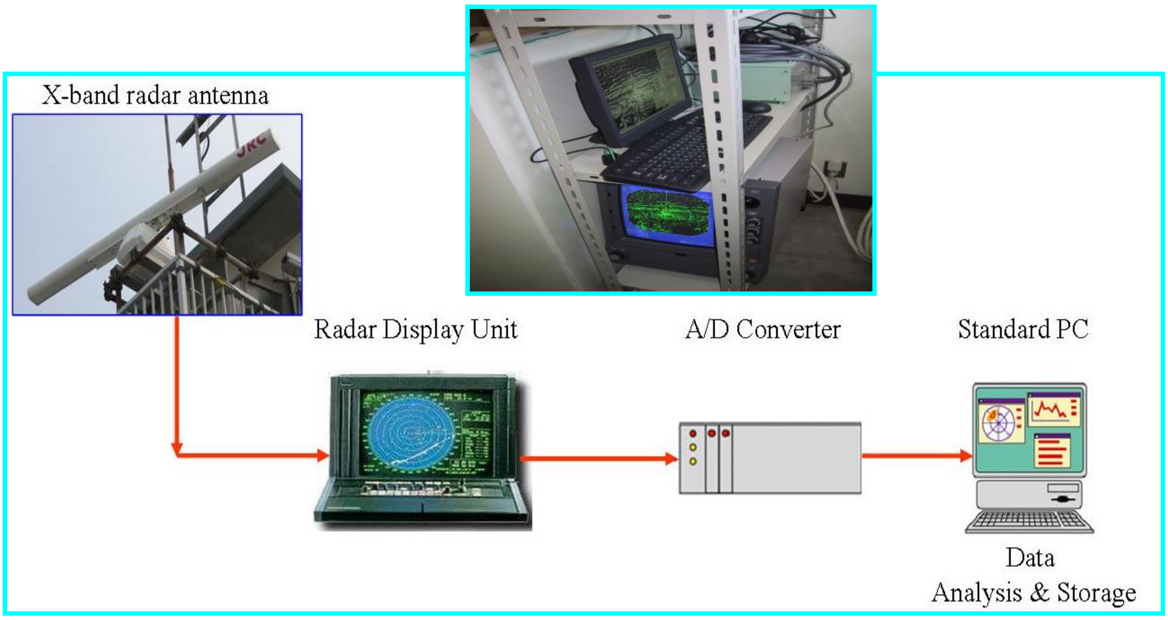

Figure 2.3. X-band radar data collection procedure.

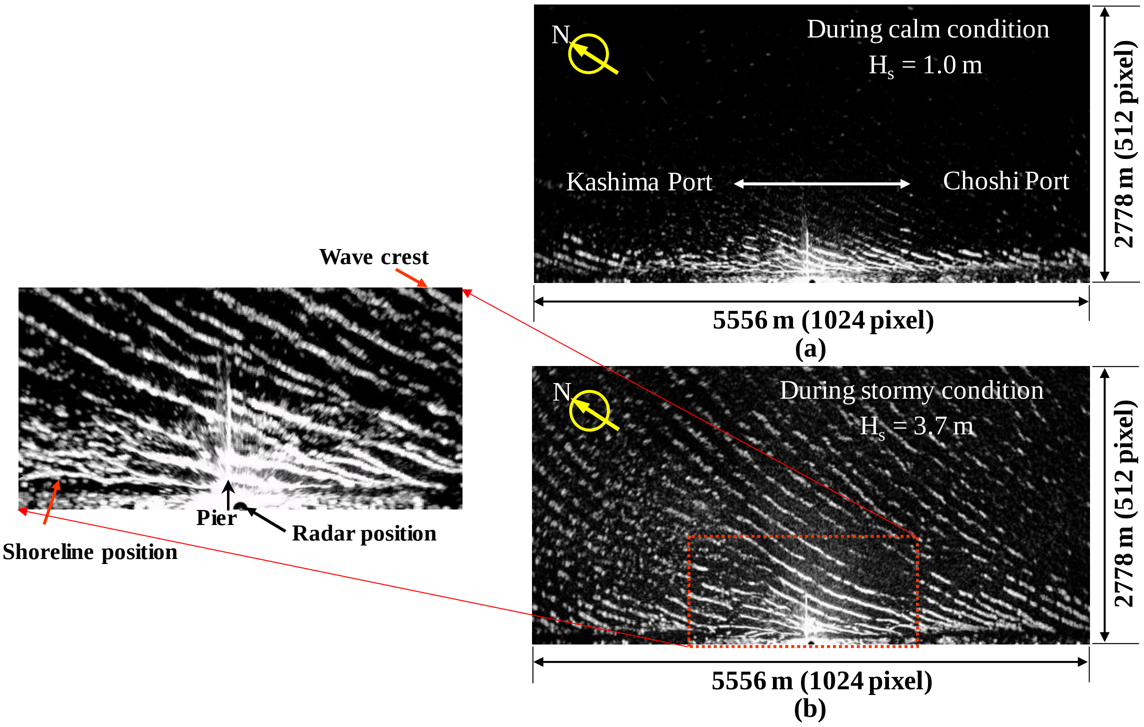

Figure 2.4. Examples of radar echo images: (**a**) calm condition (27 July 2005 at 8.00; significant wave height H_s = 1.02 m, and significant wave period T = 12.0 s) and (**b**) stormy condition (26 July 2005 at 22.00; H_s = 3.69 m and T = 12.1 s).

2.2.2 Time averaged image

Individual echo images sampled every 2 seconds were averaged yielding a "time-averaged image" or so-called "time-exposure" (Takewaka, 2005). Ensembles of 512 individual echo images over 17 minutes $(512\ \times 2\,\mathrm{s} = 1024\,\mathrm{s})$ were processed to time averaged radar images for every hour. This image-capturing interval of 2 s is shorter than the time required for the rotation of the antenna (approximately 2.6 s); therefore, the data acquisition is oversampled, and an un-updated portion exists always in the original radar image. This un-updated portion does not affect the following analyses in which time-averaged images are used. The echo signals are converted into a rectangular image size of 1024 pixels horizontal (longshore extent) and 512 pixels vertical (cross-shore extent). The pixel size of the rectangular image is approximately 5.42 m, whereas the theoretical spatial resolution of the radar system is approximately 7.5 m. Thus, the image covers an area spanning approximately 5556 m (1024 pixels) in the alongshore direction and 2778 m (512 pixels) in the cross-shore direction, as shown in **Figure 2.5**.

Figure 2.5(b) shows an example of time-averaged X-band radar image and coordinate system. The *x*-axis corresponds to the longshore extent, and the *y*-axis is taken in the cross-shore direction, positive toward the offshore. The pixel intensities of the time-averaged gray images are belonging 0 (no backscatter) to 255 (saturation). Owing to reflections, individual waves disappear in the time averaged radar images, and off and onshore edges of extending in the longshore direction becomes visible, as shown in see **Figure 2.5**. The time averaged images enable identification of the intertidal bathymetry, breaker zone, rip current, mega-cusp migration, wave run-up, bar crest locations and other features (An and Takewaka, 2015; Elsayed and Takewaka, 2008; Hasan and Takewaka, 2007; Takewaka, 2005). Hourly processed time-averaged images have been collected since 2005; however, some data gaps were reported due to mechanical trouble.

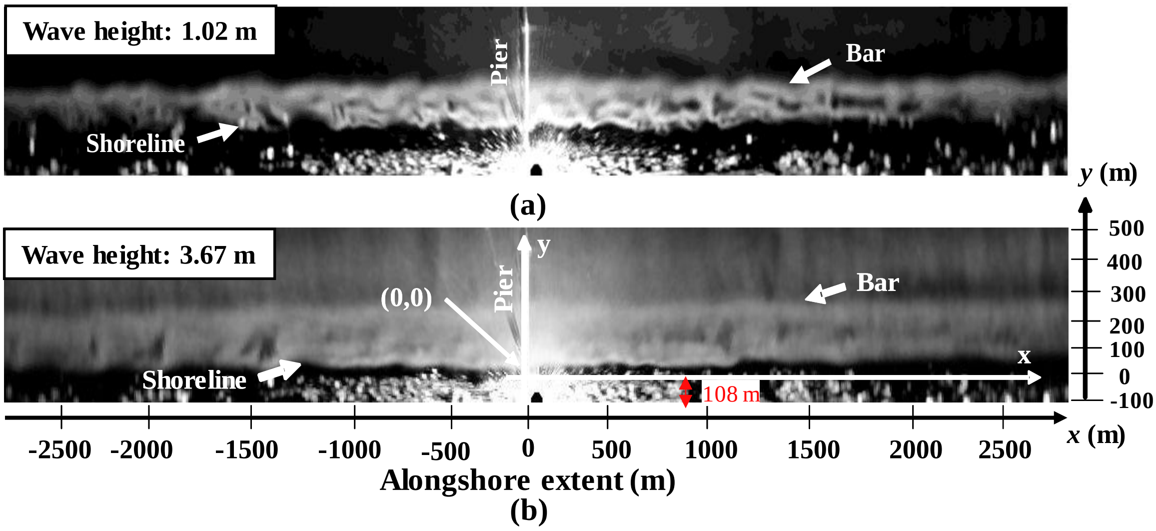

Figure 2.5. Time-averaged X-band radar image: (**a**) calm condition (27 July 2005 at 8.00; significant wave height H_s = 1.02 m and significant wave period T = 12.0 s) and (**b**) stormy condition (26 July 2005 at 22.00; H_s = 3.69 m and T = 12.1 s). The coordinate system is described in (b).

2.3 Synthetic Aperture Radar (SAR) observation shoreline position

Synthetic Aperture Radar (SAR) is an active remote sensing system which has applications in agriculture, ecology, geology, oceanography, hydrology, military, etc. (Eves, 1998). Its installed in an artificial satellite or an aircraft that can observe the surface of the earth without being affected by clouds. Using the SAR data, research is being conducted in the coastal engineering field like as spectrum estimation of surface waves, detection of shoreline position, and estimation of tsunami inundation zone.

SAR is a radar that emits microwaves towards the surface of the earth and measures backscattering. In this case, it is possible to set various observation conditions, the scattering characteristics of the object are various, and so the scenes acquired by the SAR are more readable than the scene of the visible light observation which can be understood intuitively. We used the SAR data observed by radar PALSAR and PALSAR-2, which are installed in a satellite called ALOS and ALOS-2, launched by the Japan Aerospace Exploration Agency (JAXA) in 2006 and 2014, respectively. Details of the ALOS observation image at Kashima

Coast, Japan is shown in **Figure 2.6**. It can be seen that SAR cover the broad spatial range; however, the temporal update is limited in a year. From 2009 to 2015, shoreline positions in the southern part of Kashima coast extracted from the captured SAR image, which is shown in **Figure 2.7**. The processed shoreline data is supplied by Takewaka et al. (2018).

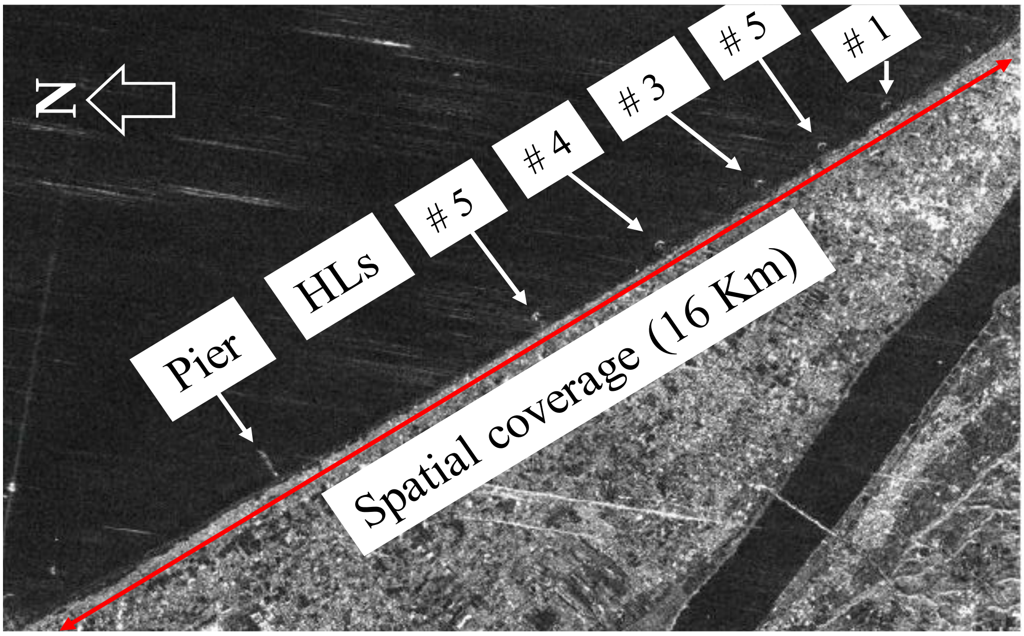

Figure 2.6. Example of ALOS- PALSAR acquired image.

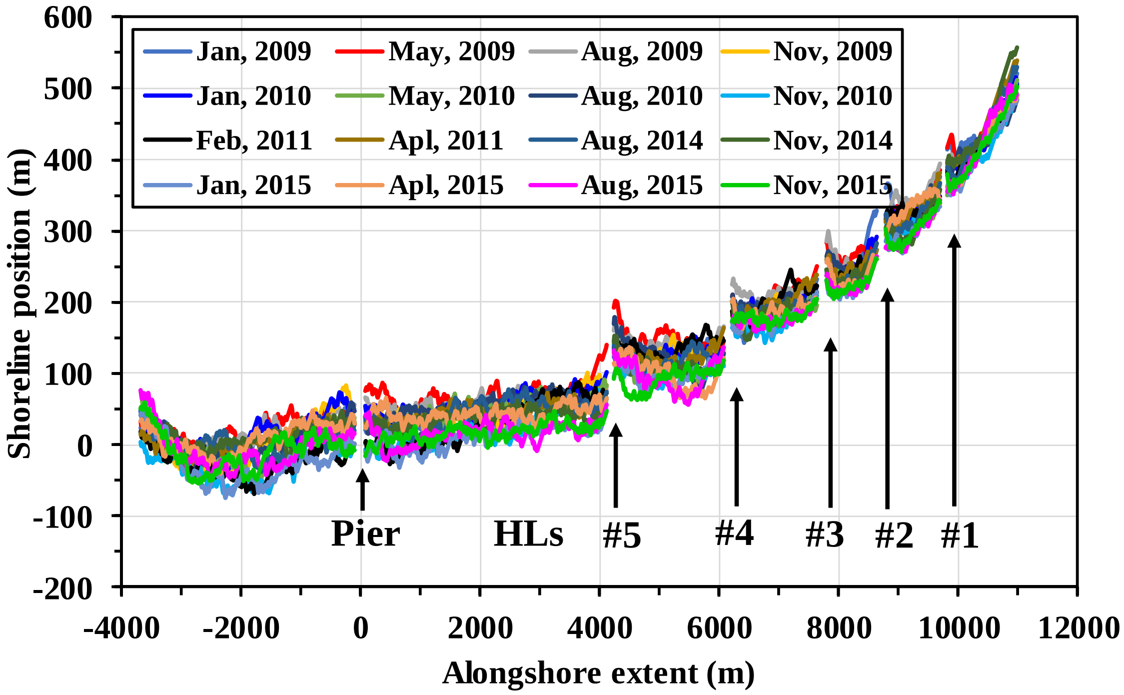

Figure 2.7. Shoreline position in the southern part of Kashima coast extracted from the captured SAR image during 2009 – 2015.

2.4 Tide and wave data

The Japanese Meteorological Agency collects hourly tidal elevation data at Choshi Fishery Port and the interannual variation is shown in **Figure 2.8**(a). The tidal environment of this area is micro-tidal with tidal variability range approximately 1.5 m. **Figure 2.8**(b) – (d) show the variations in the significant wave height, period, and incidence angle, respectively. These data are measured every two hours at Kashima Port Station, where the mean water depth is approximately 24 m, as part of the Nationwide Ocean Wave Information Network for Ports and Harbors (NOWPHAS).

http://nowphas.mlit.go.jp/eng.html).

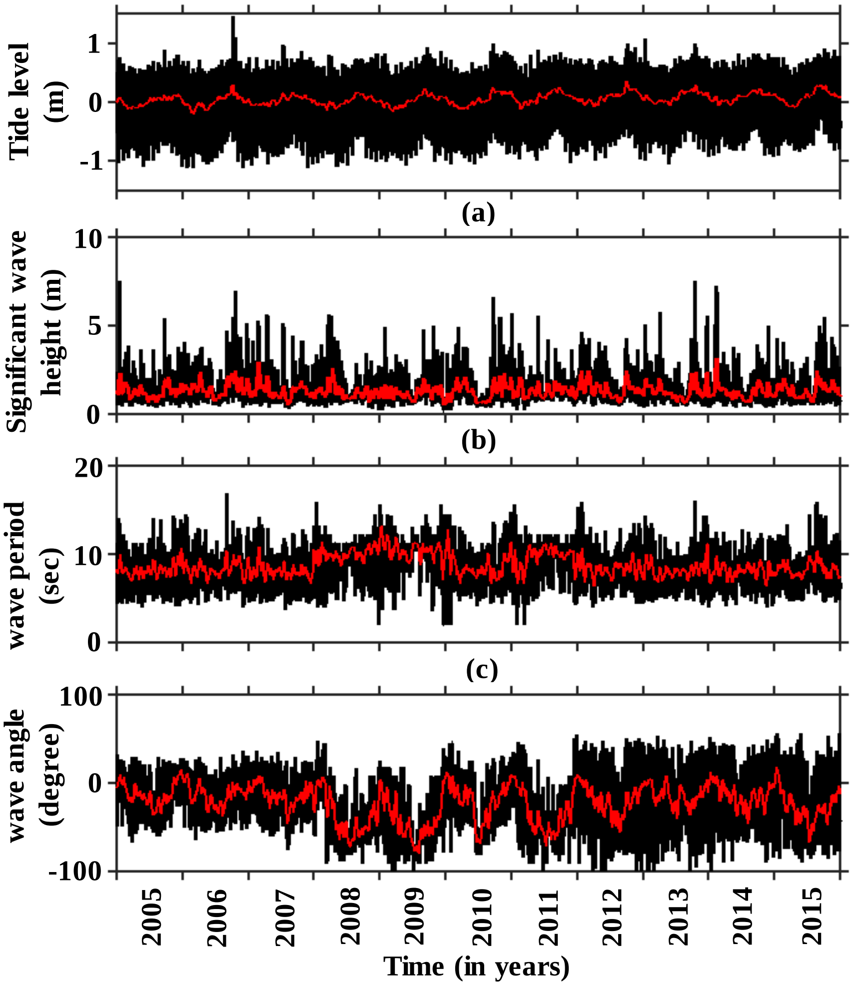

Figure 2.8. Temporal variation of (**a**) tide level, (**b**) significant wave height, (**c**) wave period, and (**d**) wave direction during 2005 – 2015. Red line indicates 14-days moving average.

2.5 Survey beach profile along to pier

Beach profiles along the research pier were measured at 5 m intervals every day from -110 m to 385 m, except on weekends and national holidays. **Figure 2.9**(a) illustrates an example of a surveyed beach profile and **Figure 2.9**(b) shows the variation in beach profile during 2005 – 2008. **Figure 2.9**(c) displays the mean, maximum, and minimum beach profiles, whereas **Figure 2.9**(d) depicts their standard deviation. The small values of standard deviation and narrow envelopes indicate stable regions, while large standard deviations and wide envelopes are associated with regions of high variability regions. The right side of (a) indicates the aerial photo research pier.

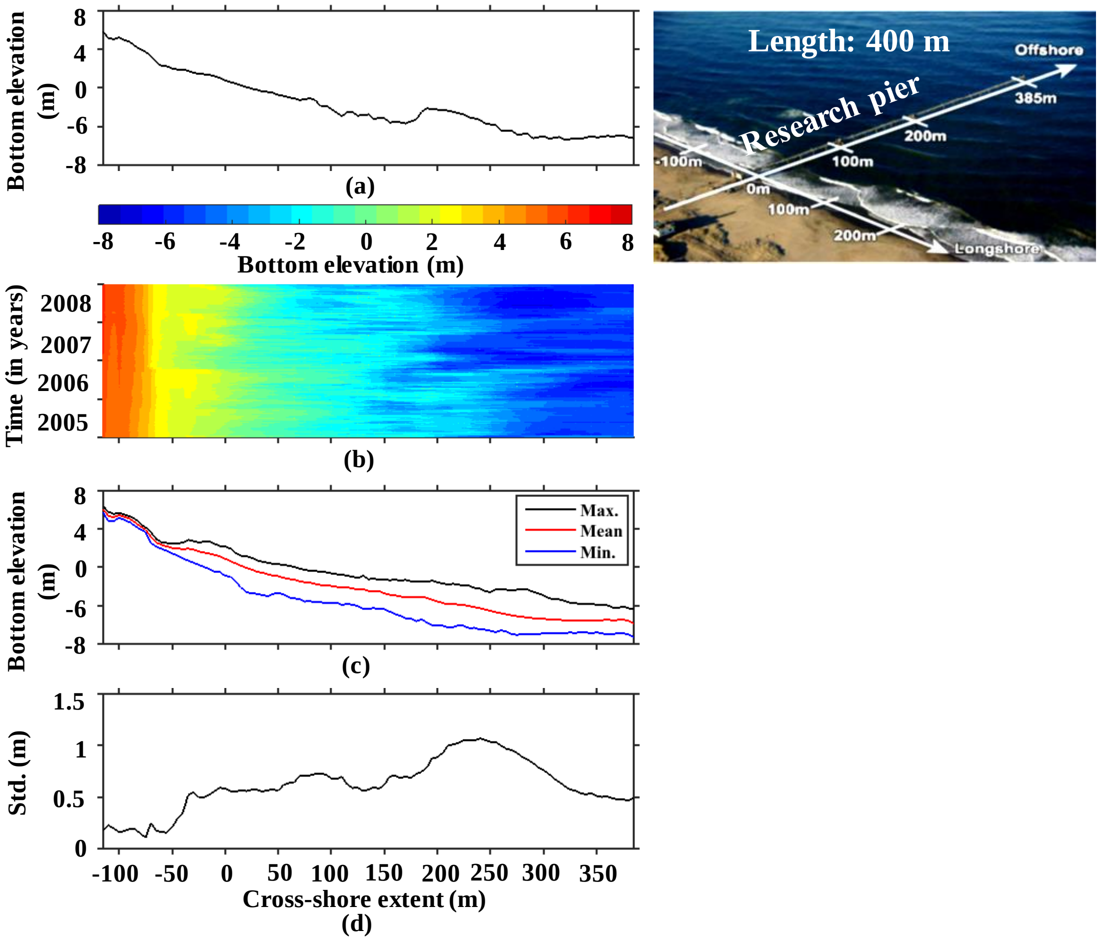

Figure 2.9. (**a**) Example of beach profile variation along the pier (18 April 2005 at 7.00), (**b**) beach profile variation during 2005 – 2008, (**c**) mean, minimum, and maximum range of beach profile, and (**d**) standard deviation. The right side of (**a**) indicates the aerial photo research pier, where beach profiles were measured along the research pier from -110 m to 385 m.

Intertidal survey shore profile is shown in **Figure 2.10**, where the water level consists between the height of -0.8 m and 0.8 m. The shoreline position is defined where the bottom elevation is equal to 0.0 m (T.P.). The intertidal foreshore slope is defined as the linear slope of the beach profile ranging between the height of -0.8 m and 0.8 m. Shoreline positions and intertidal foreshore slopes extracted from intertidal shore profile using the schematic illustration in **Figure 2.11**. **Figure 2.12**(a) and (b) show the variations in shoreline positions and intertidal foreshore slopes during 2005 – 2008.

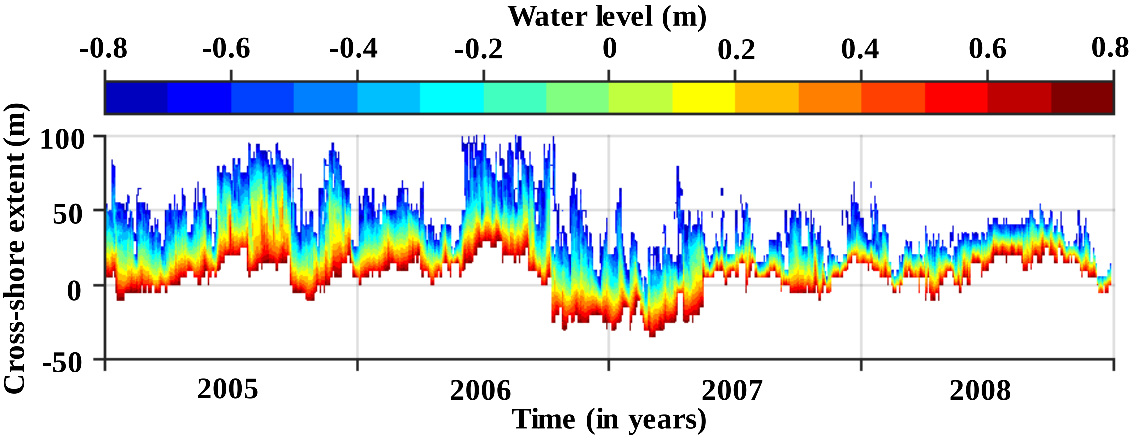

Figure 2.10. Intertidal shore profiles from survey data, where water level consists between -0.8 m to 0.8 m.

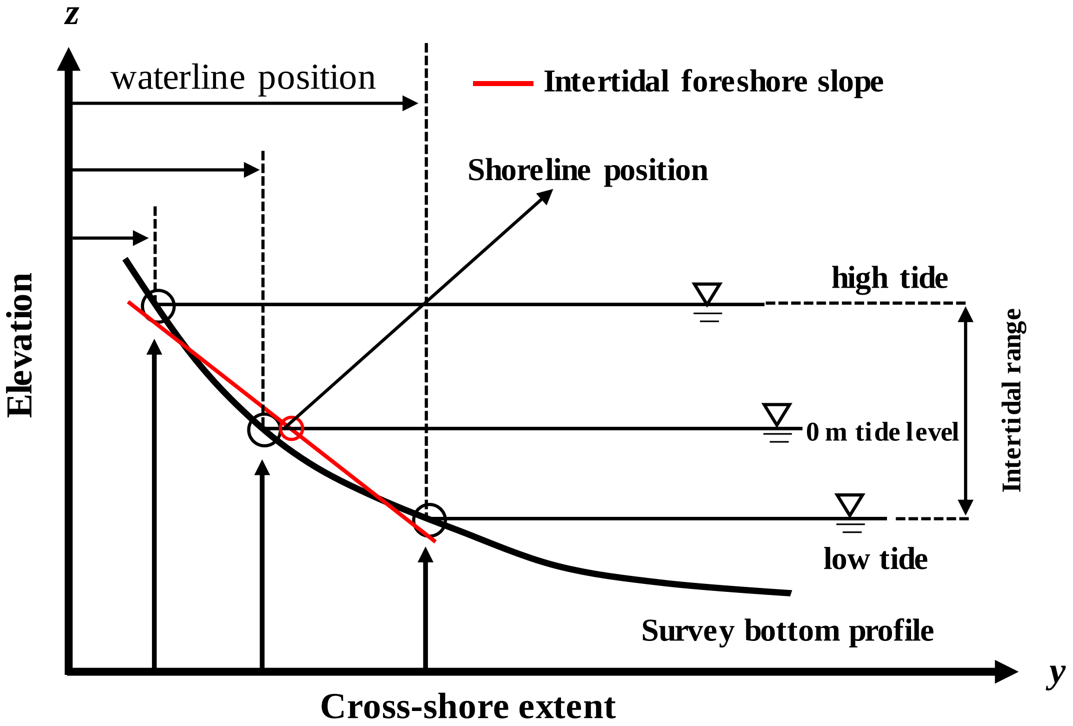

Figure 2.11. Schematic illustration of the mapping of intertidal bathymetry.

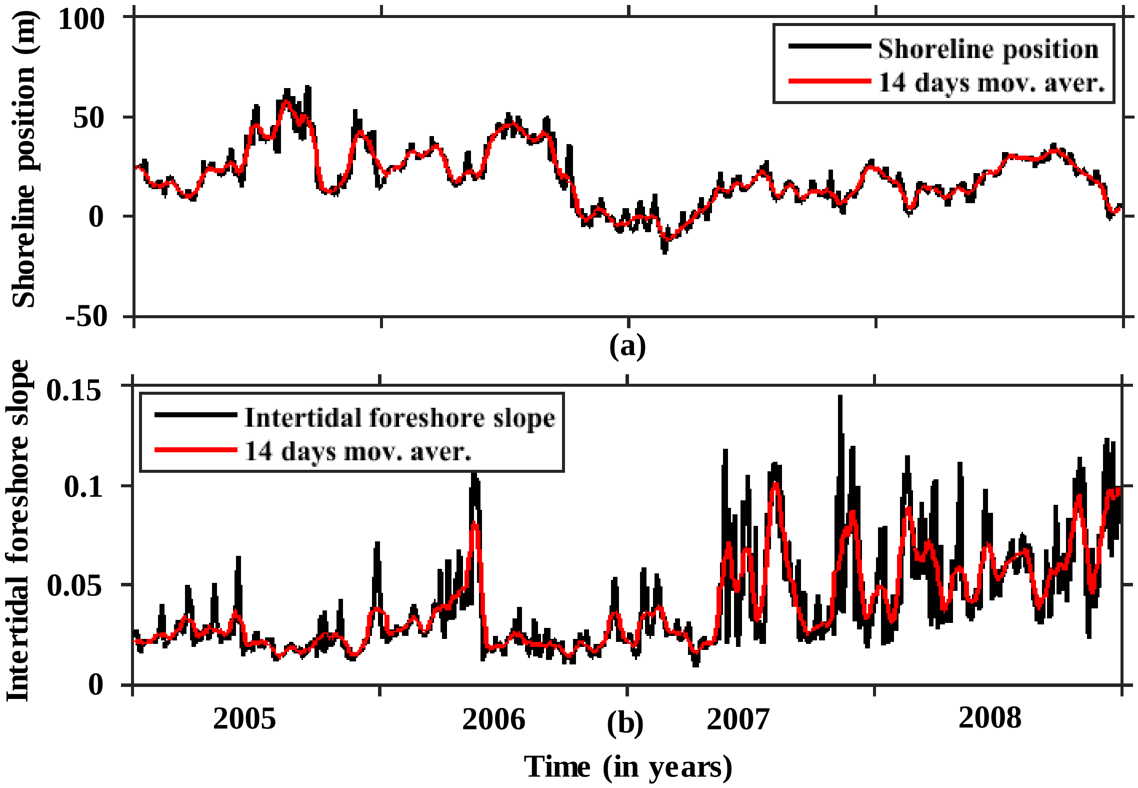

Figure 2.12. Temporal variations in (**a**) shoreline positions, and (**b**) intertidal foreshore slopes at the research pier. Red line indicates 14 days moving average of shoreline positions and intertidal foreshore slopes.

2.6 Aerial laser survey shoreline position

As previously mentioned, an aerial laser survey is one of significant tool for beach monitoring. In this context, An and Takewaka (2015) analyzed the shoreline variabilities at Kashima Coast by aerial photographs and aerial laser surveys from 2005 to 2013. After analyzed of recent years (2009 – 2013), they found that the trends in distributions of the shoreline positions indicate that fairly considerable amounts of accumulations are observed at the southern portions near Hasaki Fishery Port at Kashima Coast.

In this study, aerial laser survey data is used to validate the estimated data fusion shoreline position. Survey data is taken in May of 2011; however, the exact date is unknown. The outcome of the shoreline position distributions is depicted in **Figure 2.13**. It is mentionable that the tidal correction is only considered for this aerial laser survey data.

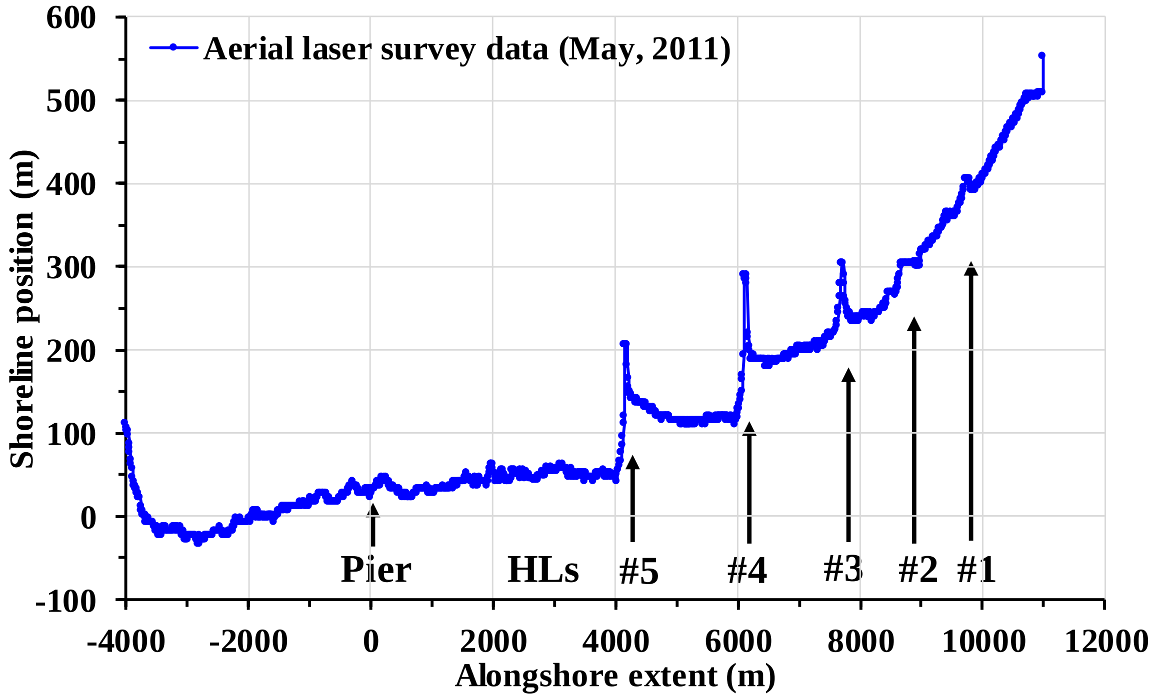

Figure 2.13. Distributions of the shoreline positions at May 2011 determined by aerial laser survey.

CHAPTER THREE : SHORELINE POSITIONS AND INTERTIDAL FORESHORE SLOPES DETECTION

3.1 Introduction

The social and economic significance of monitoring and managing shorelines have great impact on coastal regions around the world. Based on the significance, coastal scientists and engineers are continuously seeking better tools to determine the accurate position of the physical interface of coastal land and mean water level position, which is known as shoreline (Dolan et al., 1980; Boak and Turner, 2005). There have been many techniques such as manual, semi-automatic and automatic to detect shoreline position from distinct monitoring tools such as situ beach profiling, LIDAR surveys, aerial photography, video camera analysis, satellite imagery, Synthetic Aperture Radar (SAR), land-based X-band radar and so on. Among them, automatic detection technique is determined the shoreline positions more accurately from the individual monitoring tools within very quick time. Recently, Bell et al. (2016) was first developed the Temporal Waterline Method (TWM) which detects the intertidal shore profile automatically from cross-shore pixel intensity variation in time averaged X-band images and binary representation of tide records. However, the original TWM does not perform correctly to detect the intertidal shore profile as well as was unable to the time-series shoreline positions and intertidal foreshore slopes from X-band radar images of an entirely sandy, highly varied, and micro-tidal beach site at Hasaki Oceanographical Research Station (HORS) in Hasaki, Japan. Hence, the modified Temporal Waterline Method (mTWM) is introduced and applied to extract the time-series of shoreline positions and intertidal foreshore slopes in Hasaki Coast, Japan. The limitations of TWM and advantages of mTWM will be also discussed.

The mTWM exploits the excellent temporal update rates provided by the land-based remote sensing, while it could uniformly be used to a wide range of remote sensing data with the adequate number of images. Accordingly, in this study, 31,888 X-band radar images, which were captured during the period of 12 April 2005 to 31 December 2008, were used to measure the shoreline positions and intertidal foreshore slopes.

The objective of this chapter is to focus on the application of modified approach of TWM on X-band radar images to a highly erodible micro-tidal sandy beach exposed to energetic waves of the south Pacific Ocean with a comparison of the shoreline position and intertidal foreshore slope results with daily beach profile survey along the pier in the four years from 2005 – 2008.

3.2 Shoreline positions and intertidal foreshore slopes detection

The TWM was developed by Bell et al. (2016) to extract intertidal beach profile from time-averaged X-band radar images considering tidal variation and mTWM is the modified form of Bell et al. (2016) approach. First, the basic concept of TWM and then our modification is described in this subsection.

3.2.1 Intertidal beach profile and shoreline estimation using TWM and mTWM

Time-series of individual radar pixel intensities are gathered from hourly time-averaged images across the selected timescale of two weeks, including a full spring-neap cycle (as an example, 17–30 June 2005), which is shown in **Figure 3.1**(a). **Figure 3.1**(b) displays the cross-shore time stack images within the range between $y = 5\,m$ and $y = 103\,m$. The red line marked in **Figure 3.1**(c) indicates the variation of waterline position digitized manually by visual inspection, and **Figure 3.1**(d) is the concurrent tidal records. In general, the instantaneous waterline position is the boundary between coastal land and water at one instant in every measurement. It can be clearly seen that the instantaneous waterline position moves seaward when the tide ebbs and vice versa (see **Figure 3.1**(c) and **Figure 3.1**(d)).

Shoreline position is defined where the bottom elevation is equal to 0.0 m (T.P.) and the intertidal foreshore slope is defined as the linear slope of the beach profile ranging between the height of -1 m and 1 m. Using the manually digitized instantaneous waterline position (**Figure 3.1**(c)) and con-current tide records (**Figure 3.1**(d)), the shoreline position is established at *y* = 23.5 m from its origin and the intertidal foreshore slope is 0.018, which is shown in **Figure 3.2**.

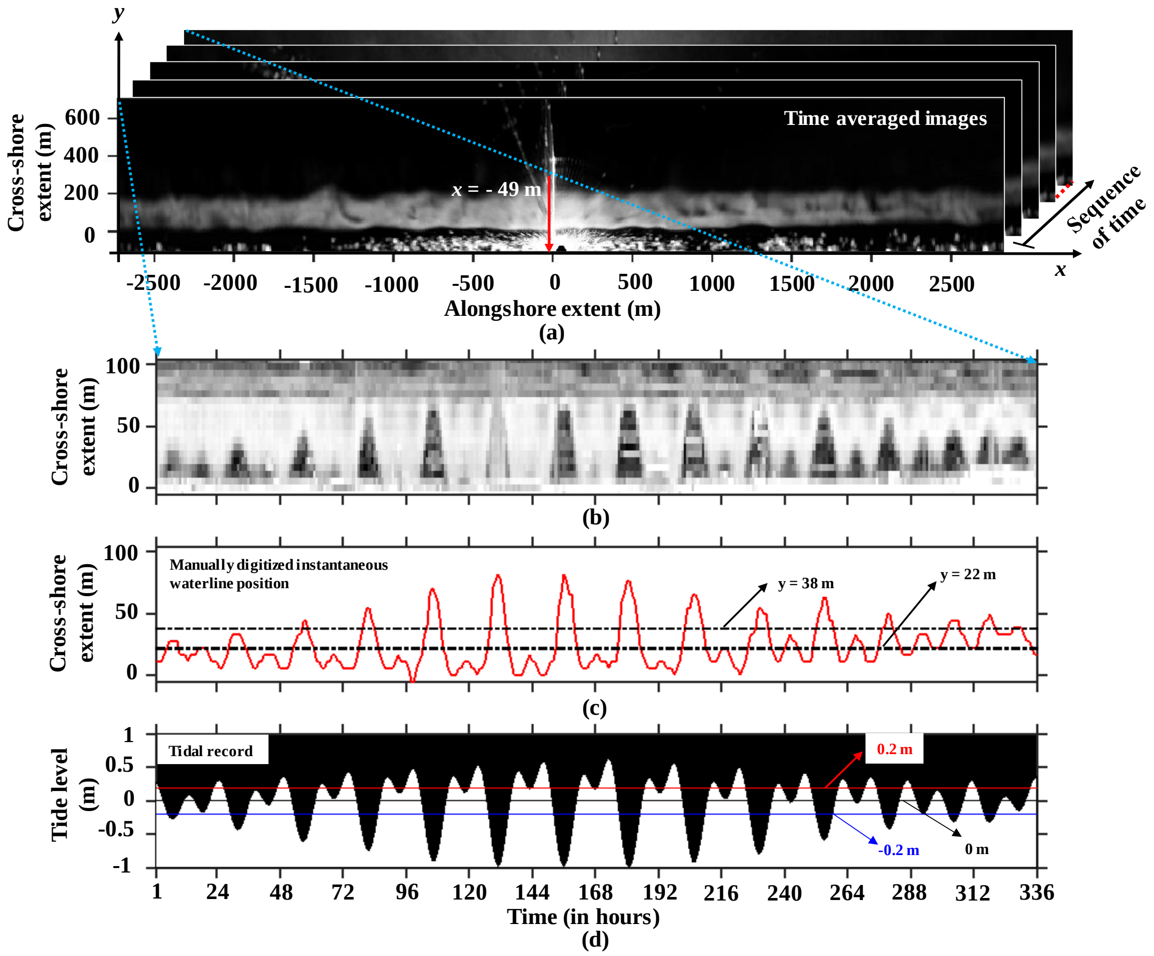

Figure 3.1. (**a**) Time-series of individual radar pixel intensities are gathered from hourly time-averaged images across the selected timescale of two weeks, (**b**) cross-shore time stack image between cross-shore extent, *y* = -5 – 103 m at *x* = – 49 m, (**c**) manually digitized waterline positions from cross-shore time stack image, and (**d**) tidal record during 17–30 June 2005. Instantaneous waterline position shifts seawards when the tide falls and vice versa.

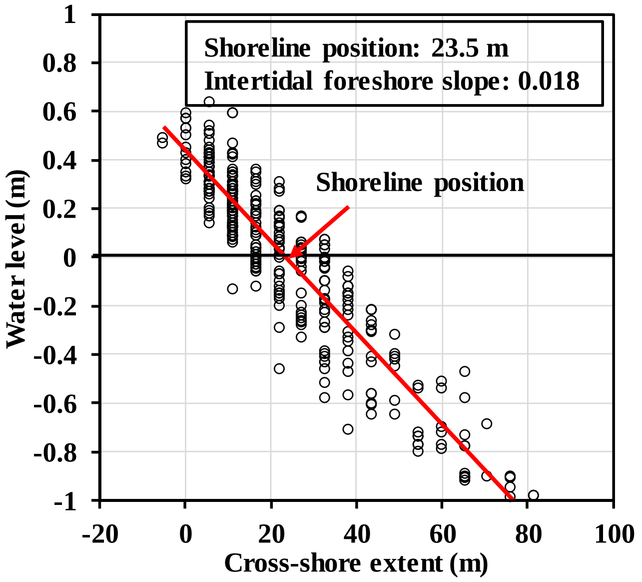

Figure 3.2. Example of linear fitting intertidal beach profile at $x = -49$ m. Datum of elevation is from the tide records, and individual waterline positions are from manual digitization on the time averaged image during 17–30 June 2005. Shoreline position is established at $y = 23.5$ m, where the bottom elevation is equal to 0.0 m and intertidal slope (0.018) is defined the regression coefficient between water level -1 m to 1 m.

At a longshore point x, pixel intensity from intertidal zone at y is extracted from time-averaged images and repeated for two weeks, which yields $P\ (y, n)$, where n is time. **Figure 3.3**(a) – (d) illustrate the variations in pixel intensities over a two weeks period, showing the periodic episode. High pixel intensities are acquired from time-averaged images when the waterline clearly appears, and vice versa.

The tidal elevation range between -0.8 and 0.8 m is considered with 0.1 m increments to generate binary pulse sequence, which are hereafter indicated with water level number N ($N = -8, -7, \dots\dots, 8$). The study site exhibits a micro-tidal influence with tidal variability range of approximately 1.5 m. Each tidal elevation within a given tidal range of -0.8 – 0.8 m with 0.1 m increment has a unique binary pulse signal that representing 1 and 0, where 1 and 0 indicates a binary pulse sequence above and below water level at a given water level of tidal cycle. Each elevation produced a unique binary pulse sequence, which is defined by $T_N(n)$, as illustrated in **Figure 3.3**(e) – (g) for $T_{N=-2\ (-0.2\ \mathrm{m})}$, $T_{N=0\ (0.0\ \mathrm{m})}$, and $T_{N = 2\ (0.2\ \mathrm{m})}$, respectively. As shown in **Figure 3.3**, the extracted pixel intensities from radar images and binary pulse signal at water levels have signal similarities.

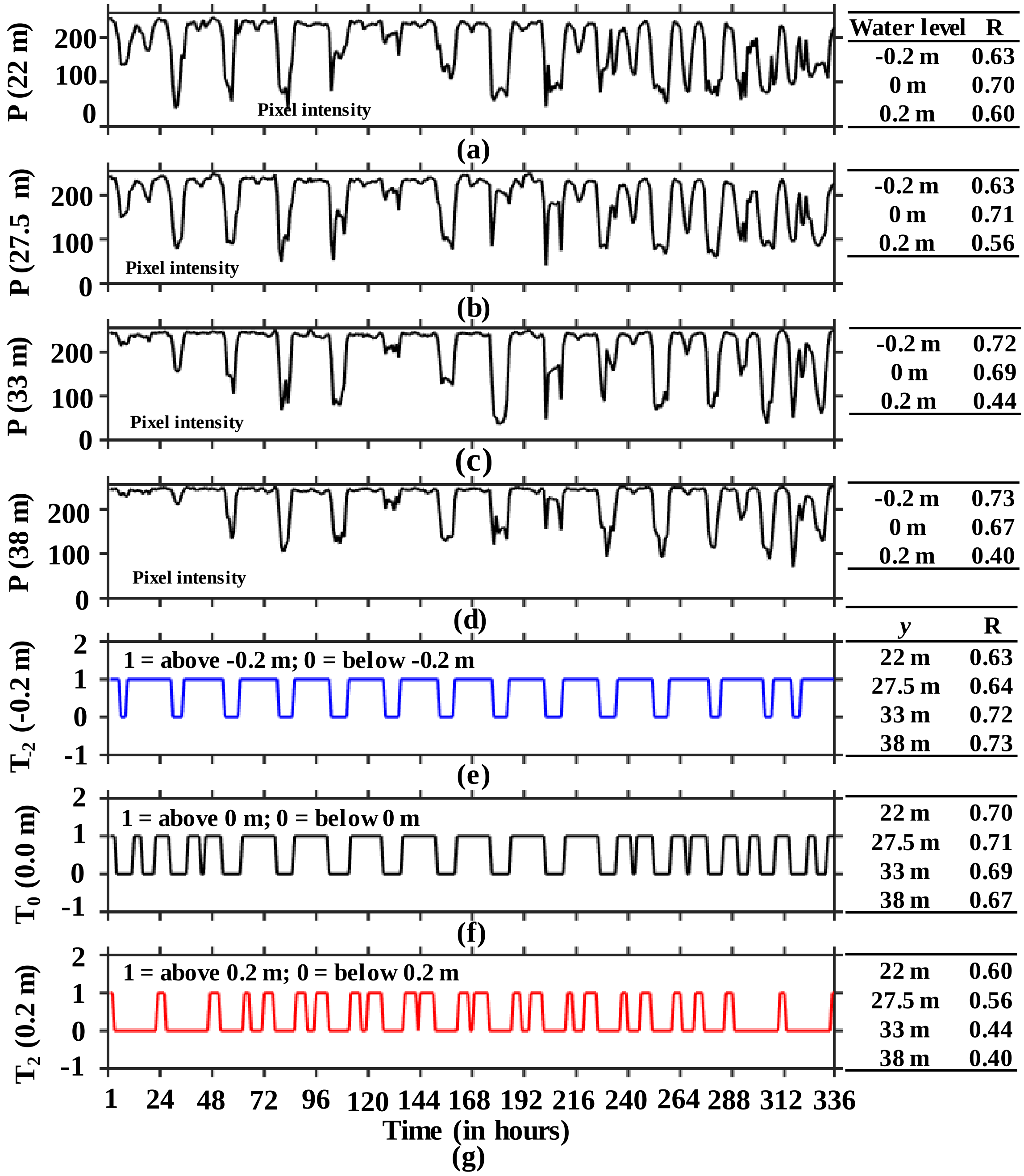

Figure 3.3. Pixel intensities over two weeks (17–30 June 2005) at $x = -49$ m (**a**) $y = 22$ m, (**b**) $y = 27.5$ m, (**c**) $y = 33$ m, and (**d**) $y = 38$ m; (**e**) Tidal binary signal indicating above or below water level -0.2 m; (**f**) water level 0.0 m; (**g**) water level 0.2 m; Tables at the right-hand side of (e) to (g) illustrate correlation coefficients between pixel intensity variation (y = 22 m, 27.5m, 33 m, 38 m) and tidal binary signals. Higher correlation value shows strong similarities between pixel intensity variation and binary signal representation of tide records.

Now, the correlation coefficient $R(y, N)$ is calculated at each possible elevation to measure the signal similarities between the pixel intensity variation $P\ (y, n)$ at different cross-shore extents, in addition to the tidal binary pulse sequence $T_N(n)$ for different water level numbers:

$$R(y, N) = \frac{\sum_{n=1}^{24\times14}\{(P(y,n)-\bar{P}(y))(T_N(n)-\overline{T_N})\}}{\sqrt{\sum_{n=1}^{24\times14}(P(y,n)-\bar{P}(y))^2}\ \sqrt{\sum_{n=1}^{24\times14}(T_N(n)-\overline{T_N})^2}}. \qquad (1)$$

where $\bar{P}(y)$ is the mean pixel intensity, and $\overline{T_N}$ is the mean tidal binary pulse sequence over two weeks. A high correlation value indicates the strong signal similarities between the pixel intensity variation and binary representation of the tidal record sequence, which describes the implication for bottom elevation.

The tables at the right-hand side of **Figure 3.3**(a) – (d) illustrate the correlation coefficient between each tidal binary signal pulse (-0.2 m, 0 m, 0.2 m) with individual pixel intensity variation, and **Figure 3.3**(e) – (g) illustrate the correlation coefficient between the pixel intensity variation at P (*y* = 22 m), P (*y* = 27.5 m), P (*y* = 33 m), and *P* (*y* = 38 m) with individual of the tidal binary signal pulse of $T_{N\,=\,-2}$, $T_{N\,=\,0}$, and $T_{N\,=\,2}$, respectively. The maximum correlation coefficient is used to indicate the cross-shore position at a certain water level and the process is repeated for all binary signal tidal elevation extracted from tide records. The outcomes are then utilized to plot a correlation map for a given longshore extent (*x* = – 49 m) at different water levels (-0.8 – 0.8 m with 0.1 m increments) within the intertidal range (*y* = 0 – 80 m with 5.4 m increments), as shown in **Figure 3.4**. Here, no correlation coefficients are available at the water levels of 0.6 – 0.8 m because the correlation values less than 0.2 at the 0.6 m level and the tide level did not reach 0.7 m and 0.8 m levels.

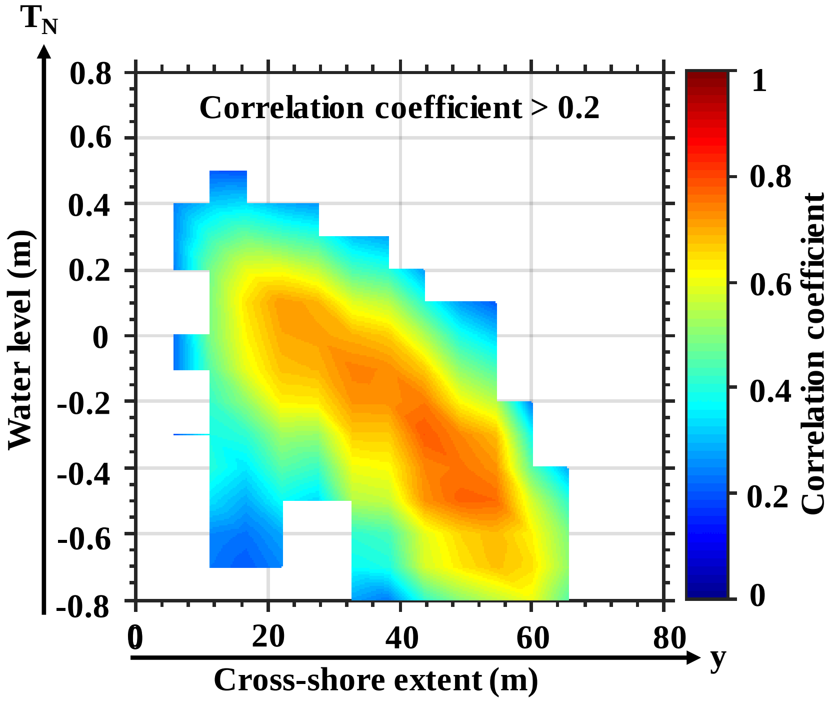

Figure 3.4. Distribution of correlation coefficients for different tidal signals (-0.8 – 0.8 m) and cross-shore positions ($0 \leq y \leq 80$ m) at $x = -49$ m during 17–30 June 2005.

By using the correlation coefficient map from **Figure 3.4**, the intertidal shore profile can be determined in the following two ways:

(i) To detect a water level from a cross-shore position correlation coefficient distribution, where the distribution is maximum. The detected point is regarded as the bottom elevation. Similarly, the maximum correlation at other water levels are estimated throughout the remaining cross-shore positions, and the intertidal cross-shore profile is determined. The described approach is known as TWM, which was initially introduced by Bell et al. (2016), and

(ii) To detect a cross-shore position from the distribution of correlation coefficient across a water level, where the distribution is maximum. The detected point is also regarded as the bottom elevation. Proceeding the same way, the maximum correlation is established at other cross-shore positions across the remaining water levels, and the intertidal cross-shore profile is produced. The stated approach is called mTWM, which is the modified form of Bell et al. (2016) approach.

Figure 3.5(a) shows an example of correlation map for a given longshore extent (x = – 49 m) at different water levels (-0.8 – 0.8 m with 0.1 m increments) within the intertidal range (y = 0 – 80 m with 5.4 m increments). The red arrow line indicates an example of the cross-shore position transect at y = 27.5 m. **Figure 3.5**(b) shows the correlation coefficient distribution at y = 27.5 m extracted from the map within the water levels range (-0.5 – 0.4 m). The maximum correlation is established at 0.0 m water level, which is regarded as the bottom elevation of this point. Similarly, the maximum correlation at other water levels are determined among the remaining cross-shore positions and the intertidal cross-shore profile is estimated. Then, a linear fitting model is applied to determine the shoreline position at 0.0 m water level, and the intertidal foreshore slope is calculated from regression line coefficient within the intertidal range. As shown in **Figure 3.5**(c), shoreline position is determined at y = 24.3 m, and intertidal foreshore slope is 0.017. Compared to the surveyed shore profile, we observed that the TWM failed to estimate the intertidal shore profile accurately from radar images.

In TWM, to look for water levels from the distribution of the correlation coefficient along the cross-shore positions, the maximum correlation coefficient is frequently established between -0.8 m and 0.4 m water levels. Due to the strong signal similarities between cross-shore position pixel intensities extracted from images and the tidal binary pulse signal (-0.8 – 0.4 m), the high correlation coefficient frequently appears in these water levels. In another sense, the original TWM cannot detect the water levels (0.5 – 0.8 m) due to the presence of lower correlation coefficients than other water levels (-0.8 – 0.4 m). As a result, the TWM failed to estimate actual intertidal shore profile and was unable to determine the shoreline position and intertidal foreshore slope with a significant bias.

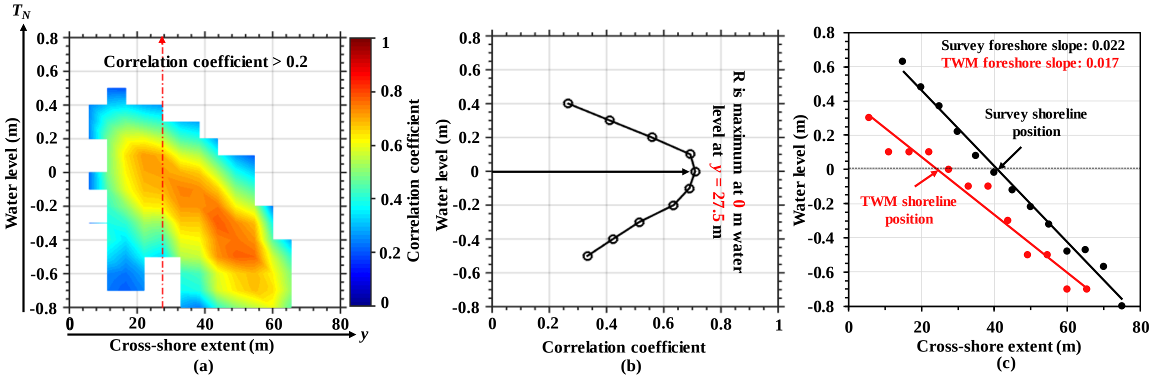

(a) (b) (c)

Figure 3.5. Example of TWM detected beach profile at $x = -49$ m during 17–30 June 2005. (**a**) Distribution of correlation coefficients for different tidal signals (-0.8 – 0.8 m) and cross-shore positions ($0 \leq y \leq 80$ m), (**b**) correlation coefficients for different tidal binary signals at $y = 27.5$ m. Maximum correlation is established at water level 0.0 m. (**c**) Intertidal beach profile determined by linear regression. Shoreline position ($y = 24.3$ m) is defined at water level 0.0 m, and the black regression line indicates survey intertidal beach profile on 17 June 2005.

Landwards cross-shore position pixel intensities have no periodic oscillation like tidal binary pulse signal, which is due to the irregularity of water line with time for each transition. In such reason, cross-shore position pixel intensities and tidal binary pulse signals provide poor and almost identical correlation coefficient values. Therefore, cross-shore direction-wise water levels detection technique (TWM) is failed to estimate the expected objects. Under a changed search direction (mTWM) to find the bottom elevation, the extracted intertidal shore profile becomes closer to the survey profile. The above-described bottom elevation finding approach is considered as the modification in this study. Prior to estimating the intertidal shore profile, the input of the intertidal range was selected from tidal elevation data. In order to ensure each of water levels in the intertidal shore profile, it is expected that water level direction-wise cross-shore position detection is more appropriate than TWM. The performance of this approach will be described later.

Figure 3.6(b) displays a correlation map for a given longshore extent ($x = -49$ m) at different water levels (-0.8 – 0.8 m with 0.1 m increments) within the intertidal range (*y*

= 0 – 80 m with 5.4 m increments). The red arrow line indicates an example of 0.0 m water level transect. **Figure 3.6**(b) shows the correlation coefficient distribution at water level 0.0 m extracted from the map within the cross-shore extent range ($0 \leq y \leq 80\,m$). The maximum correlation is established at y = 27.5 m cross-shore position, which is regarded as the bottom elevation of this point. Similarly, the maximum correlation at other cross-shore positions are determined among the remaining water levels and the intertidal cross-shore profile is estimated. Then, a linear fitting model is applied to determine the shoreline position at 0.0 m water level, and the intertidal foreshore slope is calculated from regression line coefficient within the intertidal range. The shoreline position in **Figure 3.6**(c) is determined at y = 30 m, and the intertidal foreshore slope is 0.024. Authors have compared to the estimated slope with a survey intertidal profile slope on 17 June 2005. **Figure 3.6**(c) shows the mTWM estimated intertidal foreshore slope is found very close to survey intertidal foreshore slope; however, the extracted shoreline positions have some landward shifts compared to the survey data. On the other hand, TWM fails to estimate intertidal foreshore slope and shoreline position with a significant bias.

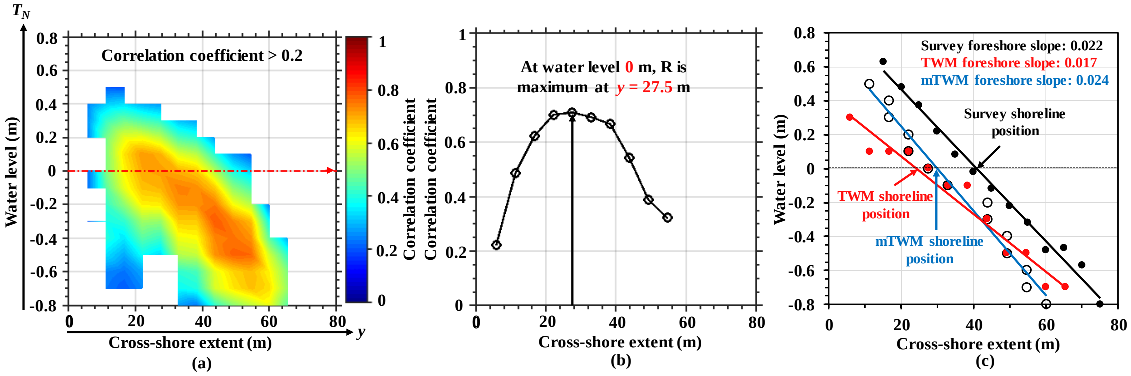

Figure 3.6. Example of mTWM detected intertidal beach profile at $x = -49$ m during 17–30 June 2005. (**a**) Distribution of correlation coefficients for different tidal signals (-0.8 – 0.8 m) and cross-shore positions ($0 \leq y \leq 80$ m), (**b**) distribution of correlation coefficients for cross-shore positions at a water level 0.0 m. Maximum correlation is established at y = 27. 5 m. (**c**) Intertidal beach profile determined by linear regression. Shoreline position (y = 30 m) is defined at water level 0.0 m. where the red and black regression lines indicate TWM and survey intertidal beach profile, respectively, on 17 June 2005.

The data collected over a two-week period are processed to obtain a shoreline position and an intertidal foreshore slope data. This process was repeated over the period between 12 April 2005 and 31 December 2008 to estimate the variations in shoreline position and intertidal foreshore slope. **Figure 3.7**(a) and (b) depict the variation in shoreline positions derived by TWM and mTWM compared to those obtained by survey data collected at the research pier; however, some random gaps are observed owing to the lack of strong waterline signals or the saturation of echo signals. The bias between the results obtained by survey data and mTWM derived results is presented in **Figure 3.7**(c), showing 14 m Mean Absolute Bias (MAB). A similar trend is observed between the shoreline positions estimated by mTWM and the survey data, which is confirmed by the correlation coefficient (R = 0.86) shown in **Figure 3.7**(d); however, a horizontal shift between the mTWM derived results and surveyed shoreline positions is detected. This shift is induced by the effect of wave set-up or wave run-up, and a combination of correction factors will be discussed in sub-sections 3.2.2 and 3.2.3. On the other hand, the calculated MAB between survey and TWM derived shoreline positions is 19.2 m, which is larger than the obtained MAB between survey and mTWM. The large number of random gaps appear in **Figure 3.7**(a) for the TWM estimation.

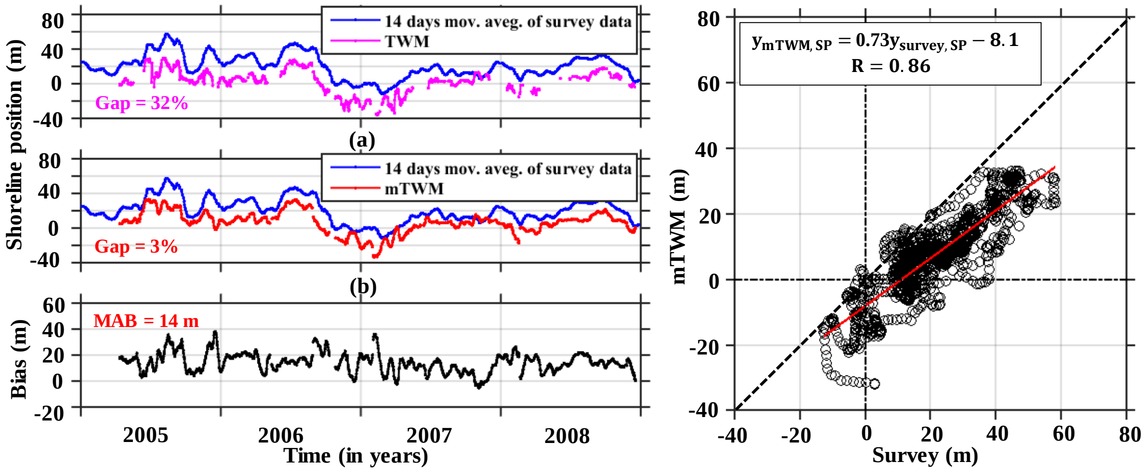

(c) (d)

Figure 3.7. Temporal variations in shoreline positions (SP) estimated from (**a**) survey data and TWM, (**b**) survey data and mTWM derived results (at x = – 49 m), (**c**) bias between survey and mTWM results, and (**d**) scatter plot of survey vs. mTWM. Red line represents linear fitting line.

Figure 3.8(a) and (b) present the temporal variations in intertidal foreshore slopes derived by mTWM during the study period, and survey data, and the bias between the obtained outcomes are shown in **Figure 3.8**(c). Compared to surveyed slopes, TWM estimated slopes are three times milder. That means TWM cannot estimates slopes accurately from radar images. The reason for this discrepancy is described above. In order to estimate the bias, the radar detected values at each time point were subtracted from the survey detected values. The surveyed slope is sometimes steeper than that estimated by the mTWM owing to comparing different cross-section transect estimated observations. This discrepancy can be attributed to the fact that survey data is collected along the research pier, while data used for the mTWM is extracted 49 m far from the research pier. In addition, a fixed gap is observed along the research pier ($- 49 < x < 65$ m) due to saturated echo signals.

Water flows typically faster around piers and abutments, making them susceptible to local scour or removal of sediment (Zhai, 2010). Due to local scour, sand is eroded around the pier and accumulated to near side. As a consequence, the cross-shore beach profile changes gradually along the pier, and beach slopes can be steeper than the surroundings. Authors have visited the study site several times and sometimes found steeper foreshore close to the pier. This may be one possible reason for the discrepancy in slopes estimation.

The mTWM is applied to all alongshore locations; the spatio-temporal variation in the shoreline positions and intertidal foreshore slopes for the entire area is obtained for the period between 12 April 2005 and 31 December 2008, as shown in **Figure 3.9**. The *x*-axis denotes alongshore extent, and the *y*-axis denotes the time history between 2005 and 2008. The color bar of **Figure 3.9**(a) indicates the landwards (blue) and seawards (red) shoreline positions from its origin. On the other hand, the color bar pattern of **Figure 3.9**(b) shows the milder (blue) and steeper (red) intertidal beach slopes. However, 3% of the estimates are missing owing to the previously mentioned reason.

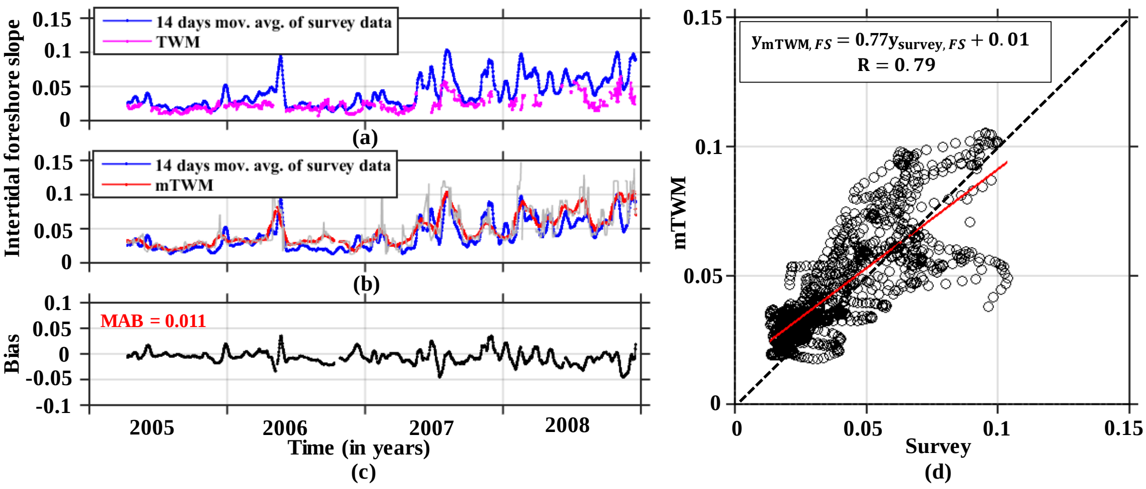

Figure 3.8. Temporal variations in intertidal foreshore slopes (FS) estimated from (**a**) survey data and TWM, and (**b**) survey data and mTWM derived results (at $x = -49$ m), where the off-white and red lines indicate mTWM derived intertidal foreshore slopes and its 14-day moving average, respectively. (**c**) Bias between survey and mTWM results. (**d**) Scatter plot of survey vs. mTWM.

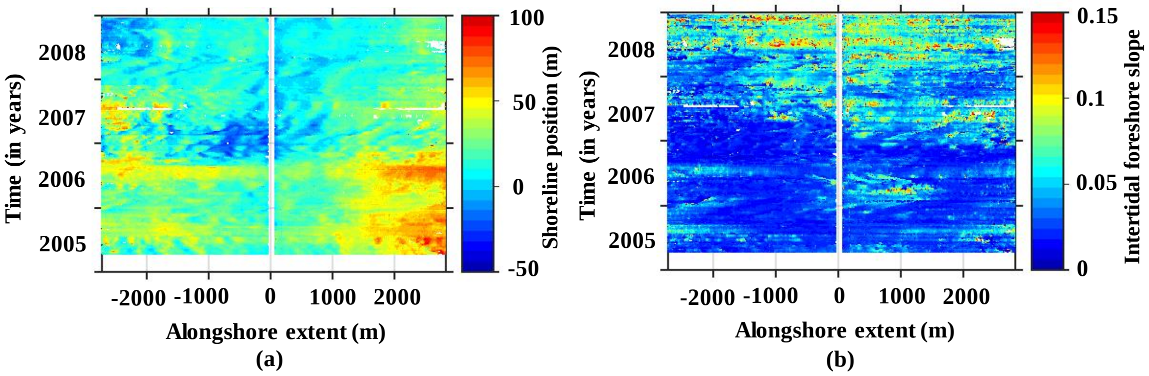

Figure 3.9. Spatial and temporal variations in (**a**) shoreline positions, and (**b**) intertidal foreshore slopes estimated by mTWM during 12 April 2005 and 31 December 2008.

3.2.2 Wave set-up correction

Wave set-up, defined as an increase in the mean water level above the still water level owing to momentum transfer to the water column with the presence of breaking waves, which is a common dynamic process in the nearshore zone (Lentz and Raubenheimer, 1999). Within the surf zone where wave breaking dissipates energy, the wave thrust decreases as the breaking surge travels shoreward, and consequently the mean water level rises, thus wave set-up occurs. **Figure 3.10**(a) is a schematic illustration of the wave set-up that indicates the corresponding rise in waterline. It shows that the mTWM estimated results are shifted landwards compared to survey data. Hence, the correction of wave set-up on the mTWM is essential to reduce the horizontal shifts in shoreline positions. Based on this schematic scenario, the following strategy is adopted to correct the wave set-up and obtain more accurate results by mTWM.

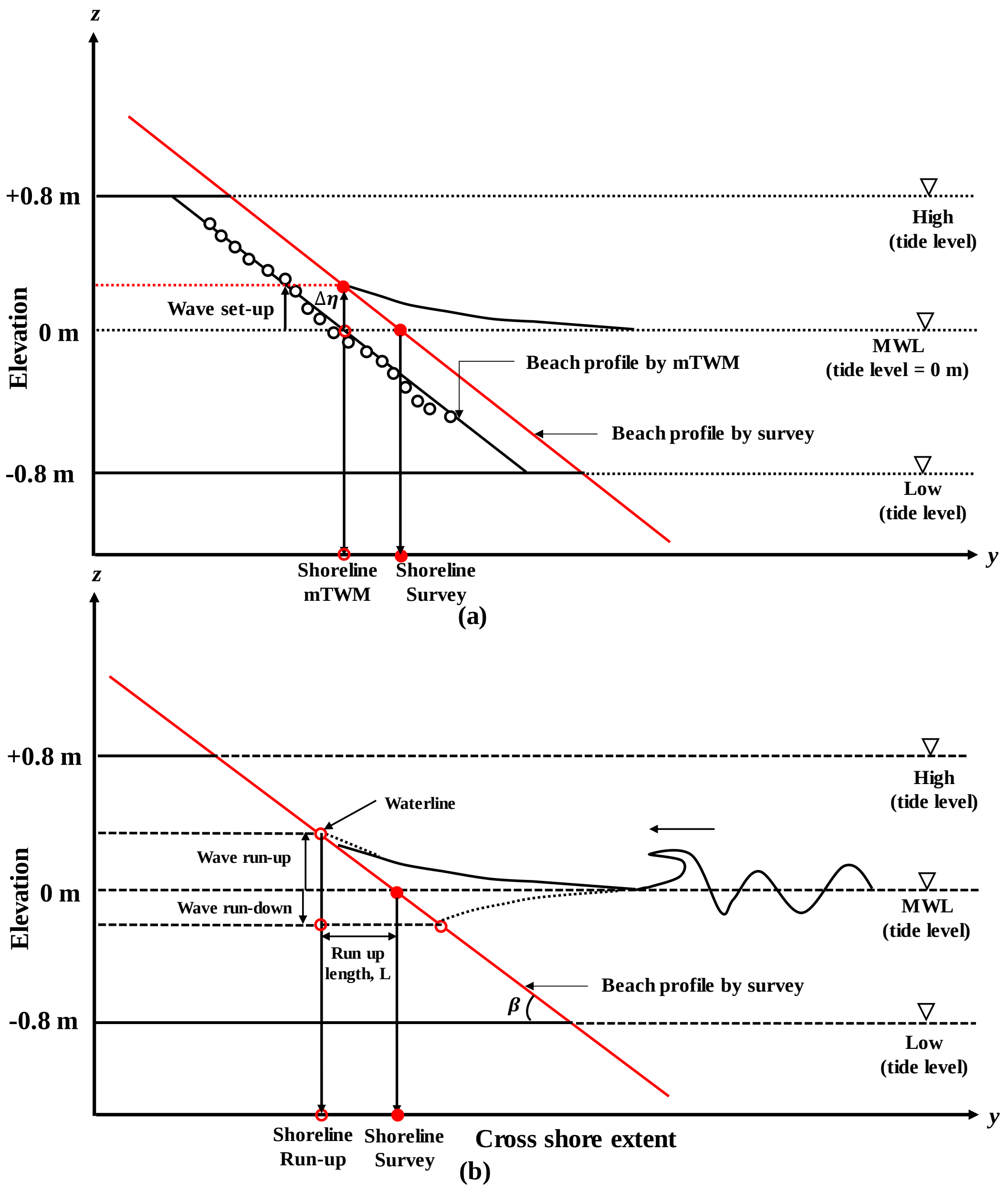

Figure 3.10. Schematic illustration of shift in estimated shoreline position due to (**a**) wave set-up, or (**b**) wave run-up.

Several studies have been conducted on the wave set-up on sloping beaches. In this study, the following empirical formula is used to estimate the amount of wave set-up (η) at Hasaki beach caused by normal wave incidence (Goda, 2010):

$$\frac{\eta}{H_0} = A_0 + A_1 log(H_0/L_0) + A_2\big(log(H_0/L_0)\big)^2, \tag{2}$$

and

$$\left.\begin{array}{r} A_0 = 0.0063 + 0.768\ tan\beta \\ A_1 = -0.0083 - 0.011\ tan\beta \\ A_3 = 0.00372 + 0.0148\ tan\beta \end{array}\right\} . \tag{3}$$

where, $\tan\beta$ is the bottom slope; H_0 is the offshore wave height, which is determined by the linear wave theory equation $H_1 = H_0 K_r K_s$, where K_r is the refraction coefficient, K_s is the shoaling coefficient, and H_1 is the NOWPHAS wave height; L_0 is the offshore wave length, which is determined by $L_0 = 1.56T^2$ and T is the wave period.

The amount of wave set-up $\Delta\eta$ at Hasaki beach due to oblique wave incidence is given by (Goda, 2010)

$$\Delta\eta = \eta \times (cos\theta_0)^{0.545+0.038\ log(H_0/L_0)}. \tag{4}$$

where θ_0 is the offshore wave direction estimated by Snell's law. In this calculation, NOWPHAS wave angle is used as the input for significant wave angle. **Figure 3.11**(a – g) show the wave period, NOWPHAS collected significant wave height, significant wave angle, estimated offshore wave angle, refraction coefficient, shoaling coefficient, and off-shore wave height. The amount of wave set-up is calculated for every two-hour time frame using Eqs. (2) – (4), as shown in **Figure 3.11**(h). In order to determine wave set-up, the mean beach slope (0.04) is used, which is extracted by the mTWM from radar images during 2005 – 2008.

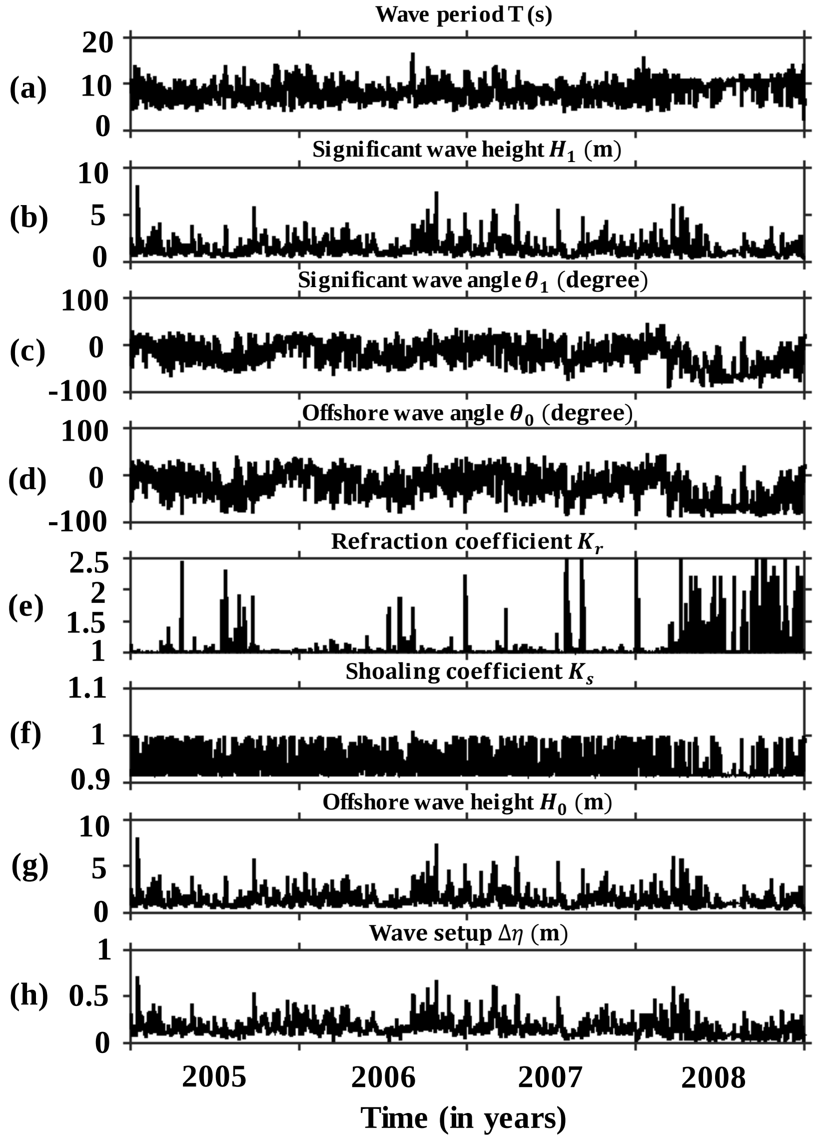

Figure 3.11. Temporal variation of (**a**) significant wave period, (**b**) significant wave height, and (**c**) significant wave direction measured at NOWPHAS Kashima station. (**d**) Offshore wave angle, (**e**) refraction coefficient, (**f**) shoaling coefficient, (**g**) offshore wave height estimated by linear wave theory, and (**h**) wave set-up.

A set-up corrected water level for the mTWM estimates is set by adding the wave set-up to the tide record, as shown in **Figure 3.12**. The corrected water level is shifted upward by approximately 0.17 m compared to the original tide record. A new correlation map is established with the corrected water level at x = – 49 m shown in **Figure 3.13**(a). The correlation coefficients obtained at 0.0 m water level at cross-shore positions ($0 \leq y \leq 80$ m) are shown in **Figure 3.13**(b) with red solid circles. The maximum correlation is now established at $y = 33$ m. Similarly, the obtained intertidal beach profile with corrected tide signal is shown in **Figure 3.13**(c). The results of linear regression analysis indicate the estimated shoreline position at $y = 34$ m with intertidal foreshore slope $\beta = 0.024$. The shoreline position is now shifted 4 m landwards, while the intertidal foreshore slope remains almost same.

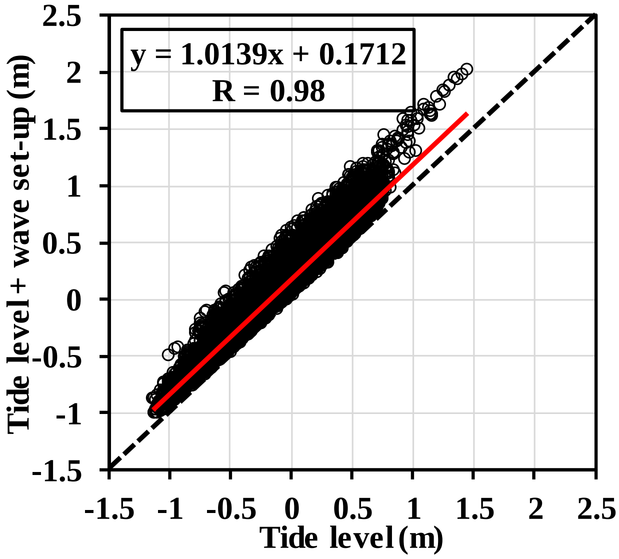

Figure 3.12. Scatter plot of tide level and tide level + wave set-up (2005 – 2008). Red line represents the linear fitting line.

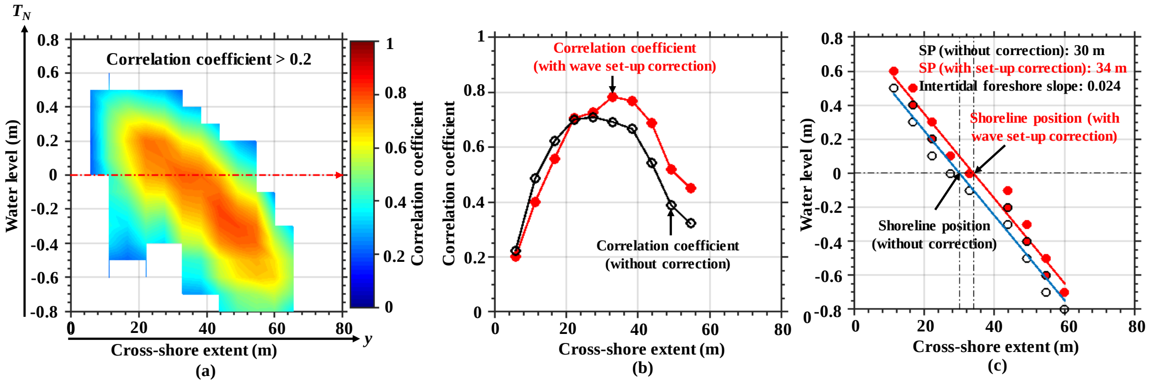

Figure 3.13. Example of mTWM detected beach profile at $x = -49$ m with corrected wave set-up during 17–30 June 2005. (**a**) Distribution of correlation coefficients between different tidal signals (– 0.8 to 0.8 m) and cross-shore positions ($0 \leq y \leq 80$ m). (**b**) Distribution of correlation coefficients for cross-shore positions at a water level 0.0 m (without and with corrected wave set-up). Maximum correlation is established at $y = 33$ m for corrected wave set-up. (**c**) Intertidal beach profile determined by linear regression. Shoreline position is defined at water level 0.0 m.

Figure 3.14(a) depicts a comparison between the survey and shoreline position with corrected set-up, and the vertical elevation bias between the survey and mTWM results with corrected wave set-up is shown in **Figure 3.14**(b). As shown in **Figure 3.14**(c), the correlation coefficient (R = 0.85) in both cases is almost equivalent to the previously obtained results. Similar trends are observed between the shoreline position obtained by the mTWM with corrected wave set-up and the survey data; however, the MAB of the estimated results dropped from 14 m to 10.5 m.

The variation in intertidal foreshore slope with corrected wave set-up that shown in **Figure 3.15** is similar to the previously mTWM estimated results.

Figure 3.14 and **Figure 3.15** confirm the effectiveness of the corrected wave set-up to determine the shoreline positions using the mTWM accurately. It allows shifting the estimated shoreline position landwards without changing the shape of intertidal beach profile.

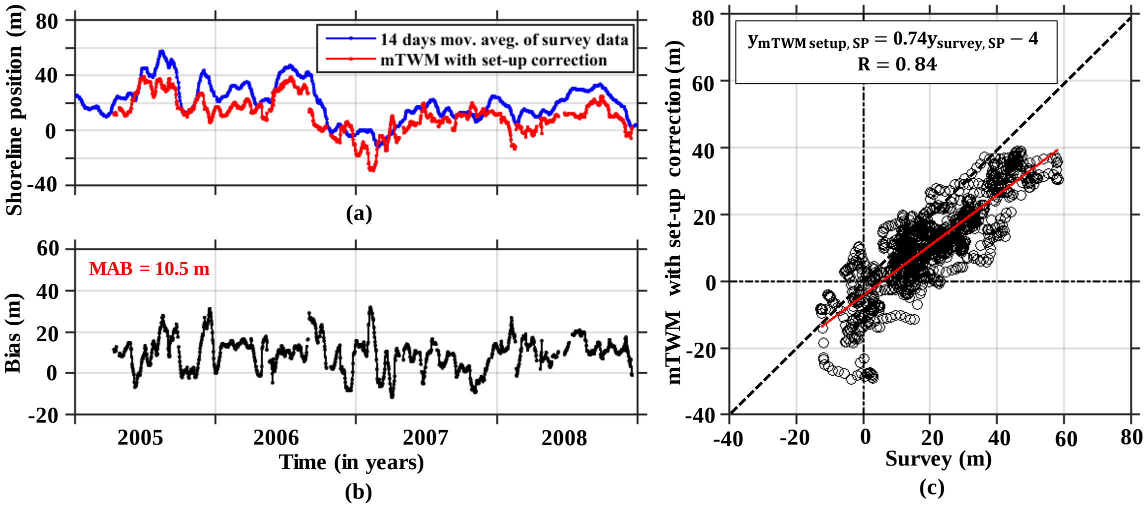

Figure 3.14. (**a**) Temporal variations in shoreline position (SP) estimated from survey data and mTWM derived results with corrected wave set-up (at *x* = – 49 m). (**b**) Bias between survey data and mTWM derived results with corrected wave set-up. (**c**) Scatter plot of survey vs. mTWM with corrected wave set-up. Red line represents linear fitting line.

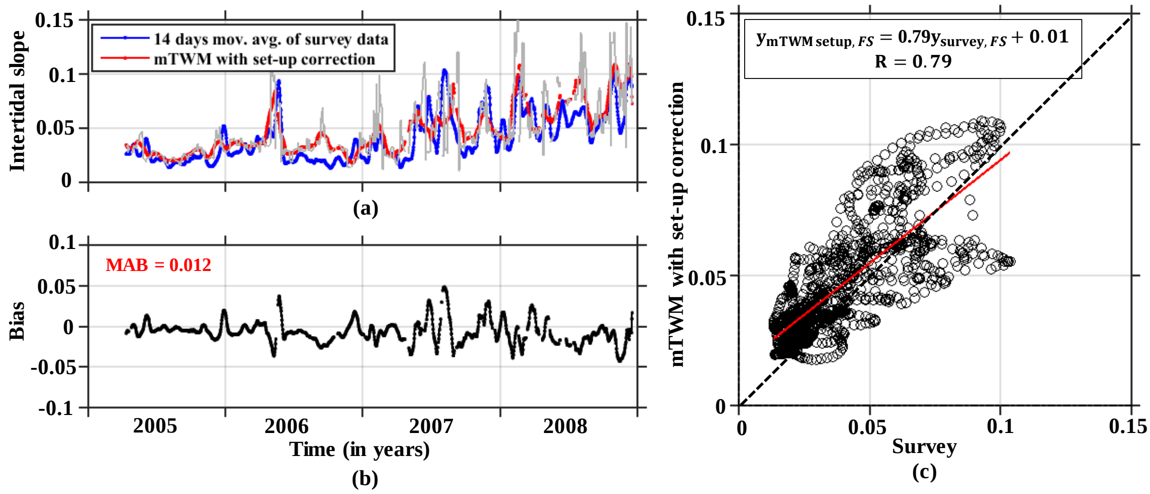

Figure 3.15. (**a**) Temporal variations in intertidal foreshore slope (FS) estimated from survey and mTWM derived results with corrected wave set-up (at *x* = – 49 m), where off-white and red lines indicate mTWM derived intertidal foreshore slope and its 14-day moving average, respectively. (**b**) Bias between survey data and mTWM derived results with corrected wave set-up. (**c**) Scatter plot of survey data vs. mTWM derived results with corrected wave set-up. Red line represents linear fitting line.

The mTWM with corrected wave set-up is applied to all alongshore locations; the spatio-temporal variations in the shoreline positions and intertidal foreshore slopes are obtained for the entire study site from April 12, 2005 to December 31, 2008, as shown in **Figure 3.16.** The *x*-axis corresponds to the longshore extent, and the *y*-axis is taken in the time history between 2005 and 2008. The color bar of **Figure 3.16**(a) indicates the landwards (blue) and seawards (red) shoreline positions from its origin. The color bar pattern of **Figure 3.16**(b) shows the milder (blue) and steeper (red) intertidal beach slopes.

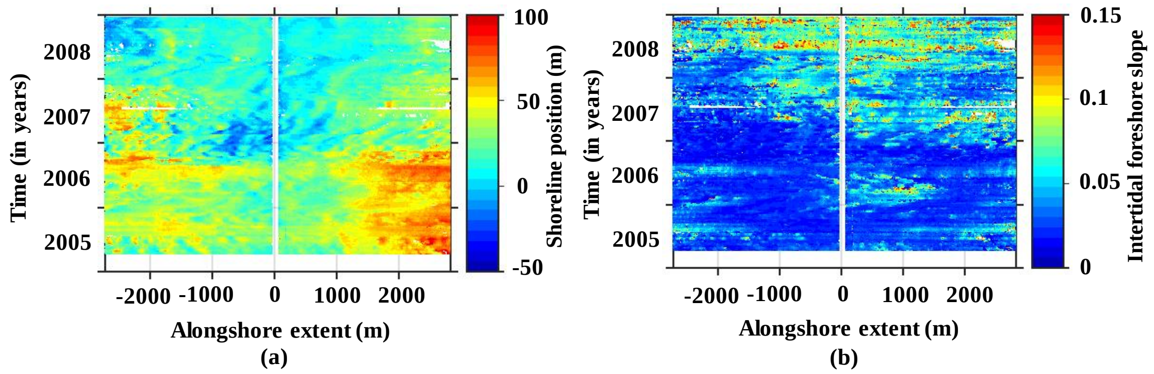

Figure 3.16. Spatial and temporal variations in (**a**) shoreline positions with corrected wave set-up, and (**b**) intertidal foreshore slopes with corrected wave set-up estimated by mTWM during 12 April 2005 and 31 December 2008.

3.2.3 Wave run-up correction

Wave run-up is defined as “the landward extent of wave uprush measured vertically from the still water level” (Melby, 2012). Accordingly, during high wave conditions, the waterlines positions shift more landward owing to wave run-up effect. Basically, the run-up characteristics change with the beach slope and offshore wave properties (i.e. offshore wave height, wave period, wave length and etc.). **Figure 3.10**(b) is a schematic illustration of wave run-up. It shows that the results obtained by the mTWM extraction with corrected wave run-up are further shifted landwards compared to survey data. Hence, using corrected wave run-up is essential to determine the shoreline positions accurately for the study site. The following strategy is adopted to correct the wave run-up to obtain more accurate estimates by the mTWM:

Based on both field and laboratory observations, Hunt (1959) initially proposed the following wave run-up formula, which is typically defined by,

$$\frac{R}{H_0} = c\xi_0 + d, \tag{5}$$

where R is the vertical run-up height derived by the offshore wave height H_0, c and d are dimensionless constant, and ξ_0 is the surf similarity parameter.

Several researchers investigated the amount of wave run-up on intermediate to reactive beaches by using video cameras analyses (e.g., Mase, 1989; Ruessink et al., 1998; Ruggiero et al. 2004; Stockdon et al. 2006; Holman and Bowen, 1984). Hasan and Takewaka (2009) first analyzed the wave run-up using data extracted from X-band radar images at Hasaki beach, and proposed a formula to calculate the infragravity wave run-up:

$$\frac{R}{H_0} = 1.025\xi_0 + 0.03, \tag{6}$$

where ξ_0 is the surf similarity parameter (Iribarren and Nogales, 1949) and is expressed by

$$\xi_0 = \frac{tan\beta}{\sqrt{H_0/L_0}}, \tag{7}$$

where $tan\beta$ is the beach slope, L_0 is the deep-water wave length defined as $L_0 = gT^2/2\pi$, g is the gravitational acceleration, and T is the wave period. The low surf similarity parameters ($\xi_0 \leq 0.3$) usually specify a dissipative beach condition while higher values suggest a more reactive condition.

Figure 3.17 shows the variation in wave run-up height along a transect at $x = -49$ m over the period between 12 April 2005 and 31 December 2008 using Eqs. (6) and (7). H_0 and L_0 are calculated from the wave records, and intertial foreshore slope ($tan\beta$) is derived from mTWM estimation considering tidal variation.

The following formula is employed to correct the wave run-up effect on the shoreline position derived by the mTWM:

$$\text{mTWM run-up corrected SP} = \text{mTWM estimated SP} + \left(\frac{\text{Wave run-up height}}{\text{mTWM estimated slope}}\right) \tag{8}$$

where the second term of the right side of Eq. (8) denote the landward horizontal shift due to wave run-up, which is known as wave run-up length. 14 days moving average filter is used for the wave run-up length calculation.

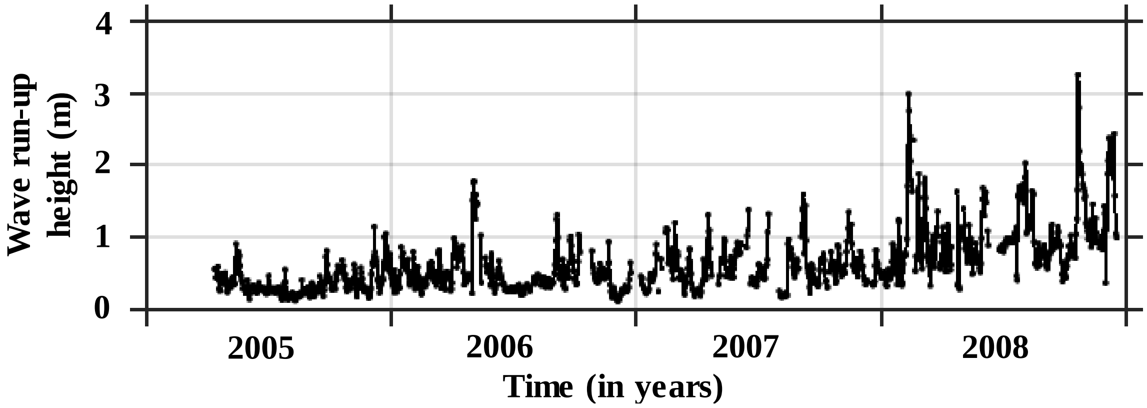

Figure 3.17. Wave run-up height (at *x* = – 49 m) estimated using an empirical wave run-up formula (Hasan and Takewaka, 2009).

The variations in the shoreline position obtained by the mTWM with corrected wave run-up compared to survey data is illustrated in **Figure 3.18**(a). Correspondingly, the vertical elevation bias between the survey and mTWM estimated results with corrected wave run-up is shown in **Figure 3.18**(b), and the MAB is further reduced to 5.9 m (compared to originally obtained value of 14 m), which is theoretically smaller than the spatial resolution of the radar measurements described in Chapter 2. The correlation coefficient between the shoreline position obtained by the mTWM with corrected wave run-up and survey data is 0.85, as shown in **Figure 3.18**(c), which is almost equivalent to previously estimated results. The results show that the utilized method can successfully estimate the shoreline position from radar images after corrected wave run-up.

The mTWM with corrected wave run-up is applied to all alongshore locations to determine the spatio-temporal variation in the shoreline positions for the entire study area over the period between 12 April 2005 and 31 December 2008, as shown in **Figure 3.19**. The color bar of indicates the landwards (blue) and seawards (red) shoreline positions from its origin.

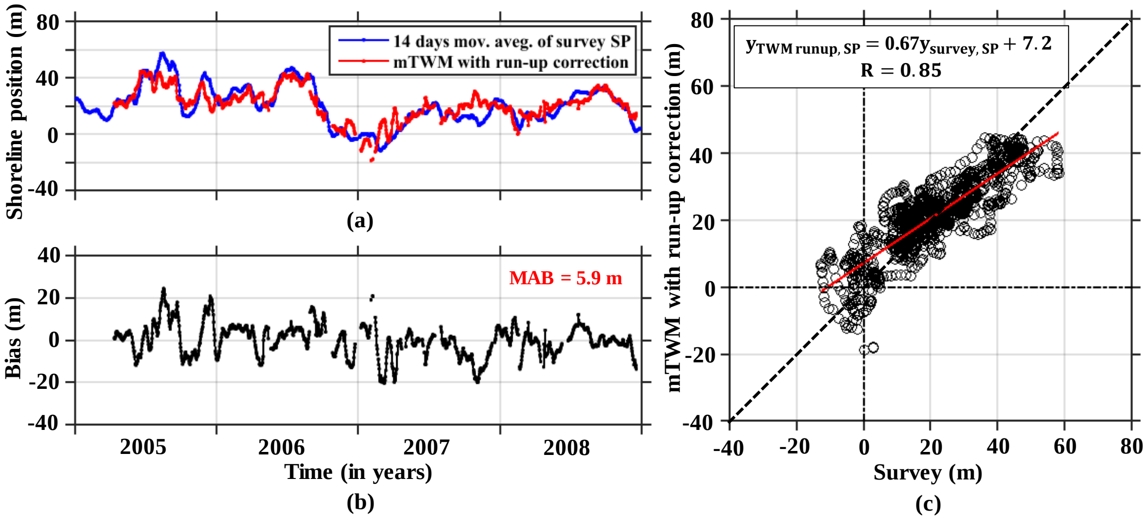

Figure 3.18. (**a**) Temporal variations in shoreline positions (SP) estimated from survey data and mTWM derived results with corrected wave run-up (at $x = -49$ m). (**b**) Estimated bias between survey data and mTWM derived results with corrected wave run-up. (**c**) Scatter plot of survey data vs. mTWM derived results with corrected wave run-up. Red line represents linear fitting line.

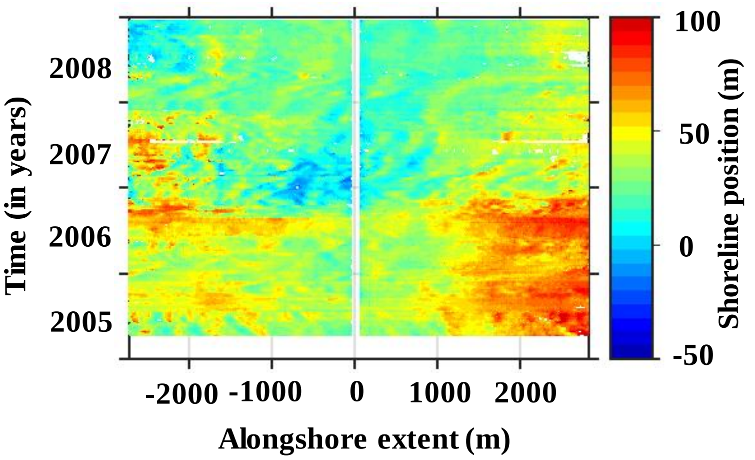

Figure 3.19. Spatial and temporal variations in shoreline positions derived by mTWM with corrected wave run-up during 12 April 2005 – 31 December 2008.

3.2.4 Shoreline position data gaps filled by Garcia's method

The white blanks in **Figure 3.19** indicate the 3% gaps in the shoreline data derived by mTWM owing to the lack of strong waterline signals that caused by over flooding, the existence of strong radar reflectors, etc. Garcia's smoothing and gap filling method (Garcia, 2010) was employed to fill these gaps, and the validity of this method will be checked.

Garcia's method is formulated based on a Penalized Least Squares regression by means of the Discrete Cosine Transform (PLS-DCT), which expresses the data in terms of a sum of cosine functions oscillating at different frequencies, and it is suitable for equally spaced data in one dimension and higher. As the DCT can be multidimensional, the DCT-based PLS regression can be instantly extended to multidimensional datasets. Furthermore, this method was adopted by Wang et al. (2012), and its performances to fill the gaps in a global soil moisture dataset was analyzed. Recently, Bell et al. (2016) and Bird et al. (2017) have employed this algorithm to fill the gaps in beach profile data. This method will be adopted in this study to fill the random gaps in the temporal or spatiotemporal shoreline datasets.

To evaluate the performance of Garcia's method, the numerous random gaps in the mTWM derived shoreline positions with corrected wave run-up are considered. As mentioned before, the estimated variation of shoreline positions with corrected wave run-up are quite similar to the survey data. **Figure 3.20**(a) depicts the temporal variation in gap-filled shoreline positions with corrected wave run-up. The gaps in shoreline positions are filled by Garcia's method. The bias distribution between the survey data and mTWM extracted shoreline position results with corrected wave run-up is shown in **Figure 3.20**(b) with MAB of 5.9 m, which is equivalent to that obtained before applying Garcia's method. As shown in **Figure 3.20**(c), the gap filled result implies that the variations in shoreline positions are synchronized, which is confirmed by the good correlation coefficient (R= 0.85). This value is almost equivalent to that obtained before applying Garcia's method on the wave run-up correction shoreline positions. Therefore, the estimated variation of shoreline positions with corrected wave run-up are quite similar to the survey data. The efficiency of Garcia's filling method will be explained in the discussion section.

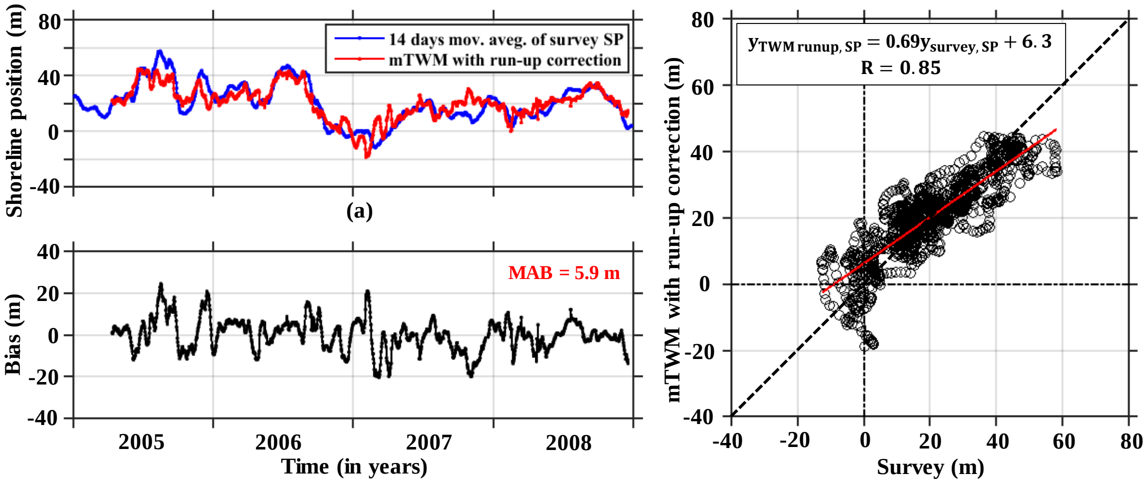

(b) (c)

Figure 3.20. (**a**) Temporal variations in shoreline position (SP) estimated from survey data and mTWM derived results with corrected wave run-up (at x = – 49 m) integrated with Garcia's filling method. (**b**) Estimated bias between survey data and mTWM derived results with corrected wave run-up. (**c**) Scatter plot of survey data vs. mTWM derived results with corrected wave run-up. Red line represents linear fitting line.

Based on the above results, Garcia's method is implemented to fill the gaps in the entire spatiotemporal shoreline position data derived by mTWM with corrected wave run-up (**Figure 3.19**). **Figure 3.21**(a) shows the gap-filled spatiotemporal distribution of wave run-up corrected shoreline positions extracted from time-averaged X-band radar images over four years (2005 – 2008). The rainbow patterns of the color bar indicate the landwards (blue) and seawards (red) positions of shoreline from its origin. Correspondingly, **Figure 3.21**(b) and **Figure 3.21**(c) show temporal variations of significant wave height and spatial mean of shoreline positions, respectively. The adopted gap-filling method demonstrates reasonably well performance in terms of the smoothness of shoreline data. **Figure 3.21** suggests that Garcia's method is capable of filling the numerous random gaps in the shoreline position data. Moreover, we may conclude that Garcia's method combined with mTWM performs reasonably well to fill the random gaps in the shoreline position data, generating results nearly similar to the survey data. The results show seaward shifts of shoreline positions due to low wave conditions, and landward shifts due to high wave conditions. The obtained result is in good agreement with Galal and Takewaka (2015) reported outcome. The obtained features were initially reported by Kuriyama and Lee (2001) and is called beach cycle. Huge erosion was observed in October 2006, which was a result of high waves and storm surge attacking the Kashima Coast. Based on the results obtained by mTWM, we can be assured that the mTWM is a robust approach to detect intertidal shore profiles automatically from time-averaged X-band radar images, and it can be used any beach in the world to help the authorities to understand long- or short-term shoreline changes in coastal zones.

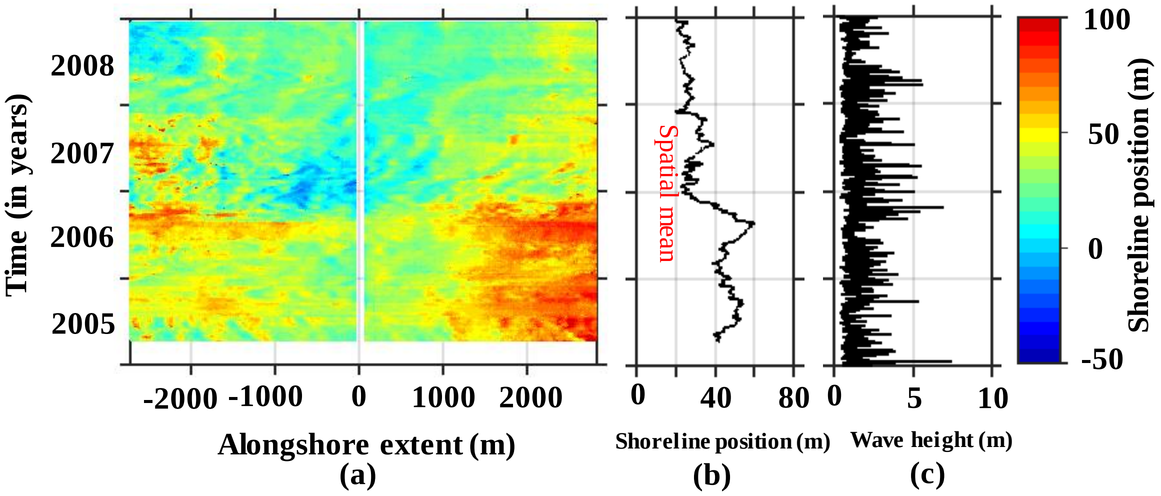

Figure 3.21. (**a**) Gaps in shoreline positions derived by mTWM with corrected wave run-up filled by Garcia's smoothing and gap-filling method. (**b**) Temporal variations of significant wave height. **(c)** Spatial means of shoreline positions.

3.3 Analysis of results and discussion

This section discusses the mTWM extracted results, its adopted correction and possible reasons for the large bias.

3.3.1 Correction of shoreline position derived by mTWM

The purpose of this chapter is to automatically detect the shoreline positions and intertidal foreshore slopes using the mTWM. Automatic extraction of shoreline positions and intertidal foreshore slopes has been successfully performed, but systematic bias in shoreline positions have been observed. As shown in **Figure 3.7**(b), the shoreline position estimated by the mTWM is shifted landwards with MAB of 14 m.

Similar shifts in estimated shoreline positions were reported in previous studies (Takewaka, 2005; Bell et al., 2016). Takewaka (2005) initially analyzed the time-averaged X-band radar images at Hasaki beach, Japan to estimate shoreline positions and intertidal foreshore slopes by manual inspection. In this study, the horizontal shift between the estimated and surveyed shoreline positions was measured as 10 m. Recently, Bell et al. (2016) automatically acquired intertidal shore profile datasets for Hilbre Island at the mouth of Dee Estuary, UK. To validate the accuracy of the calculated results, Bell et al. (2016) compared the TWM generated results with airborne LIDAR surveyed data for the same study site over the radar survey period. The vertical elevation bias between the two intertidal shore profiles is approximately ±0.5 m. This can lead to horizontal shifts in the estimated shoreline positions depending on the beach slopes and wave conditions. If the beach slopes (1:20 – 1:100) vary with high wave conditions, the horizontal shift between the two observations can also vary (10 – 50 m). In both studies, the effects of wave set-up and run-up on reducing the horizontal shift were not considered.

The schematic illustration in **Figure 3.10** suggests that wave set-up and run-up are possibly causing this type of horizontal shifts. Two correction methods were tested to reduce such systematic bias. The correction of wave set-up evaluates a mean waterline above a still water level and allows a horizontal distance between such waterline and tidal level (Chang et al., 2015). **Figure 3.14**(b) shows the distribution of bias between the survey data and shoreline positions derived by mTWM with corrected wave set-up. The MAB dropped by 3.5 m compared to the results obtained before applying wave set-up correction to the shoreline position derived by mTWM (from 14 to 10.5 m); however, horizontal shifts were still present. This may suggest that Eqs. (2) – (4) are appropriately used to reduce some of the detected horizontal shifts in the study site; however, it was not bound in the spatial resolution of radar measurements.

To further reduce the horizontal shifts in the estimated shoreline positions and intertidal beach slopes, a wave run-up empirical formula is applied to achieve an upward shift of waterline position as well as a horizontal shift to landward direction. The bias distribution between survey and shoreline positions with corrected wave run-up is shown in **Figure 3.18**(b), with MAB of 5.9 m, which is smaller than the theoretical resolution of the radar measurements described earlier, and the horizontal shift of bias that obtained by

Takewaka (2005). Considering the use of X-radar images with a theoretical resolution of 7.5 m/pixel, the obtained MAB of 5.9 m is acceptable for automatic application. Sometimes, the bias of estimated shoreline positions is higher than the spatial resolution of the radar measurements. The estimated MAB and correlation coefficient without / with correction of shoreline positions are summarized in **Table 3.1**.

Table 3.1 Summary of estimated MAB and correlation analysis between extracted and survey shoreline positions.

Utilized Method	MAB (m)	Correlation Coefficient (R)
mTWM	14.0	0.86
mTWM with wave set-up correction	10.7	0.85
mTWM with wave run-up correction	5.9	0.85

3.3.2 Reason for the large bias of shoreline positions

Figure 3.22(a) shows the frequency distribution of the estimated bias of shoreline positions. The estimated bias is the difference between survey and mTWM extracted run-up corrected gap-filled shoreline positions for each measurement. The distribution of the bias seems to follow the normal distribution, with a mean value of -0.05 m and variance of 5.9 m. Hence, the overall results indicate that for about 84 % of the bias of the estimated shoreline positions are limited in the spatial resolution of the radar measurement, and rest are slightly higher than spatial resolution. The reason for the significant bias of estimated shoreline positions will be described in **Figure 3.23** – **Figure 3.25**. On the other hand, **Figure 3.22**(b) displays the frequency distribution of the estimated bias between survey and only Garcia’s method gap filled shoreline positions. This estimated bias of shoreline positions is bound in [-10 m,10 m]. That means Garcia’s method interpolates nearly similar shoreline positions like the mTWM derived shoreline positions. As shown in **Figure 3.22**(b), the distribution of the bias seems to follow the normal distribution, with a mean value of -0.1 m and variance of 3 m, where the 32 data are used in this case.

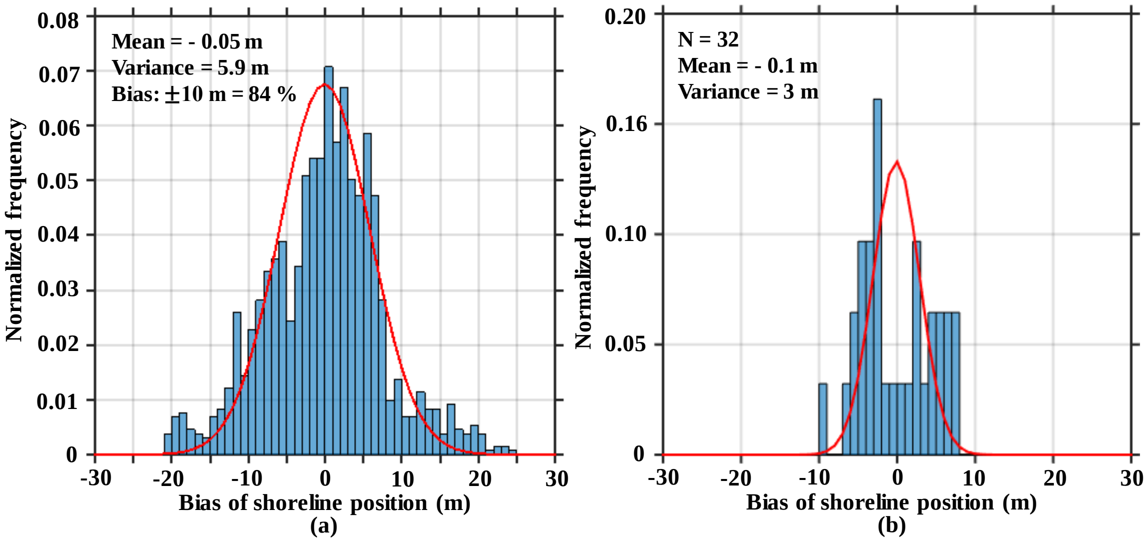

Figure 3.22. (a) Histogram of the bias between survey and mTWM detected shoreline positions during 2005-2008 (1 m bins) with the normal adjusted curve super-imposed in red. **(b)** Histogram of the bias between the estimated shoreline positions with survey and only Garcia's filling method (1 m bins) with the normal adjusted curve super-imposed in red.

Figure 3.23(a) shows the scatter plot between mTWM estimated intertidal slope and the estimated bias of shoreline positions. It seems that bias become large when the mTWM estimated intertidal foreshore slopes are in the milder range (0.01 – 0.06). In such a beach slope condition, the waterline position easily shifted landward and the shoreline position also moved landward. As a result, it sometimes surpasses the survey shoreline position and produces negative shoreline bias. On the contrary, sometimes it falls behind the survey shoreline position for the same beach slope condition and produces a positive shoreline bias. The milder beach slope is not the only reason for this bias, it also depends on wave action. It is noteworthy that the estimated bias is still within acceptable limits for steeper beach slope conditions (0.06 – 0.1). In such conditions, the shoreline position cannot be moved easily in a landward direction without an extreme weather event such as a typhoon. As shown in **Figure 26** (b), these features are verified by the relationship between the frequency distribution of slopes with 0.1 equal intervals and the corresponding estimated MAB of shoreline positions. It is also seen in Figure 26b that the high frequency of milder slope produces the large MAB of shoreline positions. As mentioned before, the action of waves (low and high) might also play an influential role in significant bias. The cumulative frequencies indicate the 75% milder slopes (0.01 – 0.06) can follow the above-mentioned characteristics.

Figure 3.24(a) shows the relationship between 14-days moving averaged wave height and the estimated bias of shoreline positions. It is remarkable to observe that the bias of shoreline positions (positive or negative) become large when the waves are in low or high conditions with same beach slope. These features are confirmed in **Figure 3.24**(b) by the relationship between the frequency distribution of wave height with 0.5 m equal intervals and its corresponding estimated MAB of shoreline positions. It can also be seen that the action of high waves produces the significant MAB of shoreline positions and vice versa. The cumulative frequencies indicate the 90% waves can follow the mentioned characteristics. Overall, the obtained results also show that the intertidal foreshore slopes (steeper or milder) and waves (low or high) are influential parameters for shoreline bias (positive or negative). It is further noted that in some significant bias are also to be expected due to the different cross-sectional transect comparison of radar and survey-derived data.

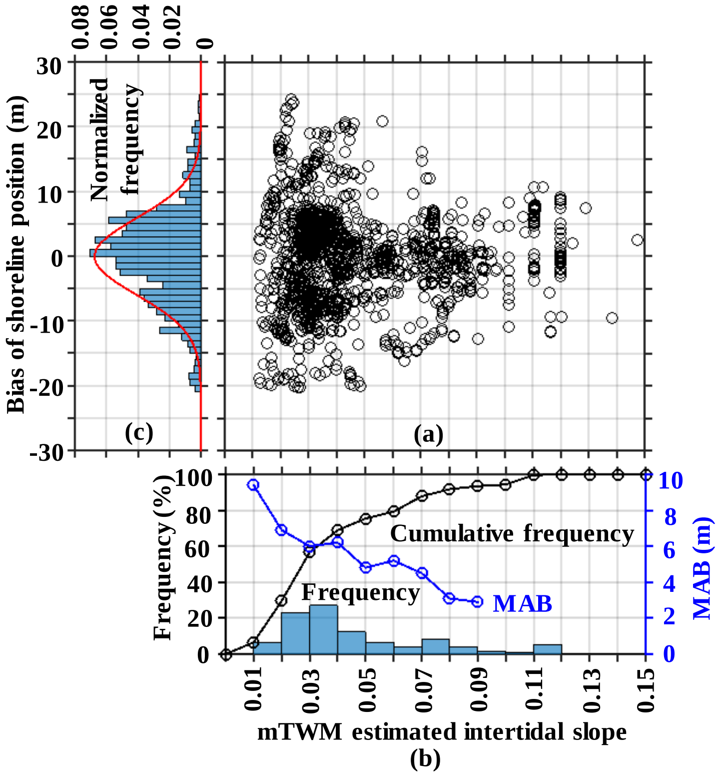

Figure 3.23. (**a**) Relationship between mTWM estimated slope and estimated bias of shoreline positions. (**b**) Frequency distribution of mTWM estimated slopes and corresponding MAB estimation of shoreline positions. (**c**) Frequency distribution of estimated bias of shoreline positions.

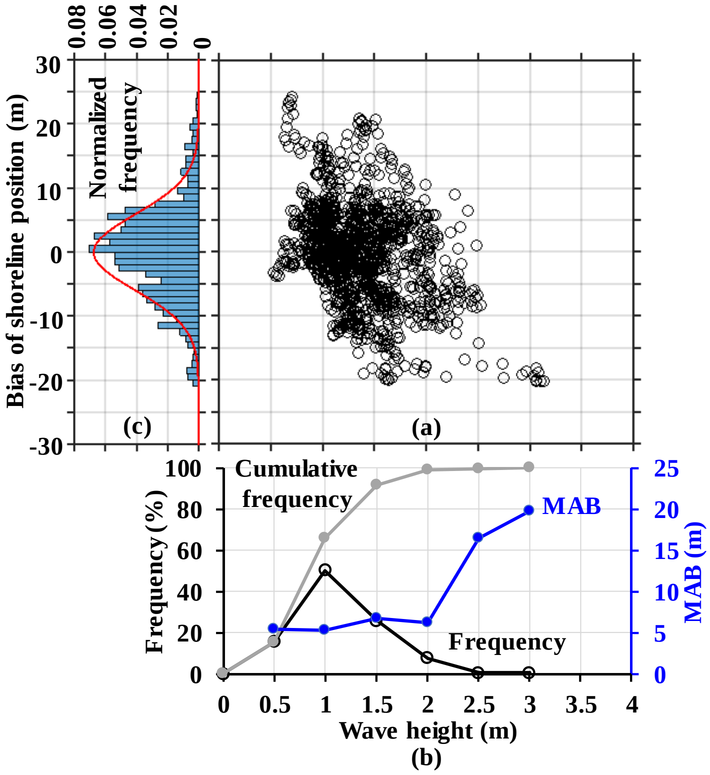

Figure 3.24. (**a**) Relationship between wave height and estimated bias of shoreline positions. (**b**) Frequency distribution of wave height and corresponding MAB estimation of shoreline positions. (**c**) Frequency distribution of estimated bias of shoreline positions.

Figure 3.25(a) shows the temporal variations in bias of shoreline positions and survey shoreline positions. It seems that bias become large when the survey beach profile is abruptly changing to the landwards or seawards direction in quick time, which is due to the influence of waves action (high or low). In such conditions, the mTWM cannot detect properly the actual beach profile from X-band radar images. These tendencies are shown in **Figure 3.25**(b) by the relationship between the rate of change of survey shoreline positions and bias of shoreline positions. This is one of the limitations of mTWM. The linear regression shows a weak correlation coefficient value (R = 0.50) with the large discrepancy of shoreline bias which occurs due to high or low wave conditions. Note that, the correlation coefficient value (positive or negative) depends on the definition of shoreline bias.

Based on the results obtained by the gap-filled corrected wave run-up, we may conclude that more accurate shoreline positions are derived by mTWM with corrected wave run-up, which is very close to the survey data. This confirms that the correction of wave run-up and application of Garcia's method are the most reasonable strategy to reduce horizontal shifts in shoreline positions at Hasaki beach, Japan.

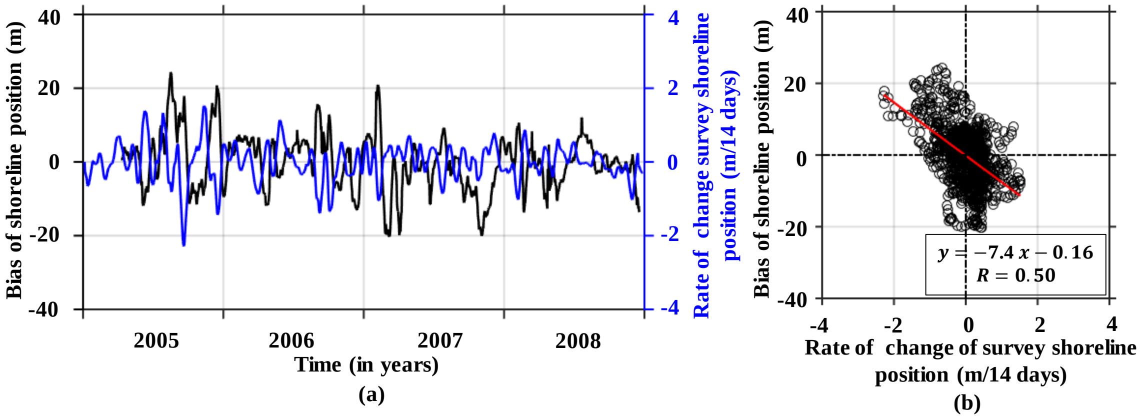

Figure 3.25. (**a**) Temporal variations in bias of shoreline positions and corresponding rate of change survey shoreline positions per 14 days during 2005 – 2008, and (**b**) Relationship between the rate of change of survey shoreline positions and bias of shoreline positions**.**

CHAPTER FOUR : DATA FUSION FOR X-BAND RADARS AND SAR OBSERVATIONS

4.1 Introduction

Understanding and monitoring of shorelines are significantly important for proper beach management. There are several shorelines monitoring tools such as situ beach profiling, LIDAR surveys, aerial photography, aerial laser surveys, video camera analysis, satellite imagery, Synthetic Aperture Radar (SAR), land-based X-band radar and so on (Yousef et al. 2013). There have been many attempts to detect shoreline position from the individual observations. However, a large number of high resolution spatial and temporal coverage data are essential for monitoring the intertidal morphological change and seasonal variations of shorelines. Among the above-mentioned remote sensing imagery, there have some advantages and disadvantages for each of beach monitoring tools. Likewise, aerial and satellite imaging typically have broad spatial coverage, but their temporal coverage is limited. On the other hand, X-band radar can provide frequent data in time. However, it has some shortcomings, e.g., limited spatial coverage compared to aerial and satellite imaging, and cost of data processing to digitize shoreline position from the images. As previously mentioned, the southern Kashima Coast is approximately 16 km long straight sandy coast with Hasaki Fishery Port at the south end and Kashima Port at the end of the north (**Figure 4.1**). It is clearly seen from **Figure 4.1** that three spatial gaps have been fixed along the coast where no X-band radar data is available. To cover the whole coast, afterwards SAR data is introduced which covers the whole spatial domain.

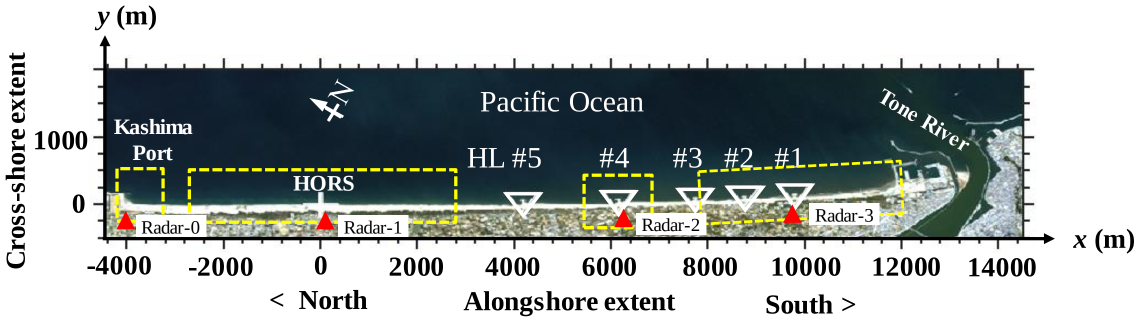

Figure 4.1. Kashima Coast, Japan. The red triangle indicates the radar location. Headlands (HL, 1-5). The rectangular boxes with yellow lines indicate the effective coverage of Radar-0, 1, 2 and 3 observations and white triangles indicate the location of artificial headlands.

In this context, a data fusion technique is tested here to overcome these types of shortcomings. Data fusion, which integrates multiple datasets from different sources and produces a unified output that preserves the desired information (Wang et al., 2015). The benefits of data fusion usually increased spatial coverage or measuring range and information completeness.

Similar types of work have been done by Kumar and Takewaka (2018) with the aid of Garcia's gap filling method (Garcia, 2010). On that study, Kumar and Takewaka (2018) utilized the TWM (Bell et al., 2016) for extracting shoreline positions from X-band radar images. The results of the gap filling method and the TWM were not fully reasonable acceptance, compared to aerial laser survey data. In this study, the mTWM is employed to digitize the shoreline positions from X-band radars and Data INterpolating Empirical Orthogonal Functions (DINEOF) method is applied for data fusion between X-band radars and SAR satellite observations to find new outcomes that will more acceptable limit. Deronde et al. (2009) used a combination of airborne LIDAR and airborne hyperspectral data to study the beach morphodynamics of the Belgian backshore and foreshore. These authors explain that the combined interpretation of the erosion/sedimentation map with the classified hyperspectral data yields an appropriate method for studying the process of sand transport along the coastline.

In this study, two types of data from extracted by different methods are used: land-based X-band radar (Takewaka, 2005) and SAR satellite observation (Takewaka et al., 2018). Hourly time-averaged X-band radar images are collected from Dec 1, 2009 to May 15, 2012 with some temporal and spatial gaps, and six SAR satellite observation data within the time duration (Dec 1, 2009 to May 15, 2012). The SAR satellite observation data are captured in 2010 (Jan 30, May 2, Aug 2, Nov 20) and 2011 (Feb 2, April 7). The processed SAR shoreline data is supplied by Takewaka et al. (2018) which is shown in **Figure 4.2**.

The main purpose of this chapter is to propose a data fusion technique that integrates two types of shoreline data observed by land-based X-band radars and SAR satellite. Above mentioned two types of data are integrated by DINEOF method, and the performance of proposed method is to validate with aerial laser survey data.

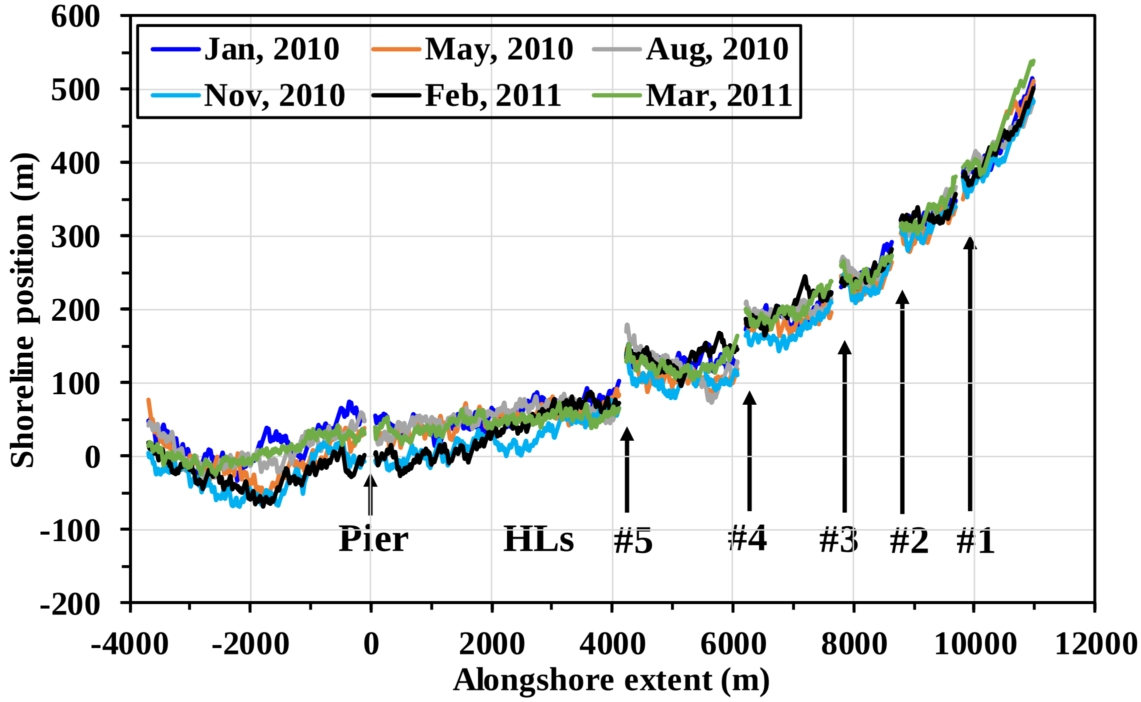

Figure 4.2. Shoreline position in the southern part of Kashima coast extracted from the captured SAR image during 2010 – 2011.

4.2 Application of mTWM for X-band radars observations

As previously mentioned in **Figure 4.1**, four land-based X-band radars have been installed, namely Radar-0, Radar-1, Radar-2, and Radar-3 for the observation of shorelines variation. **Figure 4.3** shows the example of hourly time averaged X-band radar images captured by Radar-0, Radar-1, Radar-2, and Radar-3, respectively. The pixel size of Radar-0, Radar-1, and Radar-2 is approximately 5.42 m, and Radar-3 is about 7.18 m, whereas the theoretical spatial resolution of Radar-0, Radar-1, Radar-2 is approximately 7.5 m and Radar-3 is approximately 10 m. Each radar can cover 5 km spatial range separately. But the effective range is few due to radar capability. The shaded areas in the panels represent the effective spatial coverage of each radar's observations (**Figure 4.3**).

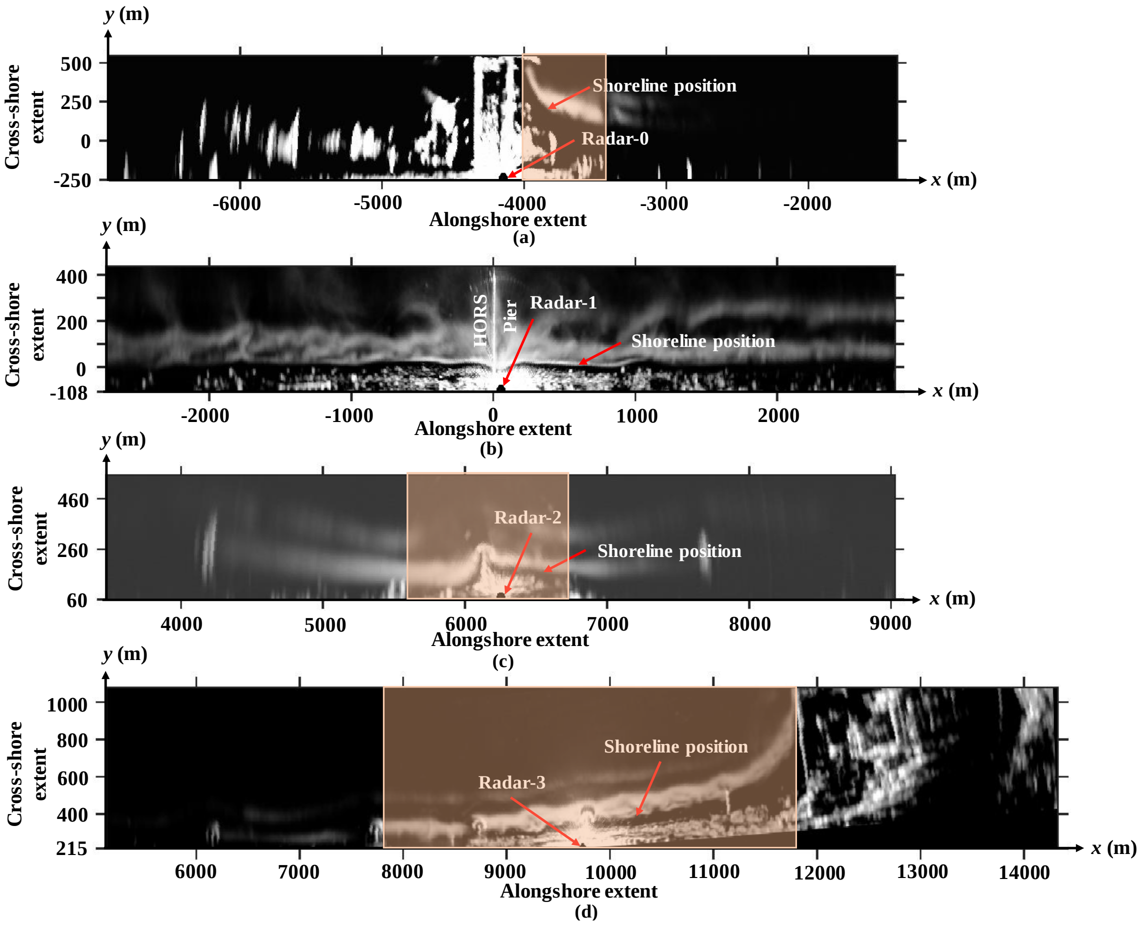

Figure 4.3. Example of time-averaged X-band radar images captured by (**a**) Radar-0, (**b**) Radar-1, (**c**) Radar-2, and (**d**) Radar-3 (4.5◦ anti-clock wise rotation), respectively. The shaded area indicates effective spatial coverage of radar observations.

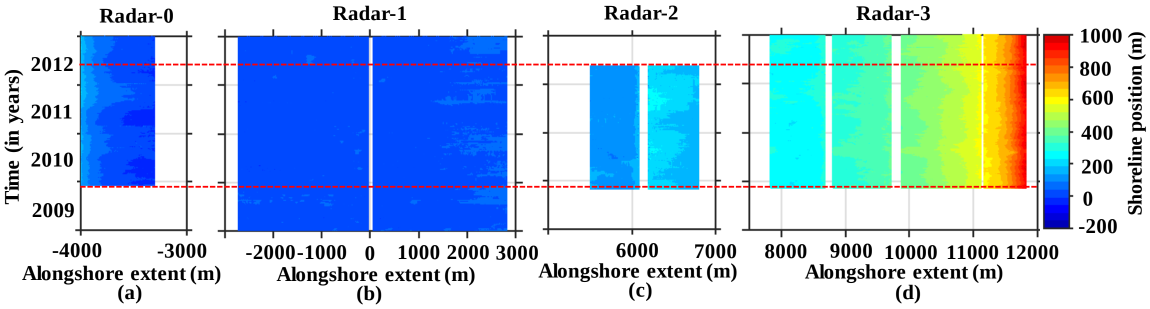

Figure 4.4. Wave run-up corrected shoreline positions extracted by the mTWM from four land-based X-band radars (**a**) Radar-0, (**b**) Radar-1, (**c**) Radar-2, and (**d**) Radar-3 observed hourly time averaged images. Red lines represent the common period of four radars observation between the time history of 2009 and 2012.

Modified Temporal Waterline Method (mTWM) is employed to digitize the shoreline positions from hourly time-averaged X-band radar images. The details of the mTWM digitization procedure of shoreline positions and intertidal foreshore slopes from X-and radars image and its validation are explained in the previous chapter. The mTWM extracted shoreline positions from X-band radar images with wave run-up correction have been displayed in **Figure 4.4**. The effective spatial coverage of shoreline position of Radar-0 is -4000 < x < -3300 m, Radar-1 is -2724 < x < 2826m, Radar-2 is 5540 < x < 6812 m, and Radar-3 is 7800 < x < 11800 m. It is also seen from **Figure 4.4** that two types of gaps were observed: (i) fixed spatial gaps (-49 < x < 65 m; 6081 < x < 6194 m; 7640 < x < 7824 m; 8685 < x < 8800 m; 9708 < x < 9866 m; 11119 < x < 11162 m) which are due to saturation of the radar measurement, and limited coverage of radars, and (ii) random gaps which are due to the lack of strong waterline signals of radar images. The x-axis corresponds to the longshore extent, and the y-axis corresponds the time history between 2009 to 2012. The color bar represents the shoreline position variation. The red lines in **Figure 4.4** indicate the common period of four radars observation between the time history of 2009 and 2012.

4.3 Combination of Radars and SAR observation shoreline positions

Since the radars do not cover the whole 16 km coast (see **Figure 4.1**), we further try to combine six SAR observation shoreline data with radars observation. The combination of the mTWM extracted shoreline positions from four radars in date 2009 to 2012 with SAR satellite observation shoreline positions in the year of 2010 (Jan 30, May 2, Aug 2, Nov 20) and 2011 (Feb 2, April 7) is shown in **Figure 4.5**. The shaded region in **Figure 4.5** shows the SAR observation shoreline positions.

Within the SAR spatial coverage, there are fixed gaps (4120 < x < 4240 m) due to the existences of Headlands. It is remarkable to observe that after introduced SAR shoreline position, the combined data covers the whole spatial extent; however, the temporal update of SAR data is available only six times during 2009 – 2012. For the data fusion, the DINEOF method is selected that can significantly filled the X-band radars and SAR satellite observations gappy shoreline positions. The details of DINEOF method will be described in section 4.4.

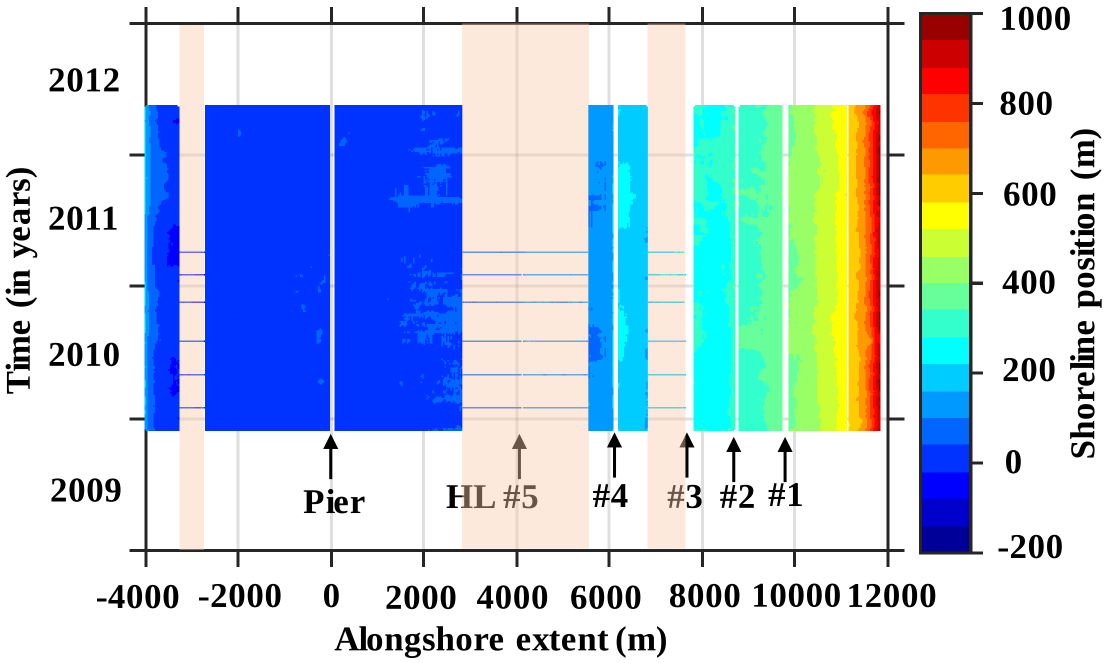

Figure 4.5. Combined X-band radars and SAR satellite observation shoreline positions (2009 – 2012). The shaded region indicates the SAR introduced shoreline positions.

4.4 Algorithm of DINEOF method

Different studies have been conducted about the imputation of missing values (Lakshminarayan et al., 1999), however, none of them were comprehensive enough to give an overall view of the appropriate method for randomly and continuously gappy datasets. In this study, the Data INterpolating Empirical Orthogonal Function (DINEOF) is selected to impute artificially created missing information of shoreline datasets, and combined radars and SAR observation shoreline datasets. As we know, image is an integral part of the field of machine learning and it is also used for machine learning research. The obtained shoreline position data is produced from sequences of radars and SAR satellite images. Therefore, the DINEOF is better tools to fill the gappy position for machine learning datasets like sea surface temperature.

DINEOF is an EOF-based iterative method which was developed by Beckers and Rixen (2003) to reconstruct the missing data from oceanographic datasets. Later on, several researchers (Alvera-Azcárate et al., 2005, 2015, 2016; Beckers et al., 2006; Nechad et al., 2011; Nikolaidis et al., 2013, 2014; Sirjacobs et al., 2011; Taylor et al., 2013; Zhou et al., 2017; Liu and Wang, 2019) have been applied this method on different types of data sets such as sea surface temperature (SST), Soil Moisture and Ocean Salinity (SMOS) sea surface salinity, historical surface chlorophyll-a concentration, MODIS land surface temperature data, and etc. The workflow of DINEOF method is as follows:

(i) During the DINEOF process, the original dataset is stored in the initial matrix with $m \times n$ dimensions, where m is the number of grids in the spatial domain and n is the number of time steps in the time series; this matrix contains both existing and missing data. Prior to DINEOF, the mean of the input dataset is removed, missing values are set to zero, and an independent cross-validation dataset (3% of the existing data in the matrix were randomly selected and removed from the input dataset).

(ii) For reconstruction of the missing data, the EOF decomposition is computed by the singular value decomposition (SVD) method, and the spatial EOFs (U), singular values matrix (S) and temporal EOFs (V) are obtained. The missing data can be reconstructed by the truncated EOFs:

$$X_{i,j} = \sum_{p=1}^{N} S_p \left(U_p\right)_i \left(V_p^T\right), \tag{9}$$

where $X_{i,j}$ are the missing data; i, j are the spatial and temporal indices of the missing data; U_p and V_p are the pth column of the spatial and temporal EOFs, respectively; S_p is the pth singular value; and N is the number of EOFs mode used for reconstruction.

(iii) The first EOF mode ($N = 1$) is then calculated from Eq. (9) through the SVD technique, and the missing values are replaced with the initial guess by the data reconstruction using the spatial and temporal functions of only the first EOF mode. The first EOF mode is then recalculated iteratively using the previous best guess as the initial value of the missing data for the subsequent iteration until the process converges is reached, when the root mean square error (RMSE) at the cross-validation points is stabilized.

(iv) The number of EOFs increases one by one and for each EOF mode ($N = 2, 3$ ... N_{max}), the whole reconstruction procedure (iii) is operated again until convergence. The optimal number of EOFs (N_{max}) is retained when the minimum RMSE is obtained.

(v) Once the optimal number of EOFs is determined, the entire process is restarted including the 3% cross-validation data that we set aside before. Finally, the reconstruction procedure is performed again, based on the optimal EOF modes, until convergence is reached. The process to determine the optimum number of EOF modes in the final reconstruction is fully automatic. For example, if the RMSE of the validation data decreases gradually from mode 1 to mode 15, but the RMSE starts to increase gradually from mode 16 to mode 20, then the first 15 modes are considered as optimum. The working approach of DINEOF method is shown in **Figure 4.6**.

A R package "sinkr" is applied to fill the missing values for gappy shoreline data sets. The package is available in URL: https://github.com/marchtaylor/sinkr.

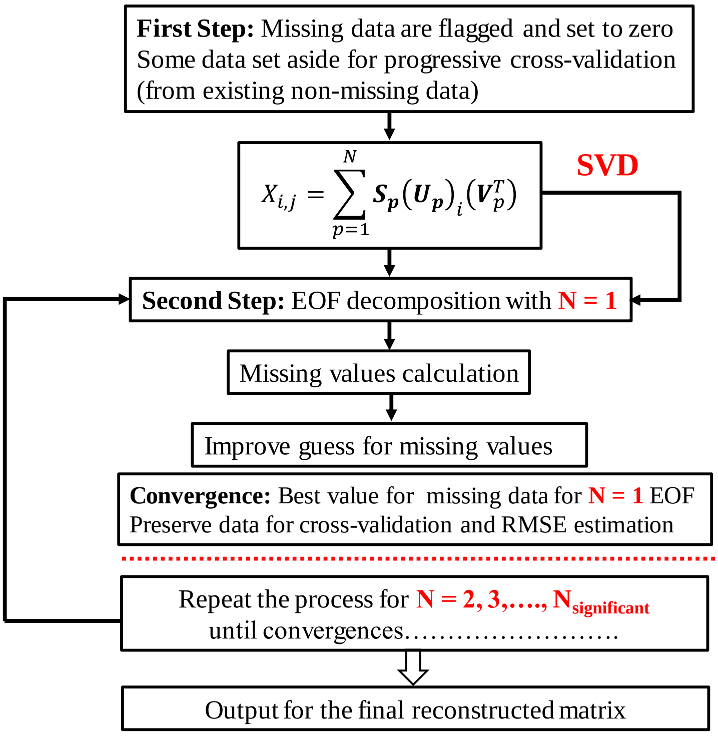

Figure 4.6. The workflow of DINEOF method (after Nikolaidis et al., 2014).

4.5 Artificially created data gaps filling and fusion results

4.5.1 Validation of DINEOF method for the artificial spatiotemporal data gaps

Prior to applying the DINEOF method in combined X-band radars and SAR observation shoreline position data (see **Figure 4.5**), the performance of the DINEOF is checked by artificially created spatiotemporal data gaps in Radar-1 shorelines data. In order to validate the performance skill of the DINEOF method, a 1020 m long ($-2723 < x < -1703$ m) and a 527 m long ($2300 < x < 2827$ m) artificial spatiotemporal gaps of Radar-1 shoreline data is introduced (see **Figure 4.7**(b)), whereas the original shoreline datasets is shown in **Figure 4.7**(a). The output of DINEOF method gap filled shoreline position is shown in **Figure 4.7**(c). Compared with **Figure 4.7**(a), the outcome looks reasonable from the observation of eye visualization as shown in **Figure 4.7**(c).

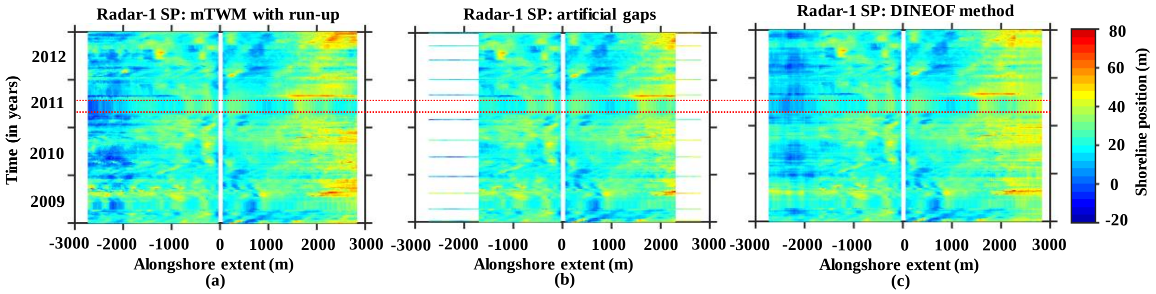

Figure 4.7. (**a**) mTWM extracted Radar-1 shoreline position data, (**b**) artificial temporal gaps set in shoreline positions, and (**c**) reconstructed shoreline positions by using DINEOF method. Red lines indicate the missing (20 April 2011 to 26 July 2011) of X-band radar data due to mechanical troubles.

In the range of (-2723 < x < -1703 m), the temporal variations of the original and reconstructed shoreline positions at x = -2702 m, x = -2360 m, and x = -1801 m is shown in **Figure 4.8**(a), (b) and (c), respectively. In the respective alongshore location, the correlation coefficient between the original values and their corresponding predictions are approximately 0.53, 0.69, and 0.70. The MAB between original and reconstructed results in the respective location are 6.8 m, 4.9 m, and 4.2 m. A good correlation and low MAB are found when the filled data are close to original data in the case of temporal variation of shoreline dataset. A similar tendency is also found in the range of (2300 < x < 2827 m). The correlation coefficient and MAB is displayed in **Figure 4.9** (a), (b) and (c) at x = 2349 m, x = 2501 m, and x = 2750 m, respectively. **Figure 4.10** (a), (b) and (c) demonstrate the spatial variation of the original and reconstructed shoreline positions. The correlation coefficient (CC) between original and reconstructed shoreline positions are 0.97, 0.75, and 0.99 on the date of Jan 1, 2010, Jan 1, 2011, and Jan 1, 2012, respectively. Overall, **Figure 4.11** shows the distribution of correlation coefficient and MAB between original and DINEOF reconstructed shoreline positions for each of longshore extent (-2726 < x < 2824 m). The above results suggest that the DINEOF method has a good prediction skill for filling in data gaps of spatiotemporal shoreline dataset.

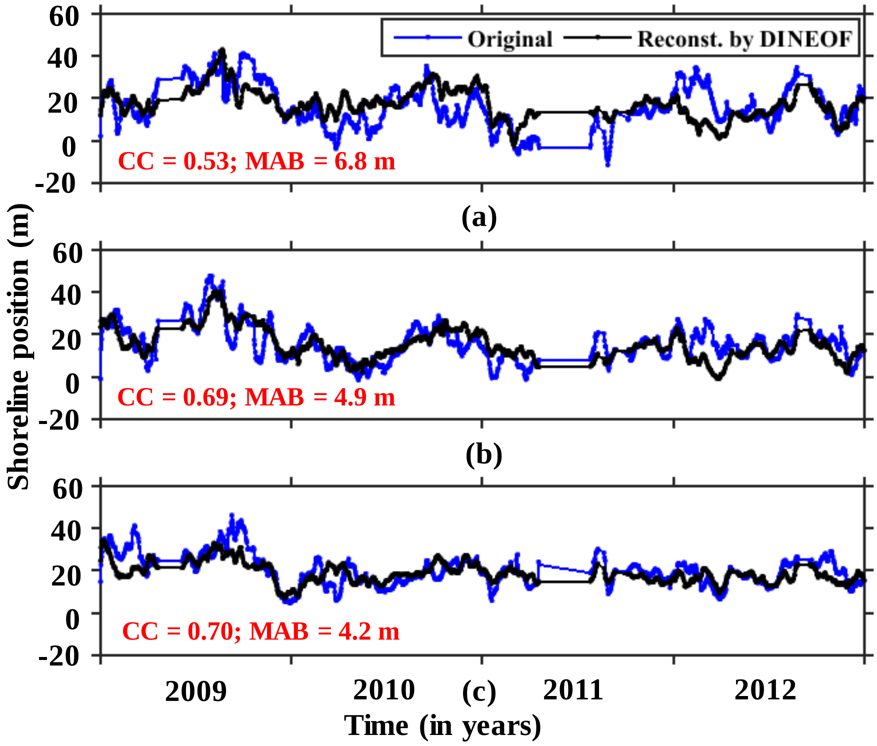

Figure 4.8. Verification of the performance of DINEOF method: Temporal variations of shoreline positions between original and reconstructed data at (**a**) *x* = -2702 m, (**b**) *x* = -2360 m, and (**c**) *x* = -1801 m.

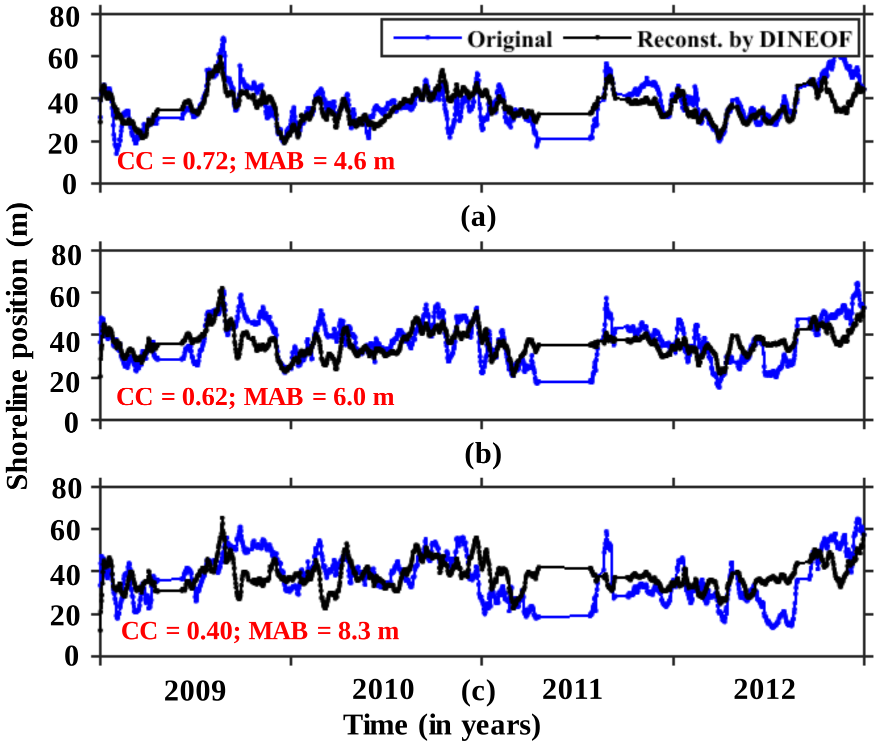

Figure 4.9. Verification of the performance of DINEOF method: Temporal variations of shoreline positions between original and reconstructed data at (**a**) *x* = 2349 m, (**b**) *x* = 2501 m, and (**c**) *x* = 2750 m.

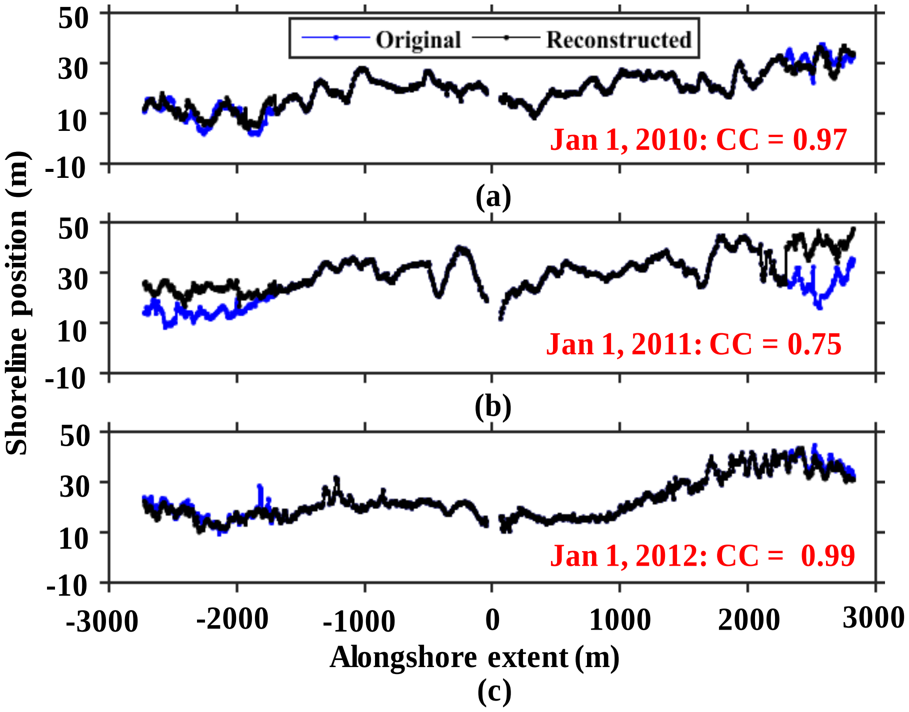

Figure 4.10. Verification of the performance of DINEOF method: Spatial distributions of shoreline positions between original and reconstructed data (**a**) Jan 1, 2010, (**b**) Jan 1, 2011, and (**c**) Jan 1, 2012.

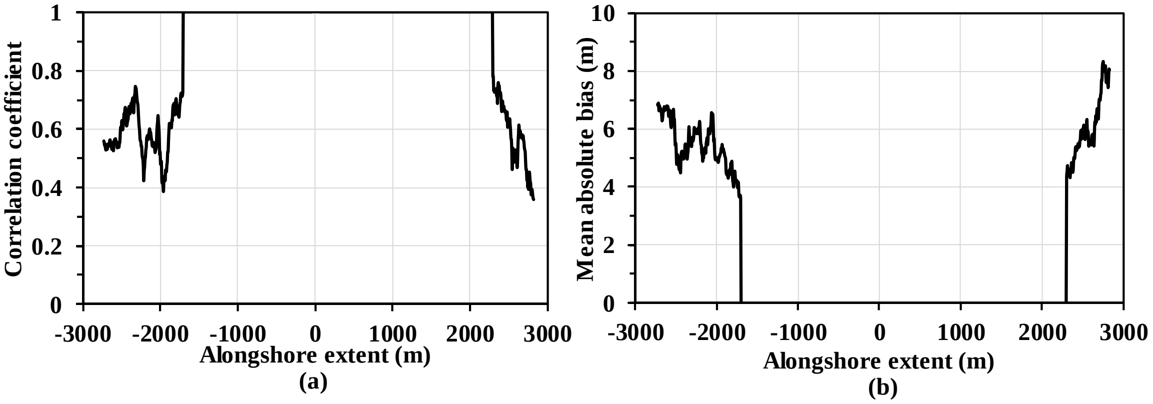

Figure 4.11. (**a**) Distribution of correlation coefficient, and (**b**) Mean Absolute Bias (MAB) between original and DINEOF reconstructed shoreline positions for each of longshore extent (-2726 < *x* < 2824 m).

4.5.2 Data fusion by DINEOF method and its validation

The following section emphasizing the role of DINEOF reconstruction method to fill the combined Radars and SAR satellite observation shoreline positions at Kashima coast, Japan.

Since the radars do not cover the whole 16 km coast, we further try to combine six SAR observation shoreline data with radar observation (see **Figure 4.5**). As mentioned before, the processed SAR shoreline data is supplied by Takewaka et al. (2018) and within the SAR spatial coverage, there are fixed gaps ($4120 < x < 4240$ m) due to the existences of Headlands. As shown in **Figure 4.5**, a region ($-4000 < x < 7640$ m) is set to test the applicability of the DINEOF reconstruction method for combined shoreline positions extracted from SAR and radar observations. DINEOF method is applied to fill the numerous data gaps at this region and the result is shown in **Figure 4.12**(a). The rainbow patterns of color bar indicate the variation of shoreline position from its origin. The shaded portion indicates the reconstructed shoreline position variations. Correspondingly, **Figure 4.12**(b) and **Figure 4.12**(c) show the temporal variation of the spatial mean of shoreline positions and significant wave height, respectively. The results also show seaward moves of shoreline positions due to low wave conditions, and landward moves due to high wave conditions. The obtained result is consistent with previous chapter reported outcome. **Figure 4.12**(d) is the mean, maximum and minimum of filled shoreline positions, and **Figure 4.12**(e) depicts their standard deviation. Small value of standard deviations and narrow ranges identify stable regions, while large standard deviations and wide envelopes are associated with regions of high variability. It is remarkable to observe that the standard deviation of reconstructed shoreline position is relatively more stable than radars obtained result. Therefore, the temporal variations of DINEOF fusion shoreline positions at $x = 3300$ m, $x = 4400$ m, and $x = 7300$ m is shown in **Figure 4.13**. The tendency of these variations is consistent with radars extracted shoreline positions. Hence, from the above analysis, it may conclude that data fusion method works well to process shoreline datasets. However, it may need to further investigate the performance of DINEOF method and its obtained outcome by aerial laser survey shoreline dataset.

The obtained result of data fusion is verified with aerial laser survey data, which is taken in date 2011 May. **Figure 4.14**(a) shows the comparison between the data fusion and aerial laser survey shoreline positions result and **Figure 4.14**(b) represents the point to point difference between these two estimations. The MAB estimation of shoreline position for the whole longshore extent is about 11.7 m, which is almost close to theoretical spatial resolution of Radar-3 and SAR satellite observation images. Sometimes, the calculated bias is larger than overall longshore extent MAB. The explanation of large discrepancies will be described in next sub-section.

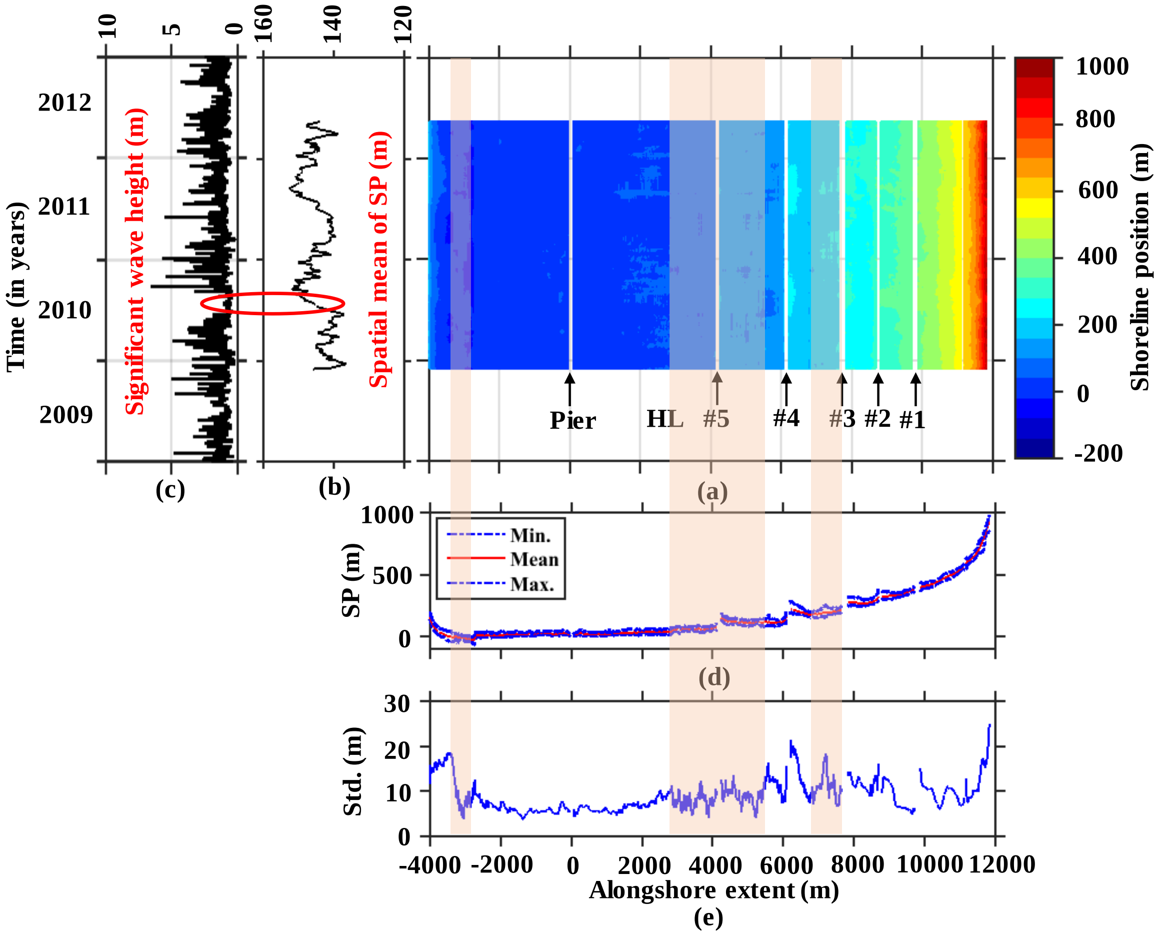

Figure 4.12. (**a**) The final result of the shoreline variations processed by DINEOF method over the period of Dec 1, 2009 to May 15, 2012, (**b**) temporal variations of spatial mean of shoreline positions, and (**c**) its corresponding significant wave height. (**d**) Mean, minimum and maximum range of the shoreline position variation of fusion data, and (**e**) their standard deviation of the variation. The shaded portion indicates the data fusion results.

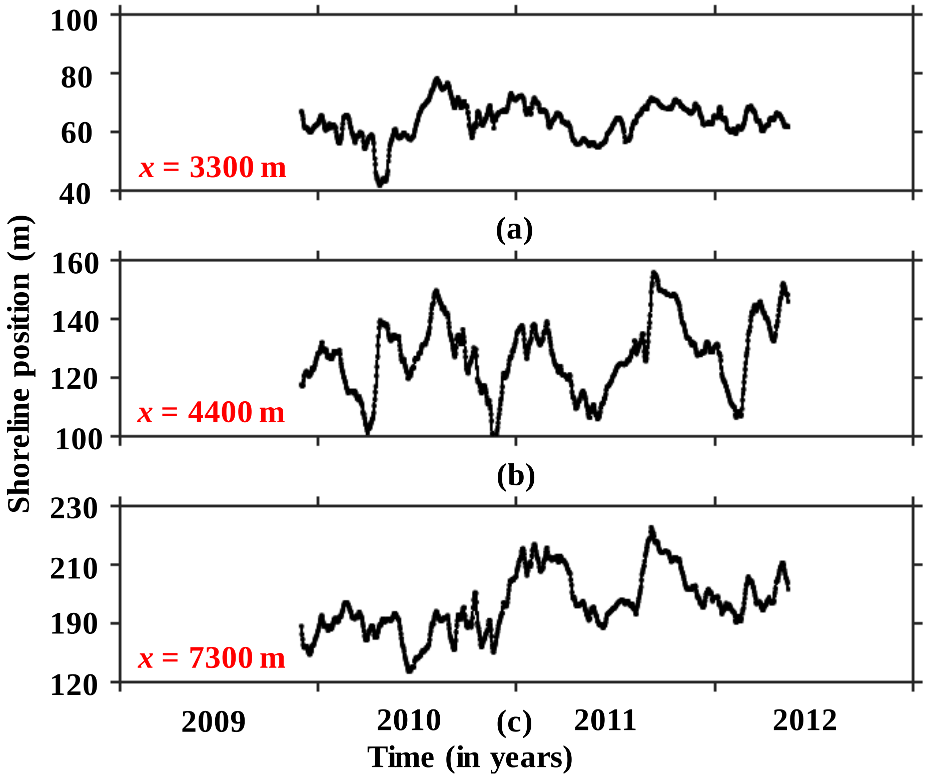

Figure 4.13. Temporal variations of data fusion shoreline positions at (**a**) *x* = 3300 m, (**b**) *x* = 4400 m, and (**c**) *x* = 7300 m, respectively.

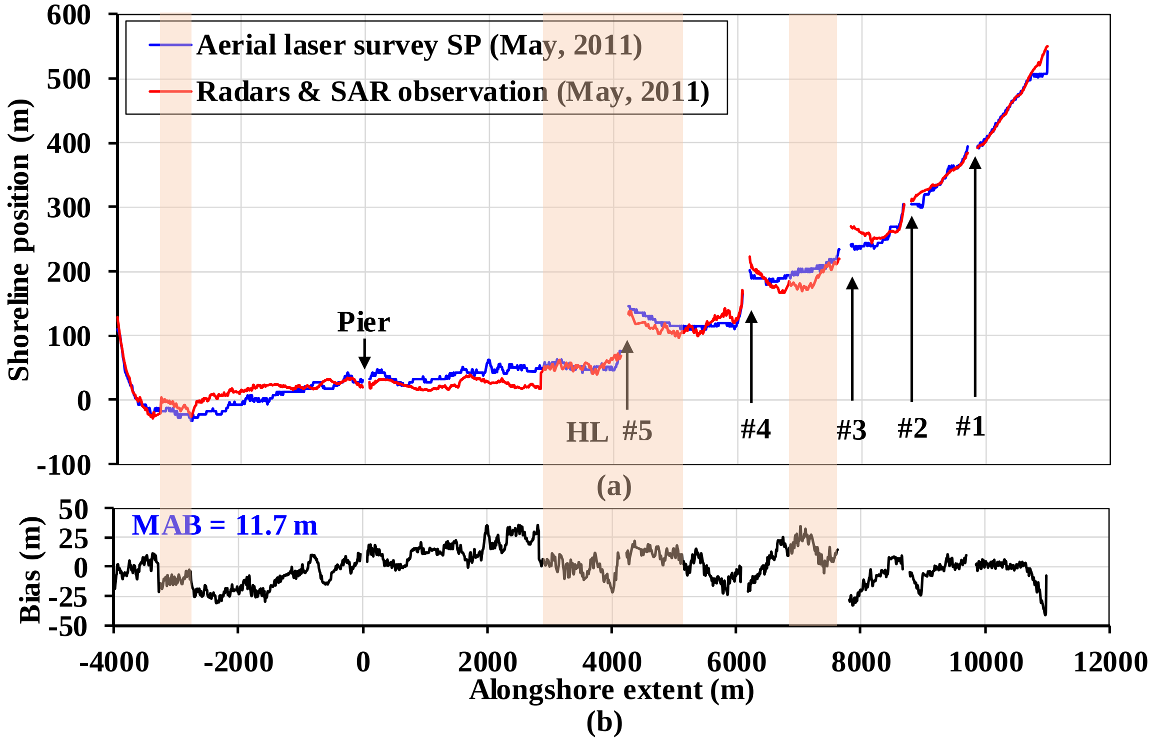

Figure 4.14. (**a**) Validation of the estimated shoreline positions from Radar and SAR observation with survey (2011 May) result, and (**b**) its corresponding bias.

4.5.3 Reason for the large bias of shoreline positions

Table 4.1 Comparison of shoreline MAB from different sources.

Longshore extent range (m)	MAB (m)	Outcome obtained from
-4000 m < x < -3300 m	5.0	Radar-0
-3290 m < x < -2730 m	11.3	Data fusion
-2724 m < x < 2826 m	14.5	Radar-1
2830 m < x < 5530 m	8.3	Data fusion
5540 m < x < 6812 m	10.3	Radar-2
6820 m < x < 7640 m	15.9	Data fusion
7820 m < x < 11000 m	8.2	Radar-3

Table 4.1 shows the individual radars and data fusion coverage range wise mean absolute bias (MAB) values. However, it is seen from **Table 4.1** that the obtained MAB greater than 10 m for Radar-1 spatial coverage range (-2724 m < x < 2826 m) and introduced SAR coverage range (6820 m < x < 7640 m). As mentioned previously, Radar-1 data was not available in time (20 April 2011 to 26 July 2011) due to mechanical troubles. Due to unavailability of radar images and extrapolation outcomes are the possible reasons for the large bias of Radar-1 shoreline positions. For 6820 m < x < 7640 m, the obtained MAB is also larger than 10 m because the SAR introduced data is continuously landwards direction compared to aerial laser survey data. This is a possible reason for the large bias of the respective longshore extent, which was discussed in Takewaka et al. (2018) study. On the other hand, the individual bias around the headlands #3 and #4 seems significantly large. The radar obtained shoreline position is corrected with wave run-up effect, and aerial laser survey obtained shoreline position is corrected with tidal effect, which is completely two different corrections. In the previous chapter, it is justified that shoreline position moves approximately 8 m in landwards direction on average due to wave run-up effect. The estimated bias becomes large due to different correction of radars and aerial laser survey shoreline positions. It may be one possible reason for this large bias. The low quality of

radar images taken from Radar-2 and Radar-3 may be another possible reason for this large bias.

Figure 4.15 shows the frequency distribution of the estimated bias of shoreline positions. The distribution of the bias seems to follow the normal distribution with a mean value of 1 m, and variance of 11.2 m. Hence, the overall results indicate that for about 74 % of the bias of the estimated shoreline positions are bounded in ±16 m, which is 1.5 times of the spatial resolution of Radar-3 and SAR satellite measurement, and rest of the bias are slightly larger than spatial resolutions. The reason for the large bias is described above.

Based on the MAB estimation, we may conclude that our fusion method performs reasonably well to process overall shoreline dataset; however, in some regions the bias becomes large.

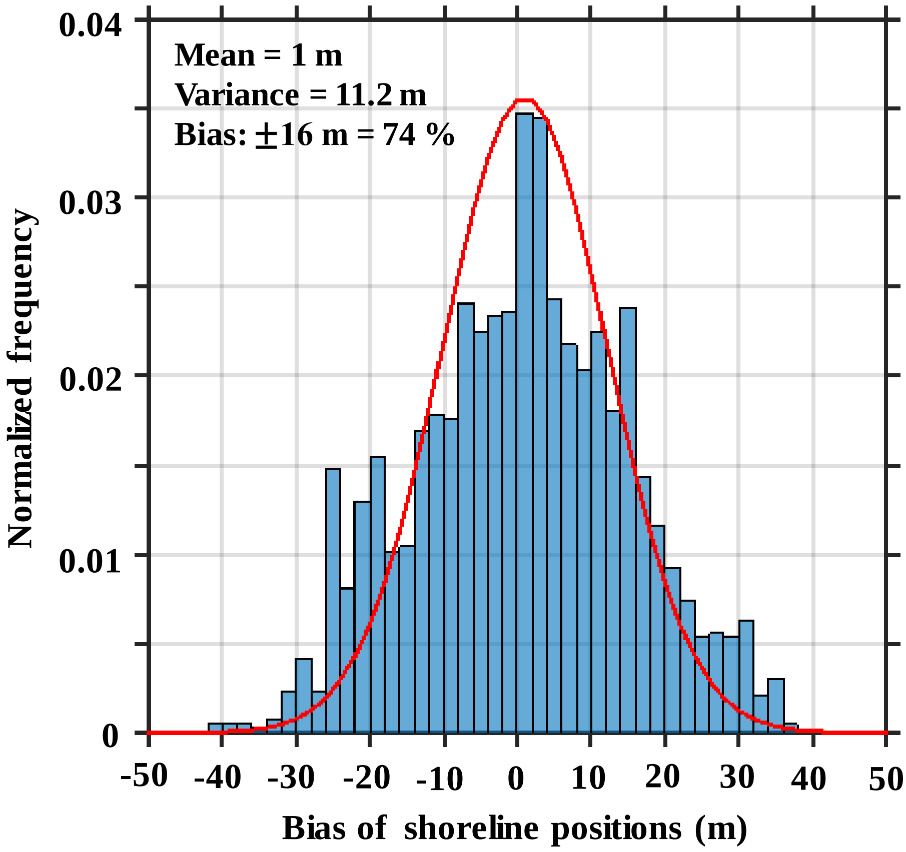

Figure 4.15. Histogram of the bias between aerial laser survey and DINEOF fusion shoreline positions (2 m bins) with the normal adjusted curve super-imposed in red.

CHAPTER FIVE : CONCLUSIONS

This study tried to estimate the shoreline positions and intertidal foreshore slopes from four land-based radars captured time averaged X-band images using mTWM along a 16 km straight micro-tidal sandy Kashima coast, Japan. Since the installed radars do not cover whole spatial extent of the coast. Then, the SAR observation shoreline positions are introduced, where radars data were not available. Hereafter, a data fusion technique is proposed and applied for covering whole domain of the coast, which remove the limitations of both observations. This chapter describes summary of the study, and also presents the limitations of the study and suggests some recommendation for future works.

5.1 Summary of the study

5.1.1 Shoreline positions and intertidal slopes detection

The mTWM is presented as a way to detect shoreline positions and intertidal foreshore slopes from X-band radar images. The method is slightly modified from the Bell et al. (2016) approach (TWM). Cross-shore direction-wise bottom elevation estimation was considered as the TWM. Due to the presence of low signal similarities between pixel intensities and tidal binary signals at the landward cross-shore location, the TWM failed to estimate an accurate intertidal shore profile. Hence, determining water level direction-wise bottom elevation and detecting intertidal shoreline profile are considered as the mTWM. The mTWM is successfully employed to detect accurate shoreline positions and intertidal foreshore slopes from X-band radar images collected over the course of two-week tidal cycle variation at microtidal sandy Hasaki beach, Japan, during 2005–2008. Compared to survey data, the MAB of the detected shoreline positions was 14 m. However, the estimated foreshore slopes were almost close to survey data. Sometimes, the surveyed slope looks steeper than that estimated by the mTWM owing to comparing different cross-section transect estimated observations. This discrepancy can be attributed to the fact that survey data is collected along the research pier, while the data used for the mTWM is extracted 49 m far from the research pier. The local scour is another possible reason for this discrepancy. Due to local scour, sand is eroded around the pier and accumulated to near side. Consequently, the cross-shore beach profile changes gradually along the pier, and beach slopes can be steeper than the surroundings.

To reduce the horizontal shift between the shoreline positions derived by mTWM and the survey data, the corrected wave set-up was applied to the tidal record to compensate for the horizontal shift in the estimated results. The MAB between the shoreline positions derived by mTWM with corrected wave set-up and the survey data is reduced to 10.5 m, while the intertidal foreshore slope remains almost same as previous. Due to wave set-up correction, the estimated shoreline position shifted landwards direction without changing the shape of intertidal beach profile. Furthermore, the correction of wave run-up was applied to the results obtained by the mTWM. This reduced the MAB to 5.9 m, which is smaller than the theoretical resolution of radar measurements; however, sometimes, the estimated bias was larger than spatial resolutions. These larger biases are the effect of milder intertidal foreshore slopes and the action of waves. The frequency distribution results indicate that 84 % estimated bias of shoreline positions are limited in the spatial resolution of the radar measurement. On the other hand, numerous random gaps were still existing in the dataset. These random gaps are due to lacking strong waterline signals that caused by over flooding, the existence of strong radar reflectors, etc.

To fill the random gaps, Garcia's method was applied in the mTWM derived shoreline positions with the corrected wave run-up. The MAB between these estimated shoreline positions and the survey data was 5.9 m, which is almost equivalent to that obtained before applying the gap filling method. This indicates the reliability of Garcia's method, and we can conclude that the mTWM integrated with this method is an efficient and robust approach to automatically detect shoreline positions from time-averaged X-band radar images with the consideration of wave run-up correction at sandy beaches during various periods, and to demonstrate the practicability of the utilized method. Therefore, the temporal and spatial variations of a shoreline can be automatically and continuously monitored over the long term to help authorities understand coastal changes, facilitating coastal protection and sustainable development in coastal zones.

5.1.2 Data fusion for X-band radars and SAR observations

Since the mTWM can estimates the shoreline positions from radar images with the aid of wave-run correction and Garcia's gap-filling method, then the mTWM was applied with a necessary correction to the remains other radars images between the period 2009 and 2012. As a result, the shoreline positions are obtained successfully. As we know, the mTWM obtained shoreline positions from radars data do not cover the whole spatial domain of the coast, then six available SAR observation shoreline positions were introduced within the mentioned period. Hereafter, a data fusion method was applied to combines the X-band radars and SAR satellite observation shoreline data with the help of DINEOF method. The method was successfully executed and verified the result with aerial laser survey data in May 2011. The MAB between these estimated shoreline positions and the aerial laser survey data was 11.7 m, which is almost close to the theoretical spatial resolution of Radar-3 and SAR satellite introduced data; however, sometimes, the estimated bias was larger than spatial resolutions. These larger biases are the effect of unavailability of radar images, tide and wave run-up corrections, seawards movement of aerial laser survey compared to SAR introduced data, and extrapolation outcomes. The frequency distribution results indicate that

74 % of the bias of the estimated shoreline positions were bounded in ±16 m, which is 1.5 times of the spatial resolution of Radar-3 and SAR satellite measurements. Therefore, the obtained outcome of the executed data fusion method that establishes a comprehensive strategy to fill the gap values in spatiotemporal shoreline dataset.

In brief, the modification of mTWM, the correction of wave set-up, the correction wave run-up, and data fusion are the new contribution of this study.

5.2 Limitation of the present study and recommendation for future study

This study can be used as a reference for future research works, although there are few limitations. The limitations of the study with some recommendation to mitigate the following issues are describing below:

- Already, it has been proved that X-band marine radar is a powerful tool to monitor the morphology at coastal zone; however, it has some shortcomings with respect to weather condition. In high precipitation time, radar provides unclear images. In such a circumstance, it is challenging to detect shoreline positions and intertidal foreshore slopes from radar images using any digitization method. In this study, some unclear time-averaged images were used to detect shoreline positions and foreshore slopes, which breaks the efficiency of the mTWM method. In order to improve the efficiency of automated mTWM, we will try to enhance the quality of image using advanced image processing and filtering techniques at high precipitation time in future study.
- Radar also provides unclear images in front and surrounding the radar location due to stronger backscatter signals. Consequently, it is tough to detect the

instantaneous waterline positions at these locations. On the contrary, the survey beach profile is collected along to pier, which is almost close to the surroundings of Radar-1 position. So, for data validation, it is essential to remove the noise from radar images near the center of Radar locations. It is confident that mTWM obtained results will be better if we improve the image quality at near the radar location.

- In the present study, the temporal update was set to two-weeks intervals corresponding to half of spring and half of neap tide and chosen to maximize the tidal range during each temporal window. From this observation, it is obvious that the mTWM is database method which cannot work correctly for less than two-weeks data. Further study may investigate reducing this interval to approximately a week or even less for intertidal shore profile estimation. However, it should be synchronized to span neaps to springs or springs to neaps to ensure the maximum tidal ranges are covered during each analysis period.
- For the data fusion, only six SAR satellite observation shoreline data were introduced between the time history 2009 and 2012. Due to unavailability of frequently observed SAR data, the outcomes of data fusion were not so precise and accurate. In the future study, we will try to introduce frequently observed data in between these periods from alternative sources like as Landsat, Sentinel. We hope that the data fusion results will be improved after introducing frequently observed data within mTWM processed radars shoreline data.

REFERENCES

Aarninkhof, S. G. J., Ruessink, B. G., & Roelvink, J. A. (2005). Nearshore subtidal bathymetry from time-exposure video images. *Journal of Geophysical Research: Oceans,* 110(C6).

Aarninkhof, S. G., Turner, I. L., Dronkers, T. D., Caljouw, M., & Nipius, L. (2003). A video-based technique for mapping intertidal beach bathymetry. *Coastal Engineering, 49*(4), 275 – 289.

Alvera-Azcárate, A., Barth, A., Parard, G., & Beckers, J. M. (2016). Analysis of SMOS sea surface salinity data using DINEOF. *Remote Sensing of Environment*, 180, 137-145.

Alvera-Azcárate, A., Barth, A., Rixen, M., & Beckers, J. M. (2005). Reconstruction of incomplete oceanographic data sets using empirical orthogonal functions: application to the Adriatic Sea surface temperature. *Ocean Modelling,* 9(4), 325-346.

Alvera-Azcárate, Aida, Quinten Vanhellemont, Kevin Ruddick, Alexander Barth, and Jean-Marie Beckers. "Analysis of high frequency geostationary ocean colour data using DINEOF." *Estuarine, Coastal and Shelf Science* 159 (2015): 28-36.

An, S., & Takewaka, S. (2016). A Study on the Morphological Characteristics around Artificial Headlands in Kashima Coast, Japan. *Journal of Coastal Research*, *32*(3), 508 – 518.

Austin, M. J., & Masselink, G. (2006). Observations of morphological change and sediment transport on a steep gravel beach. *Marine Geology, 229*(1-2), 59 – 77.

Beckers, J. M., & Rixen, M. (2003). EOF calculations and data filling from incomplete oceanographic datasets. *Journal of Atmospheric and Oceanic Technology*, 20(12), 1839-1856.

Bell, P. S. (1999). Shallow water bathymetry derived from an analysis of X-band marine radar images of waves. *Coastal Engineering*, *37*(3-4), 513–527.

Bell, P. S., Bird, C. O., & Plater, A. J. (2016). A temporal waterline approach to mapping intertidal areas using X-band marine radar. *Coastal Engineering, 107,* 84 – 101.

Bird, C. O., Bell, P. S., & Plater, A. J. (2017). Application of marine radar to monitoring seasonal and event-based changes in intertidal morphology. *Geomorphology*, *285*, 1 – 15.

Boak, E. H., & Turner, I. L. (2005). Shoreline definition and detection: a review. *Journal of Coastal Research*, 688 – 703.

Camfield, F. E., & Morang, A. (1996). Defining and interpreting shoreline change. *Ocean & Coastal Management*, *32*(3), 129 – 151.

Chang, H. K., Chen, W. W., & Liou, J. C. (2015). Shifting the waterlines of satellite images to the mean water shorelines considering wave runup, setup, and tidal variation. *Journal of Applied Remote Sensing*, *9*(1), 096004.

Chen, W. W., & Chang, H. K. (2009). Estimation of shoreline position and change from satellite images considering tidal variation. *Estuarine, Coastal and Shelf Science*, *84*(1), 54 – 60.

Crowell, M., Leatherman, S. P., & Buckley, M. K. (1991). Historical shoreline change: bias analysis and mapping accuracy. *Journal of Coastal Research*, 839 – 852.

Dankert, H., & Horstmann, J. (2007). A marine radar wind sensor. *Journal of Atmospheric and Oceanic Technology*, *24*(9), 1629 – 1642.

De Santiago, I., Morichon, D., Abadie, S., Castelle, B., Liria, P., & Epelde, I. (2013). Video monitoring nearshore sandbar morphodynamics on a partially engineered embayed beach. *Journal of Coastal Research*, *65*(sp1), 458 – 463.

Dellepiane, S., De Laurentiis, R., & Giordano, F. (2004). Coastline extraction from SAR images and a method for the evaluation of the coastline precision. *Pattern Recognition Letters*, 25(13), 1461-1470.

Deronde, B., Houthuys, R., Debruyn, W., Fransaer, D., Lancker, V. V., & Henriet, J. P. (2006). Use of airborne hyperspectral data and laserscan data to study beach morphodynamics along the Belgian coast. *Journal of Coastal Research*, 1108-1117.

Dolan, R. O. B. E. R. T., Hayden, B. P., May, P., & May, S. (1980). The reliability of shoreline changes measurements from aerial photographs. *Shore and Beach*, *48*(4), 22 – 29.

Fuse, T., & Ohkura, T. (2018). Development of Shoreline Extraction Method Based on Spatial Pattern Analysis of Satellite SAR Images. *Remote Sensing*, 10(9), 1361.

Galal, E. M., & Takewaka, S. (2008). Longshore migration of shoreline mega-cusps observed with X-band radar. *Coastal Engineering Journal*, *50*(03), 247 – 276.

Galal, E. M., & Takewaka, S. (2015). Temporal and spatial shoreline variability observed with a X-band radar at Hasaki coast, Japan. *Proceedings Coastal Sediments*, 1 – 9.

Garcia, D. (2010). Robust smoothing of gridded data in one and higher dimensions with missing values. Computational Statistics & Data Analysis, 54(4), 1167 –1178.

García-Rubio, G., Huntley, D., & Russell, P. (2015). Evaluating shoreline identification using optical satellite images. *Marine Geology*, *359*, 96 –105.

Gaudin, D., Delacourt, C., Allemand, P., Jaud, M., Ammann, J., Tisseau, C., & Véronique, C. U. Q. (2009, July). High resolution DEM derived from thermal infrared images: Example of Aber Benoit (France). In *Geoscience and Remote Sensing Symposium, 2009 IEEE International, IGARSS 2009*(Vol. 4, pp. IV-705). IEEE.

Goda, Y. (2010). Random seas and design of maritime structures (Vol. 33). *World Scientific Publishing Company*.

Hanslow D.J. (2007). Beach erosion trend measurement: a comparison of trend indicators, *Journal of Coastal Research*, Special Issue 50, 588 – 593

Hasan, G. J., & Takewaka, S. (2007). Observation of a stormy wave field with X-band radar and its linear aspects. *Coastal Engineering Journal*, *49*(02), 149 – 171.

Hasan, G. J., & Takewaka, S. (2009). Wave run-up analyses under dissipative condition using X-band radar. *Coastal Engineering Journal*, 51(02), 177 – 204.

Heygster, G., Dannenberg, J., & Notholt, J. (2010). Topographic mapping of the German tidal flats analyzing SAR images with the waterline method. *IEEE Transactions on Geoscience and Remote Sensing*, *48*(3), 1019 – 1030.

Hilborn, A., & Costa, M. (2018). Applications of DINEOF to satellite-derived chlorophyll-a from a productive coastal region. *Remote Sensing*, 10(9), 1449.

Holland, K. T., & Holman, R. A. (1997). Video estimation of foreshore topography using trinocular stereo. *Journal of Coastal Research*, 81 – 87.

Holman, R. A., & Bowen, A. J. (1984). Longshore structure of infragravity wave motions. *Journal of Geophysical Research: Oceans, 89*(C4), 6446 – 6452.

Holman, R. A., Sallenger, A. H., Lippmann, T. C., & Haines, J. W. (1993). The application of video image processing to the study of nearshore processes. *Oceanography*, *6*(3), 78 – 85.

Holman, R., & Haller, M. C. (2013). Remote sensing of the nearshore. *Annual Review of Marine Science*, *5,* 95 – 113. https://doi.org/10.1142/9789814689977_0212.

Hunt, I. A. (1959). Design of sea-walls and breakwaters. *Transactions of the American Society of Civil Engineers*, *126*(4), 542 – 570.

Iribarren Cavanilles, R. and Casto Nogales. M. (1949). Protection des ports. In *PIANC Congress 1949 SII-C4*. PIANC.

Katoh, K. &Yanagishima, S. (1995). Changes of sand grain distribution in the surf zone. *Proc. Coastal Dynamics' 99, Am. Soc. of Eng., New York*, 335 – 364.

Koopmans. B.N., Wang. Y. (1994). Satellite radar data for topographic mapping of the tidal flats in the Wadden Sea, The Netherlands. *Proceedings of the Second Thematic Conference on Remote Sensing for Marine and Coastal Environments, New Orleans*. Vol 31.

Kraus, N. C., & Rosati, J. D. (1997). Interpretation of shoreline-position data for coastal engineering analysis (No. CERC-CETN-II-39). *Coastal Engineering Research Center Vicksburg Ms.*

Kumar, D., & Takawaka, S. (2018). Estimation of Shoreline Positions by Combining X-band Radar and SAR Observations. *Journal of Japan Society of Civil Engineers, Ser. B2 (Coastal Engineering)*, 74(2), 979-984.

Kuriyama, Y. (2002). Medium-term bar behavior and associated sediment transport at Hasaki, Japan. *Journal of Geophysical Research: Oceans*, *107*(C9), 15 – 19.

Kuriyama, Y., & Lee, J. H. (2001). Medium-term beach profile change on a bar-trough region at Hasaki, Japan, investigated with complex principal component analysis. *Proceedings Coastal Dynamics*' 01, ASCE Press, 959 – 968.

Kuriyama, Y., Ito, Y., & Yanagishima, S. (2008). Medium-term variations of bar properties and their linkages with environmental factors at Hasaki, Japan. *Marine Geology*, *248*(1-2), 1 – 10.

Lakshminarayan, K., Harp, S. A., & Samad, T. (1999). Imputation of missing data in industrial databases. *Applied Intelligence*, 11(3), 259-275.

Lentz, S., & Raubenheimer, B. (1999). Field observations of wave setup. *Journal of Geophysical Research: Oceans*, *104*(C11), 25867 – 25875.

Liu, H., & Jezek, K. C. (2004). Automated extraction of coastline from satellite imagery by integrating Canny edge detection and locally adaptive thresholding methods. *International Journal of Remote Sensing*, 25(5), 937-958.

Liu, X., & Wang, M. (2018). Gap Filling of Missing Data for VIIRS Global Ocean Color Products Using the DINEOF Method. *IEEE Transactions on Geoscience and Remote Sensing*.

Mase, H. (1989). Random wave runup height on gentle slope. *Journal of Waterway, Port, Coastal, and Ocean Engineering*, *115*(5), 649–661.

Mason, D. C., Davenport, I. J., Robinson, G. J., Flather, R. A., & McCartney, B. S. (1995). Construction of an inter-tidal digital elevation model by the “Water-Line” Method. *Geophysical Research Letters*, *22*(23), 3187 – 3190.

Melby, J. A. (2012). Wave Runup Prediction for Flood Hazard Assessment. ERDC/CHL TR-12-24 *Technical Report. Vicksburg MS: Coastal and Hydraulics Laboratory, U.S. Army Engineer Research and Development Center*. 126 pp.

Nechad, B., Alvera-Azcaràte, A., Ruddick, K., & Greenwood, N. (2011). Reconstruction of MODIS total suspended matter time series maps by DINEOF and validation with autonomous platform data. *Ocean Dynamics*, 61(8), 1205-1214.

Nikolaidis, A., Georgiou, G. C., Hadjimitsis, D., & Akylas, E. (2014). Filling in missing sea-surface temperature satellite data over the Eastern Mediterranean Sea using the DINEOF algorithm. *Central European Journal of Geosciences*, 6(1), 27-41.

Pajak, M. J., & Leatherman, S. (2002). The high-water line as shoreline indicator. *Journal of Coastal Research*, 329-337.

Paravolidakis, V., Ragia, L., Moirogiorgou, K., & Zervakis, M. (2018). Automatic Coastline Extraction Using Edge Detection and Optimization Procedures. *Geosciences*, 8(11), 407.

Pardo-Pascual, J. E., Almonacid-Caballer, J., Ruiz, L. A., & Palomar-Vázquez, J. (2012). Automatic extraction of shorelines from Landsat TM and ETM+ multi-temporal images with subpixel precision. *Remote Sensing of Environment*, 123, 1-11.

Plant, N. G., & Holman, R. A. (1997). Intertidal beach profile estimation using video images. *Marine Geology*, *140*(1-2), 1 – 24.

R. W. Ives, On the Compression of Synthetic Aperture Radar Imagery. PhD thesis, Dept. of Electrical and Computer Engineering, The University of New Mexico, Albuquerque, New Mexico, May 1998.

Ruessink, B. G., Kleinhans, M. G., & Van den Beukel, P. G. L. (1998). Observations of swash under highly dissipative conditions. *Journal of Geophysical Research: Oceans*, *103*(C2), 3111 – 3118.

Ruggiero, P., Holman, R. A., & Beach, R. A. (2004). Wave run-up on a high-energy dissipative beach. *Journal of Geophysical Research: Oceans*, *109*(C6).

Ryu, J. H., Kim, C. H., Lee, Y. K., Won, J. S., Chun, S. S., & Lee, S. (2008). Detecting the intertidal morphologic change using satellite data. *Estuarine, Coastal and Shelf Science*, *78*(4), 623 – 632.

Ryu, J. H., Won, J. S., & Min, K. D. (2002). Waterline extraction from Landsat TM data in a tidal flat: a case study in Gomso Bay, Korea. *Remote Sensing of Environment*, *83*(3), 442 – 456.

Sirjacobs, D., Alvera-Azcárate, A., Barth, A., Lacroix, G., Park, Y., Nechad, B., & Beckers, J. M. (2011). Cloud filling of ocean colour and sea surface temperature remote sensing products over the Southern North Sea by the Data Interpolating Empirical Orthogonal Functions methodology. *Journal of Sea Research*, 65(1), 114-130.

Sobral, F., Pereira, P., Cavalcanti, P., Guedes, R., & Calliari, L. (2013). Intertidal bathymetry estimation using video images on a dissipative beach. *Journal of Coastal Research*, *65*(sp2), 1439 – 1444.

Stockdon, H. F., Holman, R. A., Howd, P. A., & Sallenger Jr, A. H. (2006). Empirical parameterization of setup, swash, and runup. *Coastal Engineering*, *53*(7), 573 – 588.

Takewaka, S. (2005). Measurements of shoreline positions and intertidal foreshore slopes with X-band marine radar system. *Coastal Engineering Journal*, *47*(2-3), 91 – 107.

Taylor, M. H., Losch, M., Wenzel, M., & Schröter, J. (2013). On the sensitivity of field reconstruction and prediction using empirical orthogonal functions derived from gappy data. *Journal of Climate*, 26(22), 9194-9205.

Uunk, L., Wijnberg, K. M., & Morelissen, R. (2010). Automated mapping of the intertidal beach bathymetry from video images. *Coastal Engineering*, *57*(4), 461 – 469.

Valentini, N., Saponieri, A., Molfetta, M. G., & Damiani, L. (2017). New algorithms for shoreline monitoring from coastal video systems. *Earth Science Informatics*, *10*(4), 495 – 506.

Vandebroek, E., Lindenbergh, R., van Leijen, F., de Schipper, M., de Vries, S., & Hanssen, R. (2017). Semi-automated monitoring of a mega-scale beach nourishment using high-resolution terrasar-x satellite data. *Remote Sensing*, 9(7), 653.

Vitousek, P. M., Mooney, H. A., Lubchenco, J., & Melillo, J. M. (1997). Human domination of Earth's ecosystems. *Science,* 277(5325), 494-499.

Wang, G., Garcia, D., Liu, Y., De Jeu, R., & Dolman, A. J. (2012). A three-dimensional gap filling method for large geophysical datasets: Application to global satellite soil moisture observations. *Environmental Modelling & Software*, 30, 139 – 142.

Wang, J., Leach, R. K., & Jiang, X. (2015). Review of the mathematical foundations of data fusion techniques in surface metrology. *Surface Topography: Metrology and Properties*, 3(2), 023001.

Xu, Z., Kim, D. J., Kim, S. H., Cho, Y. K., & Lee, S. G. (2016). Estimation of seasonal topographic variation in tidal flats using waterline method: A case study in Gomso and Hampyeong Bay, South Korea. *Estuarine, Coastal and Shelf Science*, *183*, 213 – 220.

Yousef, A. H., Iftekharuddin, K. M., & Karim, M. A. (2013). Shoreline extraction from light detection and ranging digital elevation model data and aerial images. *Optical Engineering*, 53(1), 011006.

Zhai, Y., (2010). Time-dependent Scour Depth under Bridge-submerged Flow. M. E. Dissertation. University of Nebraska-Lincoln, Lincoln.

Zhao, B., Guo, H., Yan, Y., Wag, Q., & Li, B. (2008). A simple waterline approach for tidelands using multi-temporal satellite images: a case study in the Yangtze Delta. *Estuarine, Coastal and Shelf Science*, *77*(1), 134 – 142.

Zhou, W., Peng, B., & Shi, J. (2017). Reconstructing spatial-temporal continuous MODIS land surface temperature using the DINEOF method. *Journal of Applied Remote Sensing*, 11(4), 046016.

BIBLIOGRAPHY

Kumar, D., and Takewaka, S. (2018). Estimation of Shoreline Positions by Combining X-band Radar and SAR Observations. *Journal of Japan Society of Civil Engineers, Ser. B2 (Coastal Engineering)*, 74(2), 779 – 784.

Kumar, D., and Takewaka, S. (2019). Automatic Shoreline Position and Intertidal Foreshore Slope Detection from X-band Radar Images using modified Temporal Waterline Method with Corrected Wave Run-up. *Journal of Marine Science and Engineering*, 7(2), 45.

Kumar, D., and Takewaka, S. (2019). Execution of Missing Value Imputation Techniques for X-band Radar and SAR Satellite Observations of Shoreline Data Gaps. (Under submission).